TECHNISCHE UNIVERSITÄT WIEN
Vienna | Austria

TOKYO AOYAMA GAKUIN

DIPLOMARBEIT

Synthesis of Compounds using Hard/Hard and Soft/Soft Lewis Acid - Base interactions and Investigation of their Properties for Possible Industrial Applications

Ausgeführt am Institut für

Angewandte Synthesechemie

in Kooperation mit dem

Institut für Festkörperphysik

der Technischen Universität Wien

und dem

Department of Chemistry and Biological Science

der Aoyama Gakuin Universität

unter der Anleitung von

Univ. Prof. Dr. Wolfgang **Linert**

Univ. Prof. Dr. Ernst **Bauer**

Univ. Prof. Miki **Hasegawa**, Ph.D.

durch

Marlene **Mathuber**, B.Sc.

(1025175)

Hauptplatz 2/32, A-2601 Sollenau,

AUSTRIA

Wien, Dezember 2016

In dieselben Flüsse steigen wir hinab und steigen wir nicht hinab,

wir sind und wir sind nicht.

Heraklit

Danksagung

Zu Beginn möchte ich mich vor allem bei **Univ. Prof. Dr. Wolfgang Linert** bedanken, der mir diese Arbeit ermöglicht hat und mich dabei immer mit Rat und Tat unterstützt hat.

Durch seine weitreichenden internationalen Vernetzungen war es mir möglich einen Teil dieser Arbeit in Japan (Sagamihara, Kanagawa) an der Aoyama Gakuin Universität in der Arbeitsgruppe von **Univ. Prof. Miki Hasegawa, Ph.D.** abzulegen. Ich möchte mich auch bei ihr, ihrer Assistentin **Ayumi Ishii, Ph.D.** und der gesamten Arbeitsgruppe für die herzliche Aufnahme und Begleitung während meines Auslandsaufenthaltes bedanken. In diesem Sinne: ありがとうございました**!**

*I would also like to thank **Univ. Prof. Miki Hasegawa, Ph.D.**, her assistant **Ayumi Ishii, Ph.D.** and the entire workgroup for their warm welcome and help during my stay abroad. In this sense:* ありがとうございました**!**

Weiters möchte ich **Univ. Prof. Dr. Ernst Bauer** danken, der mich bei dem zweiten Teil dieser Arbeit beraten und unterstützt hat. Auch bei seinem Dissertanten **Dipl.-Ing. Igor Knapp** und Post-Doc **Dr. Patrick Heinrich** möchte ich mich für ihre Hilfe bei den Messungen und Auswertungen bedanken.

Großer Dank gebührt auch **Dipl.-Ing. Esther Knittl**, die mir bei meiner Arbeit im Labor zur Seite stand und immer ein offenes Ohr für mich hatte, und **Dr. Matthias Mastalir** sowie **Alexander Müller** für die Beratung bzw. Unterstützung der Versuche.

Ich möchte mich vor allem auch bei meinen Freunden und Laborkollegen für die außergewöhnlich gute Arbeitsatmosphäre während meines gesamten Studiums und die vielen vergnüglichen Stunden abseits der Universität bedanken.

Besonderer Dank gebührt auch **Birgit Ringhofer**, die mich während dieser Arbeit motiviert hat und mir immer eine große Stütze war.

Der größte Dank gebührt meiner Familie für die Ermöglichung meines Studiums. Vor allem meiner Mutter **Claudia** und meinem Vater **Johann Mathube**r danke ich dafür, dass sie immer an mich glauben und mich bei allen Plänen unterstützen. Ihnen möchte ich auch diese Arbeit widmen.

Abstract

Goal of this diploma thesis was the synthesis of various compounds for potential, industrial applications. In general these compounds can be classified into two groups by the HSAB-concept and Lewis Acid-Base interactions, namely Hard/Hard and Soft/soft chemical relations:

The first part deals with the synthesis of helical, polymeric lanthanoide complexes, which are typical representatives of Hard/Hard interactions (small atom radii, strongly polarizing). These kinds of complexes show characteristic luminescence spectra. Therefore they can be, amongst other things, applied for the production of screens. This part of was carried out at the Department of Chemistry and Biological Science, Aoyama Gakuin University in Japan in the course of staying abroad. In addition a new ligand was successfully synthesized at the Institute of Applied Synthetic Chemistry at the Vienna TU:

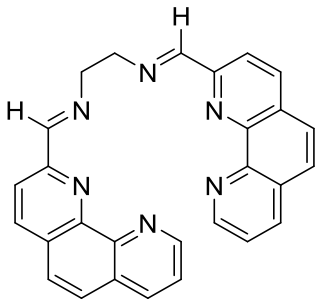

This ligand is ideal for coordination reactions with lanthanides. In this manner the significant emission spectra of these elements can be drastically enhanced.

The second part of this master thesis deals with the synthesis of copper(I)sulfide from elemental Copper and Sulfur. Copper(I)sulfide is a typical representative of Soft/Soft interactions. Both starting materials for this reaction are comparatively big and easy to polarize elements.

The aim was to synthesize this chemical compound under diverse reaction conditions and in various stoichiometric ratios, then to analyze the fabricated samples in regard to their suitability as thermoelectric material. Therefore the dimensionless figure of merit ZT is used, which is calculated by the following formula:

$$ZT = \frac{S^2 \sigma T}{\lambda},$$

whereby S is the Seebeck coefficient, σ the electric conductivity , λ the thermal conductivity and T the temperature.

In the course of this diploma thesis several samples were synthesized, compared to each other and analyzed in regard to the Seebeck coefficient and the electric resistivity ρ ($\sigma = \frac{1}{\rho}$).

The thermal conductivity will be measured prospectively. However by using a value for it, which is well known in appropriate literature, a potential ZT-value could be calculated. In doing so values up to 2.592 could be obtained, which are very promising results.

These experiments were carried out at the Institute of Solid State Physics at the Vienna TU.

Kurzfassung

Das Ziel dieser Diplomarbeit war die Synthese von diversen Verbindungen für potentielle, industrielle Anwendungen, welche generell mit Hilfe des HSAB-Konzepts und der Lewis Säure-Basen Wechselwirkungen in die Gruppen der Hart/Hart oder Weich/Weich Verbindungen eingeteilt wurden:

Der erste Teil beschäftigt sich mit der Synthese von helikalen, Polymer-Lanthanoid-Komplexen, welche den Hart/Hart Verbindungen entsprechen (kleine Atomradien, stark polarisierend). Solche Komplexe zeigen charakteristische Lumineszenz-Spektren und finden daher unter anderem Anwendung in Bildschirmen. Dieser Teil der Arbeit wurde am Department of Chemistry and Biological Science an der Aoyama Gakuin Universität in Japan im Zuge eines Auslandaufenthaltes durchgeführt.

In weiterer Folge wurden am Institut für Synthesechemie der TU Wien folgender, neuer Ligand erfolgreich synthetisiert:

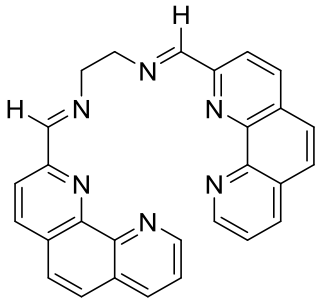

Dieser Ligand eignet sich ausgezeichnet für die Koordination mit Lanthanoiden und verstärkt dadurch die signifikanten Emissionsspektren dieser Verbindungen.

Der zweite Teil dieser Arbeit strebte die Herstellung von Kupfer(I)sulfid aus elementarem Kupfer und Schwefel an. Kupfer(I)sulfid ist ein typischer Vertreter der Weich/Weich Verbindungen, da die beiden verwendeten Ausgangsstoffe vergleichsweise große, polarisierbare Elemente darstellen.

Ziel war es, diese chemische Verbindung unter verschiedenen Bedingungen und in diversen stöchiometrischen Verhältnissen zu synthetisieren und auf ihre Qualitäten als thermoelektrisches Material zu untersuchen. Dafür wird die dimensionslose Gütezahl ZT verwendet, welche sich wie folgt zusammensetzt:

$$ZT = \frac{S^2 \sigma T}{\lambda},$$

wobei S den Seebeck Koeffizienten, σ die elektrische Leitfähigkeit, λ die thermische Leitfähigkeit und T die Temperatur bezeichnet.

Im Zuge dieser Diplomarbeit wurden entsprechende Proben hergestellt, verglichen und bezüglich des Seebeck Koeffizienten und des elektrischen Widerstandes ρ ($\sigma = \frac{1}{\rho}$) untersucht. Die thermische Leitfähigkeit wird in weiterer Folge zukünftig gemessen. Es konnte jedoch durch die Verwendung eines literaturbekannten Wertes ein potentieller Wert für die Gütezahl ZT berechnet werden. Dabei wurden Werte bis 2.592 erreicht, was ein sehr zufriedenstellendes Ergebnis darstellt.

Diese Versuche wurden in Kooperation mit dem Institut für Festkörperphysikwurde der TU Wien durchgeführt.

Abbreviations

Besides common abbreviations of the English language and chemical symbols the short forms below are used:

ACN	acetonitrile
adc	9,10-anthracenedicarboxylic acid
Abs.	absolute
bdc	terephthalic acid
DMF	dimethylformamide
EE	ethyl acetate
Et_2O	diethylether
EtOH	ethanol
iPrOH	isopropyl alcohol
HCl	hydrochloric acid
FT-IR	Fourier Transform Infrared Spectroscopy
M	molar
MeOH	methanol
MeLi	methyllithium
Mp	melting point
ndc	1,4-naphthalenedicarboxylic acid
NH_3	ammonia
NMR	Nuclear Magnetic Resonance
Phen	1,10-phenathroline
RT	room temperature
T	Temperature
TLC	thin layer chromatography
THF	tetrahydrofuran
XRD	X-ray diffraction

General Remarks

References to the Literature

Within the text, references are marked with Arabic numbers in angular brackets. Figures marked with no reference are from private use.

Nomenclature

The nomenclature of compounds, which were not mentioned yet in the chemical literature, is done by using the IUPAC based rules of Chemical Abstracts.

Well known chemicals and reagents are partly designated by their trivial names.

In the experimental part the empirical formula and molar mass in [g/mol] are written down below the structures. An exemplary depiction is shown below:

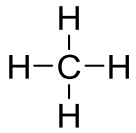

Chemical structure

CH_4 Sum formula

16.04 Molar mass [g/mol]

Table of Content

Introduction

As mentioned above in the title, this thesis comprises two parts. In a first part, attention is given to the Hard/Hard Lewis Acid-Base interactions of lanthanide complexes and their properties for possible industrial applications (*Part I*). The other aspect, Soft/Soft interactions, refer to the synthesis of copper(I)sulfide and its potential application as thermoelectric materials. The results of these experiments can be found in *Part II*.

Within this thesis both parts will be discussed in detail in the following chapters.

HSAB-Concept

The HSAB (= **H**ard and **S**oft **A**cid and **B**ases) concept, which is also named Pearson concept after its founder, is a frequently used theory to describe acids and bases. With this concept, it is possible to estimate, if and how a compound is formed, if it is stable and how it will react under various conditions with different reaction partners. It is based on the well known Lewis Acid-Bases concept, which describes Lewis-Bases as electron pair donators and Lewis-Acids as electron pair acceptors. Within the HSAB concept further distinctions between hard and soft acids as well as bases are made. This means that unlike as with the Brønsted theory, the stability of adducts is reliant on the characteristics of both reaction partners. [1] [2]

In general this concept describes following assumptions:

A “hard” particle (atoms, ions or molecules) shows a very high density of charge as compared with a concurrent relatively small radius. There is a quite big ratio between both factors. This kind of particles are hardly polarizable, however, they have a strongly polarizing effect. In complete contrast to this, there exist “soft” particles. These show a very low density of charge with a simultaneous big radius. Here, a small charge to radii ratio can be found. Soft particles can easily be polarized, but they have only a weak polarizing effect. The development of a compound between a hard Lewis-Acid and –Base rather results in an ionic chemical species with electrostatic character. On the other hand covalent species are rather formed by the reaction of a soft Lewis-Acid and –Base. Generally hard acids rather react with hard bases and vice versa in regard to soft species. Then again this consideration must not be understood absolutely, but relatively and as a common guideline. There are different thermodynamic reasons for the formation and stability of such compounds, which cannot be summarized in simple uniform rules. [1] [2]

The HSAB concept is hardly used for quantitative explanations, although there were some quite successful attempts to describe the dissociation energy of Lewis-Acid-Base adducts, but rather for qualitative considerations, such as inorganic analyses in aqueous solutions. It is also useful for a better understanding of coordination reactions and structures of complexes. There are numerous examples that are based on this concept. For example in regard to the previously mentioned separation process the prediction of the reaction behavior of inorganic ions.

According to the HSBA-concept, a silver-ion is a soft acid; therefore, it should rather form a compound with soft bases. In the case of halides, the "hardness" of the rise from bottom to top, which means that fluoride is the hardest base. Therefore, the stability of silver halides should increase from fluorine to iodine. Verifying this consideration by practical experiments, it turns out that silver fluoride is easy soluble in aqueous solutions, in contrast to silver bromide or especially silver iodide. These compounds with a high proportion of covalent bonds are poorly or nearly insoluble in a comparable medium. [1] [2]

A classic example for a hard acid is the proton, a hard corresponding base the fluoride ion. The result of a reaction between these two species is hydrogen fluoride. This compound shows the lowest dissociation tendency in aqueous solutions compared to other hydrogen halides. Although the HSAB-concept is very useful for qualitative statements, it has its limits, especially, when other effects supervene. Therefore, it is very important to see the chemical system as a whole, with all competing aspects. For instance, the salt formation of sodium ions with fluoride or hydroxide: Here, in accordance to the HSAB-concept, stable salts should be formed. In reality well known soluble salts are formed. The reason for this is the hydration of the compound caused by the used solvent. [1] [2]

Summarizing, following general classifications between hard and soft acids and bases can be set up:

Hard: small atomic/ionic radius, low polarizability, but strong polarizing effect, tends to ionic bonding, often in high oxidation stage, electronegativity for bases is quite high;

Soft: rather large atomic/ionic radius, easy to polarize, but weak polarizing effect, tends to covalent bonding, low or zero oxidation stages are often found, electronegativity for bases is rather low;

These classifications are reflected in the subsequent examples:

Hard Acids: H^+, Na^+, Cr^{3+}, Cr^{6+}, BF_3, Mn^{2+}, Co^{3+}, Fe^{3+}, Mg^{2+}, Ca^{2+}, etc.

Hard Bases: H_2O, OH^-, F^-, Cl^-, NH_3, R_3N, CO_3^{2-}, PO_4^{3-}, etc.

Soft Acids: Pt^{2+}, Pt^{4+}, Pd^{2+}, Au^+, Cu^{2+}, Hg^{2+}, Cd^{2+}, Cu^+, Pb^{2+}, Ag^+, etc.

Soft Bases: SCN^-, R_2S, R-SH, CN^-, R_3P, I^-, etc. [1] [2]

It can therefore be said that the synthesized Eu-complexes in this diploma thesis are typical representatives of Hard/Hard Lewis Acid-Base interactions, Soft/Soft interactions, however, can be found in the fabricated copper(I)sulfide bulks. In the following chapters the syntheses and properties regarding possible industrial applications of both parts will be discussed.

I. Part:

Synthesis of Eu-Complexes and an Associated Novel Ligand

I.A. Formula Scheme

I.A.1. Synthesis of Eu-Complexes

I.A.1.1. $Eu(phen)_2(NO_3)_3$

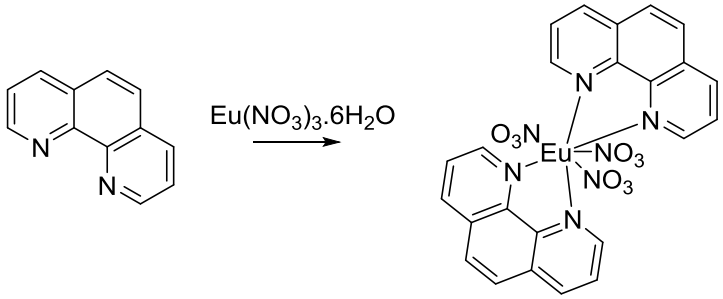

I.A.1.2. $Eu(bdc)(NO_3)_3$

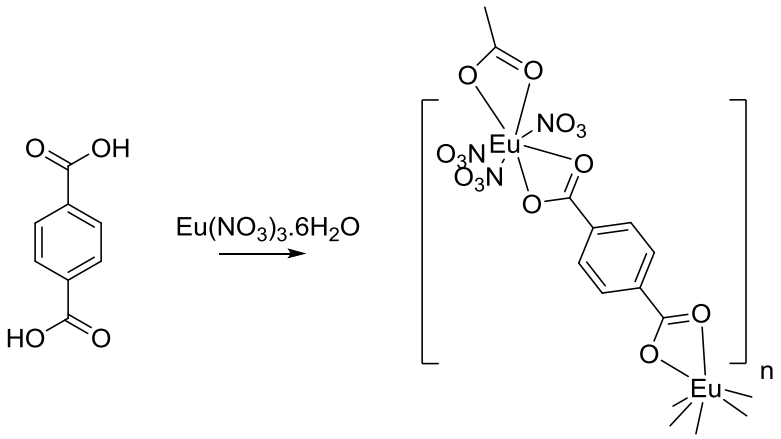

I.A.1.3. $Eu(ndc)(NO_3)_3$

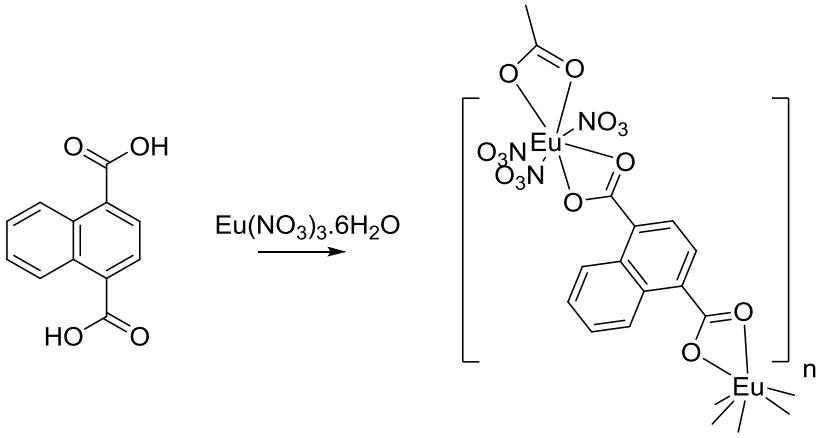

I.A.1.4. Eu(adc)$(NO_3)_3$

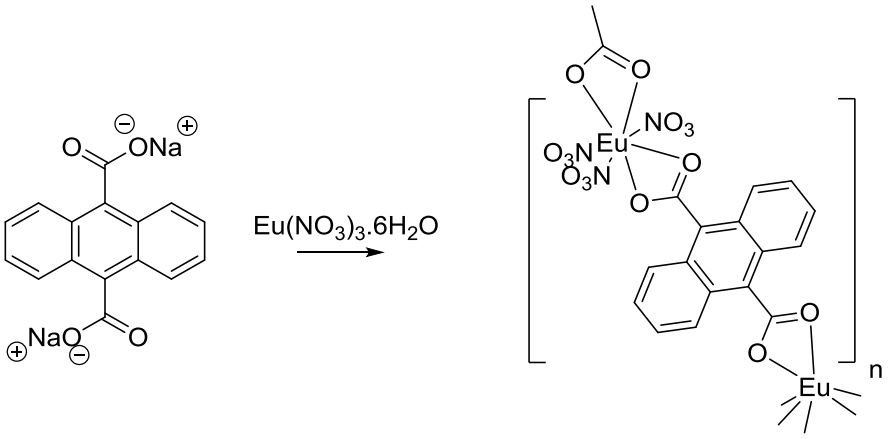

I.A.2. Synthesis of N,N^{I}-(Ethane-1,2-diyl)-bis(1,10-phenanthroline-2-yl)methanimin

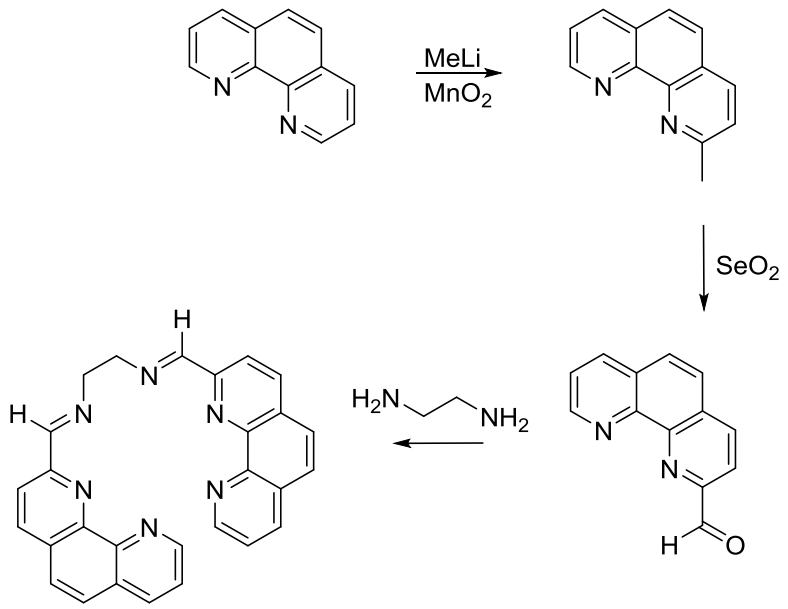

I.B. General Aspects

The following section provides an insight in the chemistry of lanthanides and their complexes. Also the motivation of this thesis will be more closely analyzed and discussed.

I.B.1. Lanthanides

I.B.1.1. Historical and Other Aspects

In presenting the group of lanthanides, it is definitely worth to take a look on the periodic table first (see figure I.B.1):

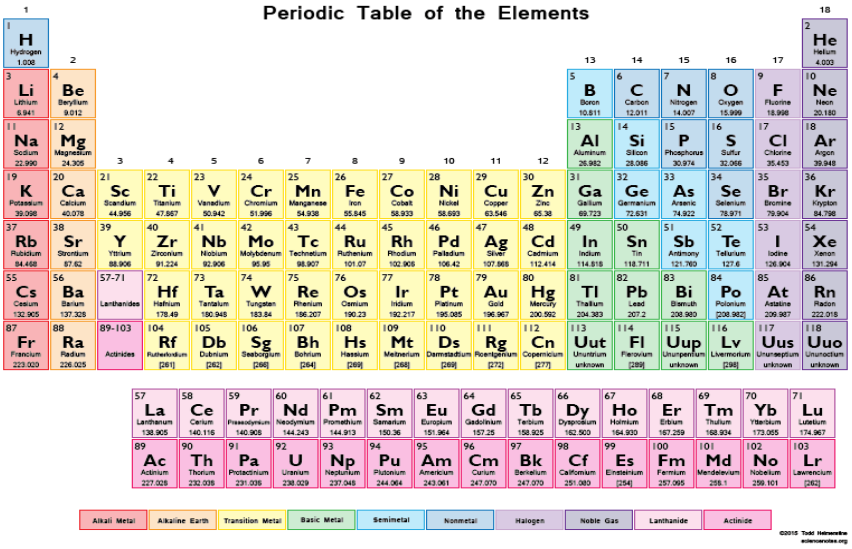

Figure I.B.1: The Periodic Table of Elements [3]

The lanthanides (Ln) can be found at the bottom of the periodic table of elements, right over the actinides (pale pink blocks in figure I.B.1). The elements of this group are the first ones, which start to fill the 4f electron shell. There is often a considerable confusion, which element starts the f-block elements. Although the name giver is obviously lanthanum (La), this element has not the appropriate electron configuration ([Xe] 6s2 5d1). Actually, the f-block elements start with Cerium (Ce) and end, after the filling of 14 f-electrons, with Lutetium (Lu). Overall there can be fifteen elements found, which belong to the lanthanides, namely La, Ce, Pr (Praseodymium), Nd (Neodymium), Pm (Promethium), Sm (Samarium), Eu (Europium), Gd (Gadolinium), Tb (Terbium) , Dy (Dysporsium), Ho (Holmium), Er (Erbium), Tn (Thulium), Yb (Ytterbium) and Lu). Their atomic numbers go from 57 to 71 and they all have a metallic character. The last element of this series is, as mentioned above, Lutetium with an electron configuration of [Xe] $4f^{14}5d^{1}6s^{2}$. [1]

Another term for lanthanides is rare earth metals (REM). This name comes from following reasons:

Firstly, large deposits of suitable raw materials are actually quite rare. The largest known deposits of rare earth metals can be found in china, more precisely in the Inner Mongolia (about 2.9 million of tons). Another deposit rich of raw materials is settled in West-Australia at Mount Weld (about 1.4 million of tons). Smaller reservoirs are distributed in the rest of the world. Secondly, the desired elements exist only in very small amounts or as a mixture in minerals. Therefore, the majority of industrial extractions of rare earth metals happen during the production process of other, more concentrated metals. [4] [5]

In figure I.B.2 an example for such a mineral (Lanthanite), containg various lanthanides, can be seen:

Figure I.B.2: Mineral Lanthanite, chemical formula $(La,Dy,Ce)_2(CO_3)_3*8H_2O$ [6]

Another fact is the constantly growing demand of rare earth metals each year. In 2010 the annual global production was approximately 133,000 tons. According to estimations, the yearly demand of REMs will increase up to 160,000 hundred of thousand tons. One of many reasons for this phenomenon is the increasing popularity of hybrid/electric cars. To produce the motor of a Toyota electric Prius, 1 kg of Nd is necessary, its battery needs up to 15 kg of La. Due to soaring sales, the demand will continue rapidly. [7] [8]

But it has not been like this ever since. Looking briefly back at the history of lanthanides, it appears that they were not of great interest in former times. In 1787, an unusual black mineral was found in a small city called Ytterby in Sweden. A few years later, the Finnish researcher J. Gadolin found out that this mineral contains a new element and named it Ytterbium. He first wrote about it in *Proceedings of the Swedish Academy of Sciences 1794*. Unfortunately, he could not separate and isolate this element, only its oxide. The isolation of this lanthanide was firstly accomplished by the Swiss Chemist J. G. Galissard de Marignac in 1878. In general, the separation and isolation of lanthanides from each other and chemical similar elements such as Scandium (Sc) or Yttrium (Y) was very difficult. It succeeded for the very first time in 1909 by very often repeated fractional crystallizations. The difficulties of the isolation process are due to their chemical resemblance. For example, they show a very similar behavior in regard to coordination reactions and solubility. [4] [5]

The reason for this is amongst other things the so called lanthanide contraction, which will be discussed later (see *I.B.1.2.Theoretical Background*, page 7). The distinguishability between the lanthanoide elements was finally realized in 1913 with methods like X-ray spectroscopy. In this manner, it was possible to present the existence of these 15 elements and to exclude other theories. The methods introduced at the time for winning lanthanides in larger scales, such as ionexchange chromatography or the liquid-liquid extraction methods are still used today. [4] [5]

The last discovered lanthanide was Promethium. This element has only radioactive isotopes and was discovered in 1945 by J. A. Marinsky, L. E. Glendenin and C. D. Coryell. Pr was synthetically created as a result of a controlled Uranium experiments. Therefore, only very small traces of this element can be found in nature. Its name comes from the Greek Titan Prometheus, who angered the Greek gods by stealing their fire to give it to the human people. A name chosen to be a warning for scientists, considering that the beginning of nuclear armaments race started at that time. [1] [9]

I.B.1.2. Theoretical Background

As mentioned above, the lanthanides are the first elements of the periodic table, which are starting to occupy the 4f-level. Thereby, the outer N-shell can be filled up with the maximum amount of 32 electrons. In table I.B.1 the associated electron configuration (EC) of these elements and their $^{3+}$-ions are illustrated, again with La und Lu (the first mentioned element has no electrons in the 4f-level, whereas the last one shows the maximum number) [1]

Table I.B.1: Electron Configuration of Lanthanoide [1]

Atomic Number	Element	Symbol	EC Atom	EC Ion Ln^{3+}
57	Lanthan	^{139}La	$5d^16s^2$	[Xe]
58	Cer	^{140}Ce	$4f^26s^22$	$4f^1$
59	Praseodym	^{141}Pr	$4f^36s^2$	$4f^2$
60	Neodym	^{142}Nd	$4f^46s^2$	$4f^3$
61	Promethium	^{147}Pm	$4f^56s^2$	$4f^4$
62	Samarium	^{152}Sm	$4f^66s^2$	$4f^5$
63	Europium	^{153}Eu	$4f^76s^2$	$4f^6$
64	Gadolinium	^{158}Gd	$4f^75d^16s^2$	$4f^7$
65	Terbium	^{159}Tb	$4f^96s^2$	$4f^8$
66	Dysprosium	^{162}Dy	$4f^{10}6s^2$	$4f^9$
67	Holmium	^{165}Ho	$4f^{11}6s^2$	$4f^{10}$
68	Erbium	^{166}Er	$4f^{12}6s^2$	$4f^{11}$
69	Thulium	^{169}Tm	$4f^{13}6s^2$	$4f^{12}$
70	Ytterbium	^{174}Yb	$4f^{14}6s^2$	$4f^{13}$
71	Lutetium	^{175}Lu	$4f^{14}5d^16s^2$	$4f^{14}$

Generally, the 6s, 5d and 4f-level show very similar energies, therefore, the filling of these levels follows no strict rule. Considering the chemical similarities of the lanthanides, this can also be lead back to their electron configurations. Each electron added to the chemical system will occupy the third outermost shell. Therefore, no spectacular changes can be observed within the chemistry of lanthanides. It turned out that each element of this series can be found in the oxidation state +3. In addition, the atom radii of the lanthanides are very similar to each other. The only exceptions are Eu and Yb due to their electron configuration ($4f^7$ and $4f^{14}$). In figure I.B.3 the atomic radii of all lanthanides are portrayed: [1] [4]

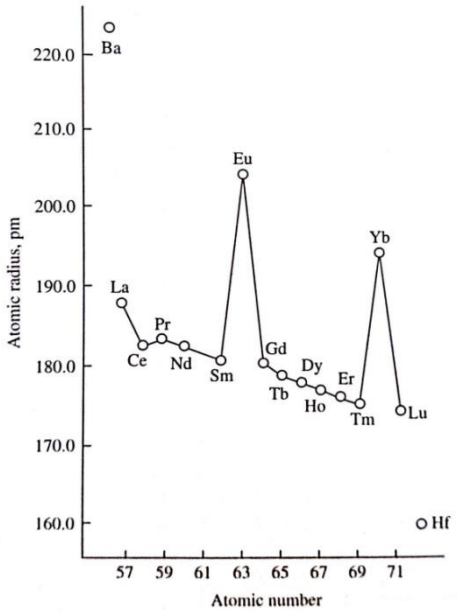

Figure I.B.3: Atomic Radius of the Lanthanoide Elements [4]

A reason for this unusual decrease of the atom radii is the so called lanthanide contraction. This phenomenon is caused by the newly introduced f-electrons. Generally, the f-atom orbitals are quite big, compared to the others. In this diffuse orbitals the electrons are “more agile” and they are not selectively localized as in the other orbitals. Therefore, 4f electrons are not very capable to shield the electrons in the outer shells from the effective nuclear charge. As a result, the 5s and 5p electrons are drawn to the centre and the atomic radius decreases with increasing atomic weight. In addition, the so called relativistic effects must be taken into consideration. These effects occur in heavy elements. Electrons close to the atomic nucleus happen to have a relativistic greater mass. Thereby, the inner atomic shells are contracted and the f-electrons are even more destabilized and delocalized. This phenomenon can also be observed with the Ln^{3+} -ion. The lanthanide contraction affects the ionic radius that strongly, so that at some point the radius of Ho^{3+} ([Xe] $6s^0$ $5d^0$ $4f^{10}$) becomes almost similar to the radius of Y^{3+} ([Kr] $5s^0$ $4d^0$). This explains the similarities of the lanthanides with the elements of group 3. [4] [5] [10]

Beyond all these remarkable features, one characteristic of the lanthanides especially points out, namely its spectroscopic properties. Solids containing appropriate Ln-compounds show a discrete energy spectrum, which means that single spectral lines can be observed. This is due to the special arrangement and structure of the atomic shells, which distinguish the spectroscopic behavior of d- and f- elements drastically from each other. The 4-f orbitals are shielded, as mentioned above, by the bigger 5s, 5p- and 6s orbitals, which are although lower in energy still a little higher situated. This behavior is shown in figure I.B.4 based on the example of Ce: [4] [5]

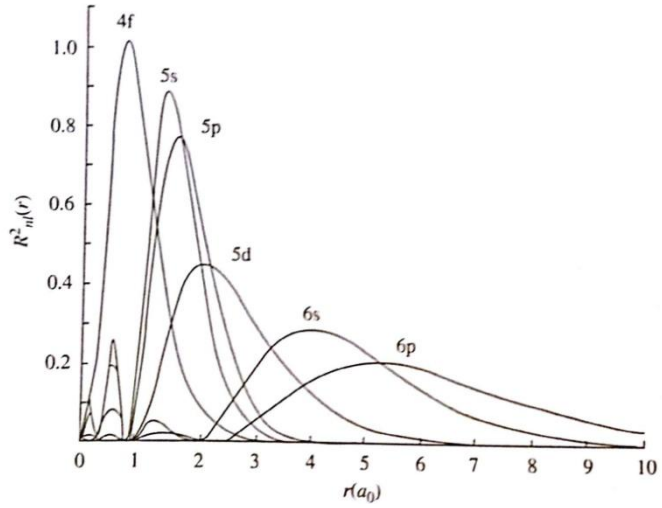

Figure I.B.4: Radial Distribution Functions for Ce [4]

In this manner, the optical transitions in the 4f-orbitals are protected from outer chemical influences. Due to this kind of isolation, electronic band structures cannot be formed. In total, there are up to 14 f-electrons, which can be distributed in several ways over the seven available 4f-orbitals. Therefore, lanthanide compounds have many various electron configurations, including partial filling of orbitals. This results in a higher amount of electric transitions in comparison to d-transition metals. As mentioned above, these transitions are hardly affected by external influences, such as solvents, etc.

The characteristic spectroscopic properties, namely, absorption and emission, are caused by the numerous possible transitions within the outer $5s^2$, $5p^6$ and $4f^n$ configuration (n = amount of electrons). This applies obviously not for La^{3+} and Lu^{3+}, since their 4f orbitals are either empty or completely filled. An example for the great quantities of lanthanide-ions in regard to their electron configurations, is elemental Pr. This element has summa summarum up to 3106 energy states, in its excited state even up to 36 000. Of course, not every transition is permitted by specific selection rules (namely Russel-Saunders and jj coupling rules). However, after applying these rules, there still can be about 30 000 visible spectral lines observed. This can generally be said for every element or its ion with partly filled f orbitals. [4] [5]

The impressive dimensions of these spectral properties become aware in comparison to other elements of the periodic table. Main group elements with partly filled p-orbitals can have up to 1000 spectral lines, transition metals with partly filled d-orbitals have a bit more, up to 7000 spectral lines. In addition, the absorption and emission of lanthanides occur in a broad spectral range (UV-VIS-NIR-MIR). As can be clearly seen, these elements show quite impressive characteristics, which make them very interesting for several industrial applications.

Some excited states are caused by 4f-4f transitions. But as mentioned above, these transitions should be forbidden due to the specific selection rules. Nevertheless, they still occur, for twofold reasons. On one hand deformations in the symmetry take place, with the consequence of the loss of the inversion center. On the other hand, two 4f electron configurations with different wave functions sings can mix up. The outcome of these actual forbidden transitions is very interesting, since an extraordinary long life span of excited states can be observed. This life span describes not, as the name suggests, the duration of the excited state existence. Actually it gives information about the time, which is needed untill the excited states decreases to 1/e of its original amount. What makes this so special, is that usually the life span of excited states of other elements is around 10^{-8} - 10^{-10} s. However, the life span of some lanthanides is up to 10^{-2} - 10^{-6} s, that makes them again interesting for various applications, such as lasers, etc.

As previously stated the quite interesting 4f-4f transitions are actually forbidden, but occur due to deviations. Unfortunately, one disadvantageous effect is that these transitions show a very low extinction coefficient. To deal with this problem, lanthanide complexes are synthesized. In such complexes the organic ligand acts as so called photo antenna, it “collects energy” for the Ln-ion. Further details about this can be found in the next section (*I.B.2. Lanthanide Complexes,* page 12). [4] [5]

To conclude this section, a small overview of lanthanide ions and their typical emission lines are given (see figure Figure I.B.5):

Ion	Transition	$\lambda_{emission}$	Ion	Transition	$\lambda_{emission}$
Eu^{3+}	$^5D_0 \rightarrow {}^7F_0$	580 nm	Nd^{3+}	$^4F_{3/2} \rightarrow {}^4F_{9/2}$	880 nm
	$\rightarrow {}^7F_1$	590 nm		$\rightarrow {}^4F_{11/2}$	1060 nm
	$\rightarrow {}^7F_2$	613 nm		$\rightarrow {}^4F_{13/2}$	1330 nm
	$\rightarrow {}^7F_3$	650 nm			
	$\rightarrow {}^7F_4$	690 nm	Er^{3+}	$^4I_{13/2} \rightarrow {}^4I_{15/2}$	1550 nm
	$\rightarrow {}^7F_5$	710 nm			
			Yb^{3+}	$^2F_{5/2} \rightarrow {}^2F_{7/2}$	980 nm
Tb^{3+}	$^5D_4 \rightarrow {}^7F_6$	490 nm			
	$\rightarrow {}^7F_5$	545 nm			
	$\rightarrow {}^7F_4$	590 nm			
	$\rightarrow {}^7F_3$	620 nm			
	$\rightarrow {}^7F_2$	650 nm			

Figure I.B.5: Overview of Eu^{+3}, Tb^{+3}, Nd^{+3}, Er^{+3} and Yb^{+3} ions and their common emission lines [5]

I.B.2. Lanthanide Complexes

In general, lanthanide compounds show very interesting and useful spectroscopic characteristics. Special attention is given to the luminescence properties, which are amongst other things caused by 4f-4f transitions. These effects are not very strong, since they are actually forbidden as mentioned above. But this problem can be circumvented by the synthesis of appropriate Ln-complexes. After an excitation by UV-light, the ligand can transfer energy to the metal center of the complex and thus,an energy exchange takes place. The result is a drastically increased luminescence. The organic ligand acts as a so called Photoantenna and energy donor. In addition, it protects the metal center from external disturbing influences. The lanthanide ion is the corresponding energy acceptor and photo emitter. In order to achieve good values, the selection of the ligands and the structure of the complex play an important role. Therefore, a suitable ligand is characterized by the inclusion of appropriate "light harvesting groups" (for examples aromatic systems) and binding groups (for example carboxylic acids, amides, pyridines).

Usually the complex coordinates through chelat effect. The quantitative properties of the luminescence are described by the quantum yield Q (Q= Number of emitted photons/ Number of absorbed photons). [4] [5]

In figure I.B.6 this intermolecular process is simplified portrayed:

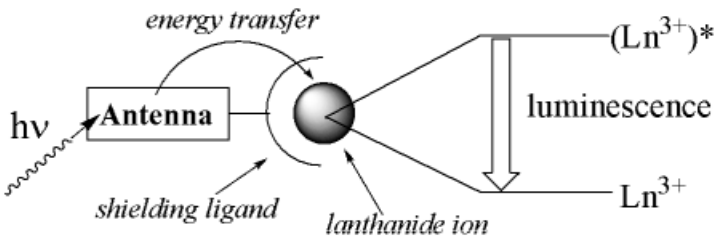

Figure I.B.6: Intermolecular Energy Transfer in Lanthanide Complexes [5]

It is possible to distinct four different groups of lanthanide-complexes based on their spectroscopic characteristics:

The first group with Sm^{3+} ($4f^5$), Eu^{3+} ($4f^6$), Tb^{3+} ($4f^8$), Dy^{3+} ($4f^9$), is the most promising one. It shows the possible strongest emission, which lies in the visible range. The life span of the excited states is quite long and exists between micro- and milliseconds. A reason for the observed emission is the transition from the lowest excited state to the ground state (4f -> 4f).

Another group compromises following Ln-ions: Pr^{3+} ($4f^2$), Nd^{3+} ($4f^3$), Ho^{3+} ($4f^{10}$), Er^{3+} ($4f^{11}$), Tm^{3+} ($4f^{12}$), Yb^{3+} ($4f^{13}$). Compared to the first group the emission intensities are much lower and they appear in the IR range. This is due to very close to each other situated energy differences. [4] [5]

The next group includes some prior mentioned elements but in a lower oxidation states: Ce^{3+} ($4f^1$), Sm^{2+} ($4f^6$), Eu^{2+} ($4f^7$), Yb^{2+} ($4f^{14}$). This change results in significant broader emission bands, which derive from d-f transitions.

Last but not least, the elements with empty, half or completely filled 4f orbitals, namely Sc^{3+} ($4f^0$), Y^{3+} ($4f^0$), La^{3+} ($4f^0$), Lu^{3+} ($4f^{14}$) remain. Due to their electron configuration, no 4f-4f transition can be observed.

The question is how the energy transfer from the ligand to the metal center works. Three simplified mechanisms were introduced, to explain this. One possible option would be the excitation of the ligand from the ground state to an excited Singlet state (S_0 -> S_1) by UV-radiation. Then an intersystem crossing takes place from the excited Singlet state to the excited Triplet state (S_1 -> T_1). Afterwards, an energy transfer to an electron of the metal center (= Ln-ion) of the complex happens. By the relaxation of these electrons, the typical spectral lines of lanthanides are now intensified emitted (portrayed on the left side in figure I.B.7). Another possible mechanism is similar to the first one. However, this time the excited Triplet state is left out and the energy is directly transferred from the excited Singlet state to the electron of the Ln-ion (portrayed in the middle in figure I.B.7). The last proposed mechanism starts again with the excitation of S_0 -> S_1. Then a repeated energy transfer between the excited state of the ligand (S_1, T_1) and the excited state of the lanthanoide-ion (E´, E´´) takes place. In the end again the energy is transferred to an electron of the metal center. Again in both mechanisms the complex emits the characteristic spectral lines of lanthanides (portrayed on the right side in figure I.B.7). [4] [5] A graphic representation of these mechanisms can be found in figure I.B.7:

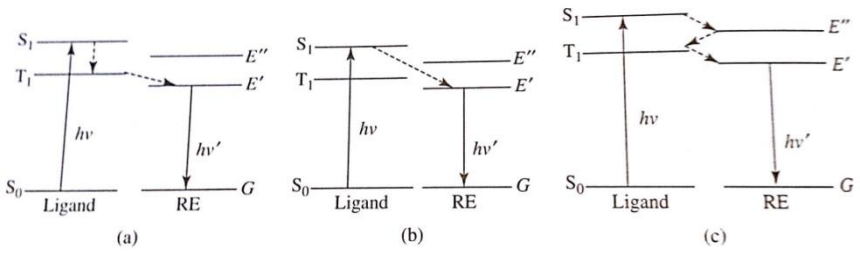

Figure I.B.7: Possible Energy Transitions Mechanism between Ligand and Metal (RE) [4]

After years of research the above described situation is more complicated than first anticipated. Various mechanisms take place simultaneously, such as internal conversion (IC), intersystem crossing (ISC), intra-ligand charge transfer (ILCT/IL) or ligand-to-metal charge transfer (LMCT/LM). Yet again the Singlet and Triplett excited states are used for explanations. It is clear, therefore, that the reaction between ligand and Ln-ions are very attractive and useful, but the mechanisms behind are not so easy to understand. [4] [5]

In figure I.B.8 this advanced energy transfer mechanism from the ligand to the metal center of the complex is shown. No back transfer processes are portrayed for more clearness.

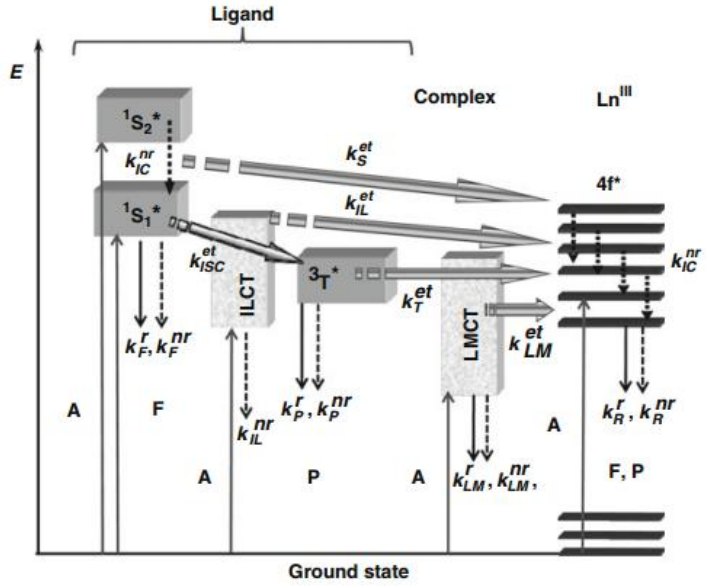

Figure I.B.8: Advanced Energy Transitions Mechanism between Ligand and Metal (RE) [11]

From the general point of view of the HSAB concept, lanthanide-cations are hard acids. Therefore, they tend to react with hard bases such as fluoride or oxide ligands. These ligands are Lewis-Bases, thus, they act as electron donors. However, complexes with N, S and other halides are not very stable in aqueous solutions. To increase their stability, complexes formed by the chelat effect can be used.

Another interesting point can be again found in the isolation of the 4f electrons. Due to barely existing interactions of these electrons with the ligands, the ligand field stabilization energy (LFSE) is quite low. This results in a relatively large amount of various ligand arrangements and coordination numbers. Typical coordination numbers are around six, seven, eight and nine, which explains various geometric arrangements. In general, the binding strengths depend on the ligand and especially its electronegativity.

In figure I.B.9 the typical luminescence spectra of Eu^{+3}-ions in different chemical environments are presented. The spectroscopic properties for this element are amongst other effects caused by transitions from the $^5D_0$ level to several ^7F_x levels (x = 1, 2, 3, 4, 5, and 6). Characteristic for the obtained spectra are sharp peaks, which positions do not depend on ligands or solvents, as one can see in the figure below. However, the intensity and fine structures are influenced by these factors: [4] [5]

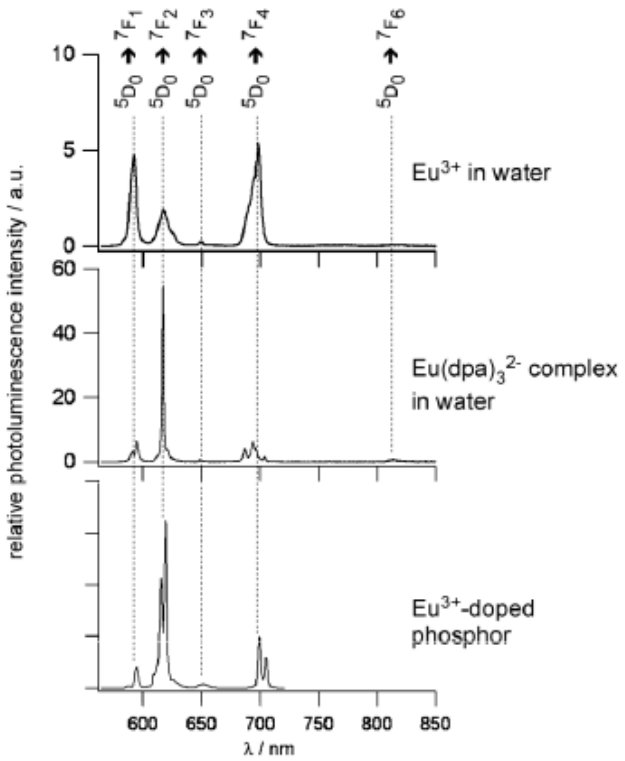

Figure I.B.9: The influence of different environments on the Luminescence Spectra of Eu^{+3}-ions [5]

Many of these interesting and promising characteristics of lanthanide complexes can be found in various researches of the work group of M. Hasegawa. In this context a good example can be found in the paper *Luminescence of fusion materials of polymeric chain-structured lanthanide complexes (*Polymer Journal 47, **2015**, 195–200). [12]

In this work new helical polymeric chain-structured complexes with alternating lanthanide as metal center ($[Eu_x,Tb_{1-x}]$(L)-bdc, $[Eu_x,Tb_{1-x}]$(L)-atpa (= 2-aminoterephtalate) and $[Eu_x,Tb_{1-x}]$(L)-htpa (= 2-hydoloxyterephtalate)) were synthesized and analyzed in regard to their spectroscopic properties and crystal structure. These complexes have promising luminescence properties, which show different emissions/colors depending on the molar ratio of the used lanthanide ions and linker molecules. Another notable feature is that spectroscopic properties can still be observed after heating up to 200 °C. This is due to the specials chain structure of these complexes. In general the Ln-complexes for the reaction with the linker to the polymeric complex were synthesized with a ligand L. This ligand consists of two bipyridine moieties, which are connected through ethylenediamine. In this manner hexadente coordination to the metal center can take place and a satisfying luminescence in the solid state at rt as well as at 77 K can be observed (quantum yield > 50 % for both temperatures). [12]

Promising results were obtained by using the EuL-bdc complex, since analyzes revealed that the advantageous electronic structure of the LnL complex remains the same, whereas changes take place using the other ligands (atpa and htpa) resulting in an amorphous structure.

A pictorial representation of this synthesis can be found in figure I.B.10: [12]

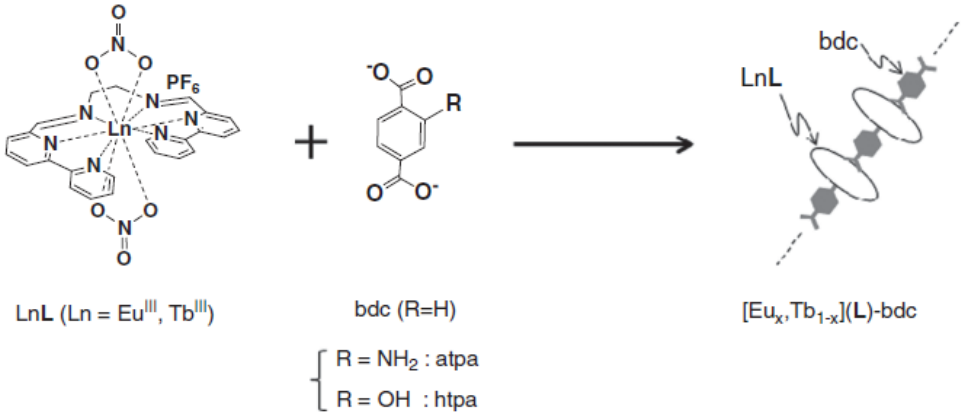

Figure I.B.10: The Fusion of Ln-complexes and Linker to polymeric chain-structured lanthanide complexes [12]

In general this combination of organic ligands and lanthanide elements can be potentially used in wide field of various applications, for example as MOFs (metal organic frameworks) or PCPs (porous coordination polymers) in heterogeneous catalysis, biomedical imaging/sensing, nano-technology and whenever highly luminescent materials are wanted. Therefore, the above introduced helical polymeric complexes are best suitable for several applications due to their excellent luminescence and structure properties, their thermo stability and variation of color. [12] [13]

The promising results of this work are the motivation and basis for this thesis. Three objectives are derived from the above introduced paper: analyses of other linker molecules (namely ndc and acd) and the comparison to the prior used bdc linker, the functionalization of a quartz glass for connection of polymeric chain-structured lanthanide complexes to its surface and last but not least the synthesis of a novel ligand as a potential alternative for the so far used ligand L. These topics are later discussed in detail, see chapter *I.C. Synthesis and Characterization* (page 18).

I.B.3. Applications

Lanthanides find, as mentioned in the chapter above (*I.B.3. Lanthanide Complexes*, page 18), various use in applications through all fields of industry by taking advantage of their unique spectroscopic properties. In many cases, where a special emission of light is needed, for example in flat television or computer screens, appropriate Ln-compounds are required. Various colors can be obtained by using one or a mix of different lanthanides. For instance Eu^{3+} ions emit red and Eu^{2+} ions blue luminescence, a combination of both results in white. Another interesting example for the industrial use of lanthanides in regard to their luminescence properties is the securing of money and passports. In the following figures I.B.4 and I.B.4 the security features, which appear under UV-light, are portrayed: [4] [5]

Figure I.B.4 A 20 Euro note under UV-light, secured by luminescence of Eu-oxides

Figure I.B.4: Austrian Passport under UV-light, secured by the luminescence of various Ln-compounds

Also in other areas, lanthanide elements are very attractive for industrial applications. Rare Earth metals, especially Nd-compounds, find usage in the production of batteries for hybrid cars or engines for wind turbines. This is due to their interesting magnetic properties. Another example is the use as contrast reagent for medical applications. For this purpose, usually Gd(III)-compounds are injected intravenously. This element shows a very paramagnetic behavior and therefore creates contrast. [4] [5]

I.C. Synthesis and Characterization

I.C.1. Goal of this thesis

In general lanthanide-complexes with well-chosen organic ligands, show impressive properties, such as photoluminescene, magnetism and many more. As mentioned above, the reasons therefore are the df transitions and the technically forbidden ff transitions (Laporte rule) within the molecule. The organic ligands of the complexes act as a so called photo antenna, they increase the emission, excited by UV-light, drastically. In this manner the Laporte rule can be circumvented. [4] [5]

The previously introduced work of M. Hasegawa, et all, investigated helical polymeric chain-structured complexes with lanthanides, such as Eu(III), Tb(III) and Gd(III). As linker bdc, atpa and htpa were used. Inspired by the promising results of this work, further researches on this topic were performed in this thesis. [12]

Firstly the synthesis of polymeric Eu-complexes using bdc, ncd (1,4-naphthalenedicarboxylic acid) and adc (9,10-anthracenedicarboxylic acid) as ligand/linker was carried out. These synthesized complexes were analyzed with regard to their luminescence properties. Furthermore, the surface of a quartz glass was appropriately cleaned and functionalized to prospectively connect polymeric Eu-complexes to it. In this manner, it is planned to expand the range of applications.

Last but not least, the synthesis of a new ligand, namely N,N^{I}-(Ethane-1,2-diyl)-bis(1,10-phenanthroline-2-yl)methanimin, succeeded. At a first sight, this ligand appears very similar to the one used in the work of M. Hasegawa (see figure I.C.1). However, the previously used ligand has two bipyridine moieties, which are bridged over an ethylenediamine unit. Whereas the ligand from this thesis has a 1,10-phenantrholine structure, which is an annulated and bigger compound. Due to these changes, it can be expected that the usage of this newly synthesized ligand shows an even better luminescence behavior after the coordination, compared to the previous one. Reason therefore is the overlapping of π-orbitals in the annulated system (see figure I.C.1 below). [12] [21]

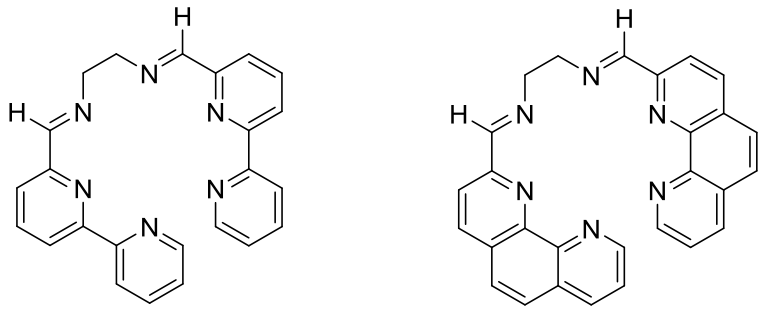

previously used ligand (L) newly synthesized ligand

Figure I.C.1: Previously used and newly synthesized ligand

I.C.2. Synthesis of Eu-Complexes

In the following paragraphs the performed syntheses and their results are discussed in detail.

I.C.2.1.1. $Eu(phen)_2(NO)_3$

As an introduction to this kind of chemistry the synthesis of the $Eu(phen)_2(NO_3)_3$ was performed. The coordination was carried out in abs. EtOH at rt. At these conditions the complexation of the phen (2 eq) to the center of an Eu compound ($Eu(NO_3)*6H_2O$, 1 eq) started immediately. The progress of the reaction could be observed under UV-light. After the addition of the lanthanide to the ligand in an alcoholic solution, immediately a red glow occurred, caused by the luminescence of the formed $Eu(phen)_2(NO)_3$ complex. This indicates the formation of an Eu(III)-complex. Whereas blue luminescence arises from complexed Eu(II)-ions. In figure I.C.2 the chemical reaction of this experiment is portrayed: [4] [14] [15]

Figure I.C.2: Luminescence of the formed $Eu(phen)_2(NO)_3$ complex

Overall a satisfying yield of 82.6 % was achieved. The analysis was done by luminescence spectroscopy.

I.C.2.1.2. Analysis of $Eu(phen)_2(NO)_3$

Luminescence spectroscopy was performed on a Horiba Jobin-Ybon Fluorolog 3–22 with appropriate UV cut filter at rt. The prior obtained compound was solved in abs. ACN. The range of the measurement was between 550 and 750 nm, which is typical for this kind of Eu(III)-complex. For the excitation four different wavelengths λ_{EX} were chosen: λ_{EX} = 290, 312, 320 and 330 nm. Due to previous work, the excitation wavelengths were known already. [5] [12]

In figure I.C.3 the results of this analysis are shown:

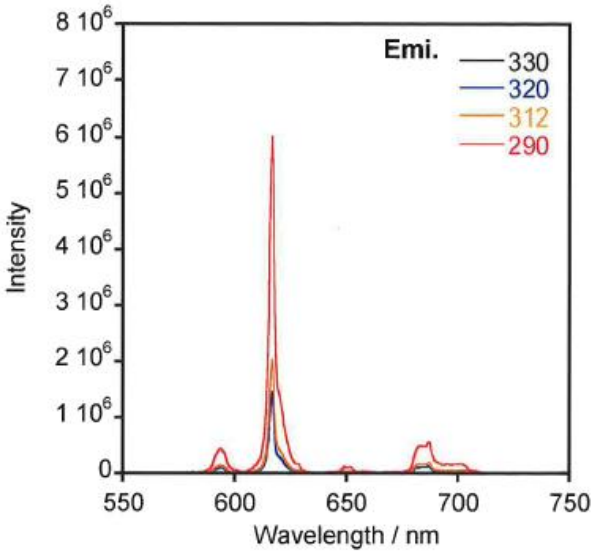

Figure I.C.3: Luminescence Spectrum of $Eu(phen)_2(NO)_3$ complex in ACN at room temperature

It could be observed that the previously synthesized compound showed a typical luminescence spectra for an Eu(III)-complex. In general, this kind of spectra show sharp peaks, as one can see also in figure I.C.3. The positions of the peaks in the spectra are not depending on the used ligands, however, the intensities and fine structures are. The peaks are caused by the radiative transitions from the $^5D_0$ level to several F levels. A closer look into figure C.3 shows that there are four peaks of importance. The first one around 590 nm is caused by $^5D_0$ to $^7F_1$ transitions, the second at 615 nm by $^5D_0$ to $^7F_2$ transitions, the hardly visible peak at 650 nm by $^5D_0$ to $^7F_3$ transitions and last but not least the peak around 680 nm by $^5D_0$ to $^7F_4$ transitions. In addition, a fine structure can be observed in regard to the first peak from right (around 690 nm). The reason for this is the so called crystal field splitting. More details on the theoretical background can be found above under point (*I.B.2. Lanthanide Complexes*, page 12). [5]

According to these results, the formation of the desired complex was succesfully!

I.C.2.2.1. Eu(bdc/ndc/adc)$(NO_3)_3$

The aim of this part was to synthesize polymeric Eu-complexes with various different ligands and to analyze them in regard to their luminescence properties. In this way an appropriate linker molecule for the later formation of helical polymeric chain-structured complexes could be found. As Eu-precursor, again $Eu(NO_3)*6H_2O$ was used and this time it was reacted with aromatic carboxylic acids or its salt (bdc, ndc and adc). These ligands were chosen because of their structure and the resulting possible use as photo antenna. [12]

The general synthesis scheme for the performed reactions can be found in figure I.C.4 below: [14] [15]

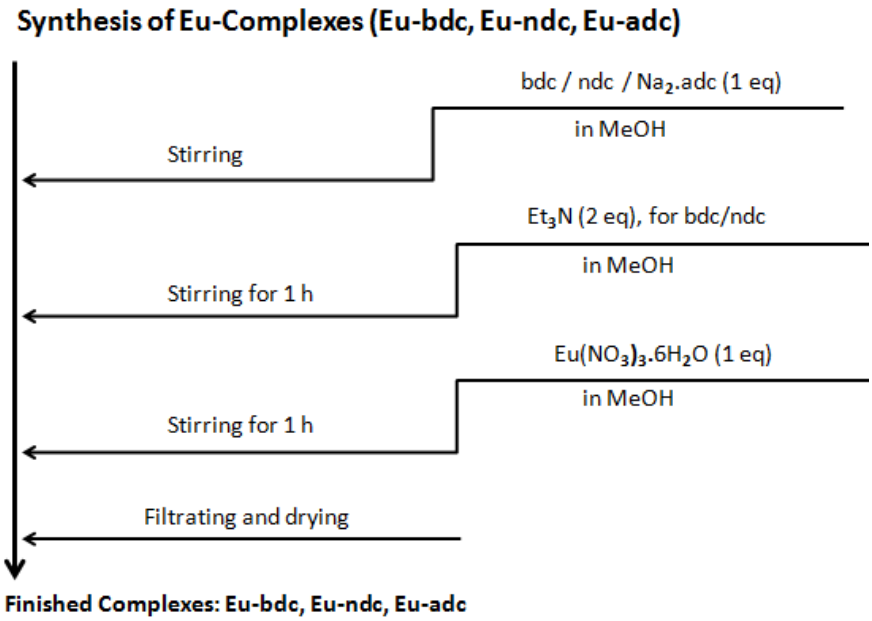

Figure I.C.4: Synthesis Scheme for Eu-complexes

The experiments worked very well, as quite satisfying yields were obtained for each reaction (70.2 % of Th. for Eu(bdc)$(NO_3)_3$, 70 % of Th. for Eu(ndc)$(NO_3)_3$ and 60.5 % of Th. for Eu(adc)$(NO_3)_3$). Unfortunately the molar ratios for the reaction with bdc and ndc could not precisely met, due to a calculation mistake and weighing failures (see point *I.D.4.1.2.* and *I.D.4.1.3.*, page 32 and 33). The comparatively low results in regard to the yield of the reaction with adc can probably be explained by the structure of the ligand itself. Adc is the largest and bulkiest ligand compared to the others, therefore, the coordination of it to the metal center may be disturbed.

Nevertheless, the resulting yields of all experiments were more than enough to continue with the analyses by luminescence spectroscopy.

I.C.2.2.2. Analysis of of Eu(bdc/ndc/adc)$(NO_3)_3$

The synthesized complexes were analyzed in the same manner as before, by luminescence spectroscopy. The measurements were again performed at rt, but this time the complexes were not dissolved, since their properties in the solid state were of interest.

The measurement range was selected again between 550 and 750 nm. For the excitation several wavelengths λ_{EX} were chosen, due to previous works. [5] [12] The used wavelengths can be found in the right corner of the respective diagrams. In the following figures I.C.5, C.6 and I.C.7 are shown the results of the luminescence spectroscopy for each complex:

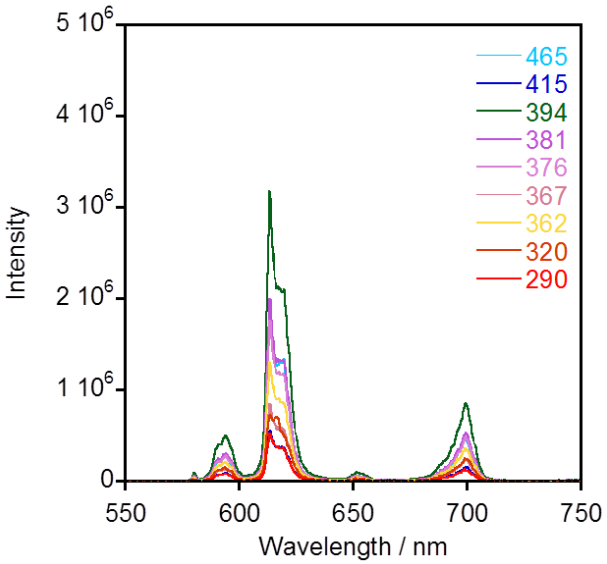

Figure I.C.5: Luminescence Spectrum of $Eu(bdc)(NO_3)_3$ complex in the solid state at room temperature

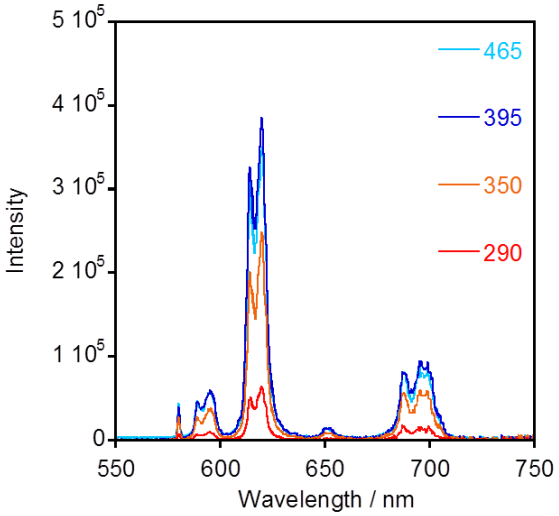

Figure I.C.6: Luminescence Spectrum of $Eu(ndc)(NO_3)_3$ complex in the solid state at room temperature

As shown in the figures I.C.5 and I.C.6 the luminescence spectra are very similar to each other in terms of their peak positions. The occurrence and position of the peaks is again due to radiative transitions from the $^5D_0$ level to several F levels, as it is usual for this kind of Eu(III) complex (see point *I.C.2.1.2. Analysis of $Eu(phen)_2(NO)_3$*, page 20). Thus, it can be said that the desired complexes were successfully synthesized. In terms of intensity it is clear to see that the Eu-complex with bdc as ligand achieved higher values than the one with ndc ($4*10^6$ vs $4*10^5$). This could be due to steric effects, since ndc shows an annulated, bigger ring system in contrast to bdc, which consist of only one aromatic benzene ring. To verify this assumption further analyzes like XRD measurements would be necessary. [5] [12]

In figure I.C.7 the luminescence spectrum of the $Eu(adc)(NO_3)_3$ complex are shown:

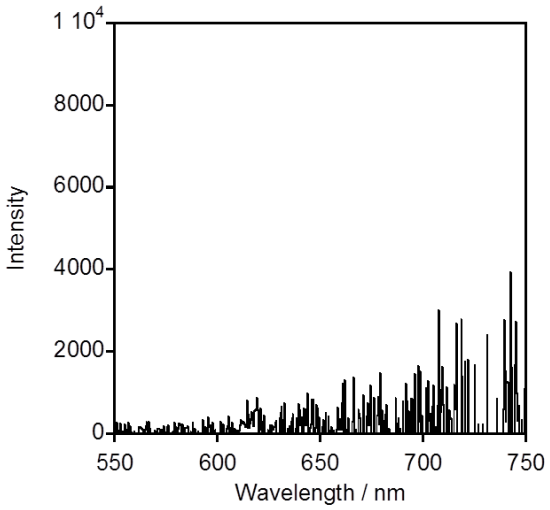

Figure I.C.7: Luminescence Spectrum of $Eu(adc)(NO_3)_3$ complex in the solid state at room temperature

It can clearly be seen that no luminescence could be measured for this complex and only background noise can be observed. This may be due the above mentioned steric reasons. Adc is the biggest and most sterically hindered used ligand of all. It might be reasonable to assume that some kind of reaction took place, but not the preferred formation of a polymeric chain-structured complex. But to verify this consideration, further measurements, especially XRD, etc., have to be performed.

In summary, it can be said that the best results were achieved by using bdc as ligand/linker. This complex showed the best results in regard to luminescence properties. The consideration to get a better photo antenna by using bigger, annulated ligands is probably due to steric interferences of these compounds. But as mentioned before, further experiments have to be performed to support this idea.

All in all bdc is the most suitable ligand compared to the others for further experiments. These results align with the previous work of M. Hasegawa. [12]

I.C.3. Development of Thin Films with Helical Eu-Complexes Using Self-Assembling Materials

I.C.3.1. Cleaning of the Surface

Before the functionalization of the glass surface could be started, it was necessary to clean it in an appropriate way from organic and inorganic residues, because they can interfere in later reactions. In the literature several methods are suggested for this kind of process. Due to its simple handling and easy accessibility of materials, the literature procedure described in [16] was chosen.

I.C.3.2. Functionalization of the Surface

After cleaning the surface its functionalization could be carried out. In general, this process was done as described in [17] with slight variations, which were proposed of M. Hasegawa. In this manner, a carboxylic acid group was introduced to the quartz glass surface. To confirm this reaction, further analyzes by FT-IR are in progress.

With this modification, it should be possible to connect an Eu-complex to the glass surface, by previously deproteinizing the carboxylic acid group with an appropriate base. Once this step is carried out, the next task will be to form a polymeric chain-structured complex layer by layer, by using alternately Eu-complexes and linker. As mentioned above in point *I.C.2.2.2. Analysis of of Eu(bdc/ndc/adc)(NO_3)$_3$,* (page 21) bdc showed the best results in terms of luminescence properties. This result was also confirmed by previous experiments. As a result, this ligand would be ideally suited as linker for this kind of reaction.
In this manner, it is hopefully possible to achieve poylmeric chain-structured complexes on the surface of quartz glass pieces with promising photoluminescence properties, like in the previous work of M. Hasegawa. Diverse analysis methods such as luminescence and polarized luminescence spectroscopy, FT-IR, XRD, etc can be used to confirm the structure of such complexes. Also, the usage of other ligands and lanthanides, such as Nd, Tb or the combination of several different elements, would be of great interest. [12]

I.C.4. Synthesis of N,N^{I}-(Ethane-1,2-diyl)-bis(1,10-phenanthroline-2-yl)methanimin

This point covers the tree-step synthesis of the target molecule N,N^{I}-(Ethane-1,2-diyl)-bis(1,10-phenanthroline-2-yl)methanimin.These experiments were carried out under the consultation of Dr. M. Mastalir.

I.C.4.1. 2-Methyl-1,10-phenanthroline

The first part of this three-step synthesis was the methylation of 1,10-phenanthroline. Therefore, MeLi was used, which is one of the strongest nucleophilic methylation reagents available. Subsequently it was necessary to restore the aromaticity of the system by using MnO_2 as oxidizing agent. [18] The general reaction mechanism is shown in figure I.C.8 below: [20]

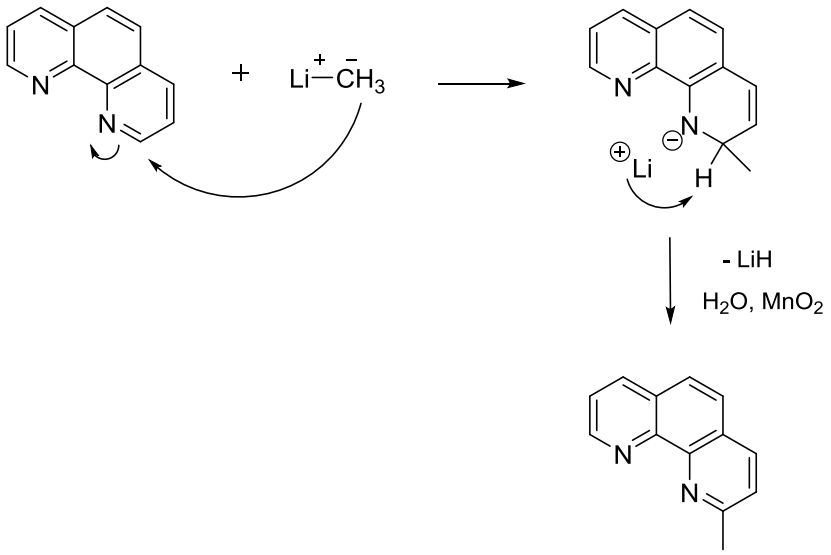

Figure I.C.8: General Mechanism of the Methylation and Rearomatization

MeLi is a strongly polarized compound, which attacks the system in a position next to an N atom. In this way a methyl group is introduced into the compound. By quenching the reaction with water carefully, the reaction is stopped, leaving a methylated but dearomatized compound. To return to the previous aromatic state, activated MnO_2 is used. To avoid double methylation, it is necessary to use both starting materials in a molar ratio of 1:1. [20]

For the reaction itself it was most important to work strictly under inert conditions. This was due to two reasons. Firstly the starting material 1,10-phenanthroline is a very hygroscopic compound. Therefore it was weighed in a glove box, to avoid unwanted reaction with the humidity from air. Secondly MeLi is a highly reactive compound, which can be handled under inert conditions only and in solvents like THF. In order to prevent unwanted reactions, the used solvent (THF) had to be absolutized with Na and the reaction was carried out under argon atmosphere.

The subsequently quenching and working up process was performed again under air. For the rearomatization of the system, as mentioned above, MnO_2 was used. In general, the results were satisfying with an overall yield of 54.3 %. No further purifications were necessary, due to a crystallization process of the crude product with pentan.

^{1}H NMR spectra was carried out for characterization (see chapter *I.F. Appendix*, page 40).

I.C.4.2. 1,10-Phenanthroline-2-carbaldehyde

The second step of the ligand synthesis was the selective reaction of the previously introduced methyl group to the corresponding aldehyde. This reaction was carried out with the prior synthesized 2-Methyl-1,10-phenanthroline (1eq) and SeO_2 (2 eq) in abs. 1,4-dioxane.[19] Selenium dioxide is a very useful chemical for this kind of oxidation reaction. The general mechanism of the reaction is portrayed in figure I.C.9 below: [20]

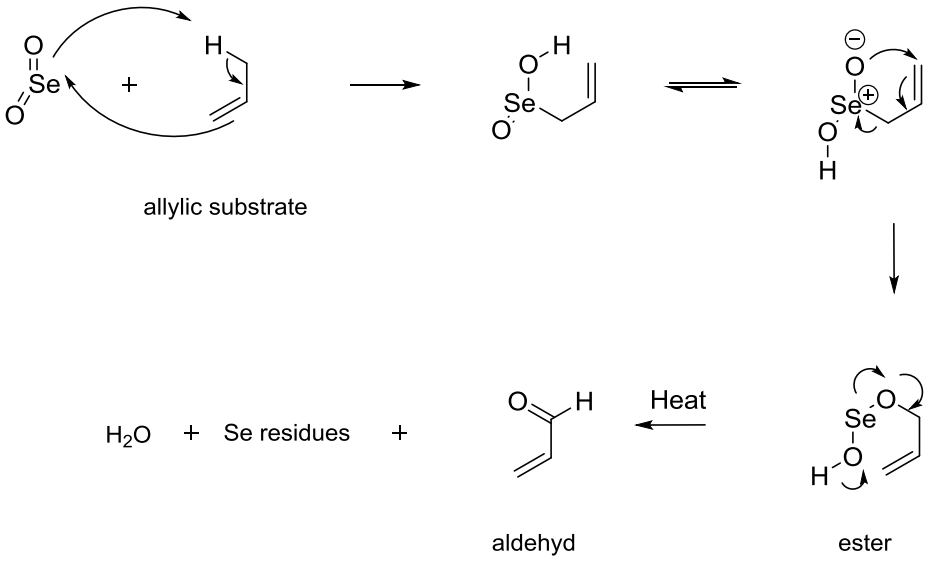

Figure I.C.9: General Mechanism of the Riley Oxidation

At first, the oxidation reagent SeO_2 reacts with the allylic substrate in a nucleophilic reaction. A so called pericyclic process takes place. Thereby the double bond attacks at one Se atom, a proton is transferred to an O atom and a new double bond is formed. After some electron pair rearrangements an ester of a kind of selenious acid is formed. This ester decomposes in heat to the desired aldehyde, water and different Se residues. During this reaction it is not necessary to work under inert conditions, since it is a straightforward oxidation process. [20]

Within this step, it was very important to check the reaction process constantly by TLC to avoid the decomposition of the formed product in the heat. The color change from pale yellow to dark brownish red under reflux conditions was a sign for the oxidation process. Afterwards it was necessary to separate the emerging, interfering Se-compounds from the product. Otherwise these residues would be a disturbance in the next step. Therefore, the reaction mixture was mixed with activated carbon after what a hot filtration over celite was performed. A repeated filtration again over celite resulted in the purified ligand. For another attempt celite was replace with Al_2O_3 in anticipation of a better fractionation.

It was found however that the product had decomposed due to the too alkaline environment. In this manner hardyl any product was received and analyzes by ^{1}H-NMR showed many impurities decompositions products.

Overall a yield of 46.6 % was obtained for this reaction. In order to receive a higher yield, the reaction mixture was filtrated over celite just once in another experiment. By doing so, a higher yield was achieved, unfortunately with a simultaneous decrease in its purity. Purification methods like recrystallization did not work and column chromatography is excluded due to a decomposition of the product in a basic milieu.

^{1}H-NMR spectra were carried out for characterization (see chapter *I.F. Appendix*, page 40).

I.C.4.3. N,N^{I}-(Ethane-1,2-diyl)-bis(1,10-phenanthroline-2-yl)methanimine

The last step for this three-step synthesis was the reaction of the previously synthesized aldehyde with a primary amine (in this case ethylenediamine with corresponding two functional groups) in iPrOH. In this reaction two equivalents of the aldehyde and one equivalent of the amine form a Diimine, the desired target compound. [21]

The mechanism of this synthesis is shown in a simplified manner in figure I.C.10:

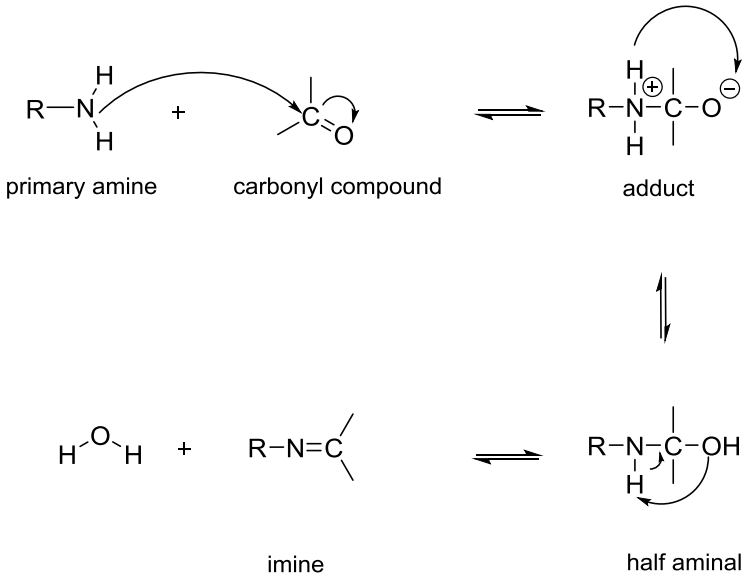

Figure I.C.10: General Mechanism of the Synthesis of an Imine under neutral conditions

In general imines are synthesized by the reaction of primary amines and aldehydes or ketones. At first a nucelophilic addition takes place and a dipolar ion with a positive charged N-atom and a negative charged O-atom is formed.

The so evolved adduct forms in a reversible step an instable half aminal by proton changing. This compound decomposes in an elimination reaction to the desired imine (also called azomethine) and water. The described reaction is performed under neutral conditions. Better results may be achieved by using the appropriate amount of acid as catalyst. All the steps are reversible in aqueous solutions, although it is not possible to isolate the half aminal.

The results of these reactions were quite satisfying with an overall yield of 38.1 %. A higher yield may be obtained, as described above, by carrying out the reaction with the addition of an acid as catalyst. Additionally, an appropriate purification method for the target compound is sought, since recrystallization did not work well and column chromatography is excluded due to decomposition of the product.

^{1}H and ^{13}C- NMR spectra were carried out for characterization (see chapter *F. Appendix*, page 40).

I.D. Experimental

I.D.1. General Remarks

In the following chapter the syntheses described above are shown and discussed in detail. Generally, the reagents for the syntheses were purchased from commercial suppliers. In this case they were used without further purification. Any exceptions are mentioned directly in the particular experiments.

Anhydrous solvents like tetrahydrofuran, 1,4-dioxane, etc. were purified by the PURESLOV-system from it-innovative-technology-inc. Furthermore THF was additionally absolutized with sodium.

The commercially available lithiation reagent MeLi was used without further quantitative analysis due to its hazardous characteristics, using the declared value.

I.D.2. Chromatographic Methods

Thin layer chromatography was performed by using TLC aluminium foil (Merck, Silica gel 60 F_{254}).

I.D.3. Analysis Methods

I.D.3.1. NMR-Spectroscopy

NMR Spectra were recorded at 200 MHZ on a Bruker Avance 200 and at 250 MHZ on a Bruker Avance 250. For ^{1}H measurements both devices were used, for ^{13}C only the latter one was used due its slightly better resolution.

Data for ^{1}H NMR are reported as follows: Chemical shift in parts per million (ppm) with TMS (tetramethylsilane) as an internal standard, with the residual solvent signal as an internal reference, multiplicity (s = singlet, d = doublet, t = triplet, q = quadruplet and m = multiplet), coupling constant in Hz and after integration.

Data for ^{13}C are reported in ppm with TMS as an internal standard, using the central peak of the solvent as reference, multiplicity with respect to the protons deduced from APT experiments (s = quarternary C, d = CH, t = CH_2, q = CH_3). [22]

I.D.3.2. Luminescence-Spectroscopy

Luminescence spectra were recorded on a Horiba Jobin-Ybon Fluorolog 3–22 with an appropriate UV cut filter. [23]

I.D.4.1. Synthesis of Eu-Complexes

I.D.4.1.1. $Eu(phen)_2(NO_3)_3$

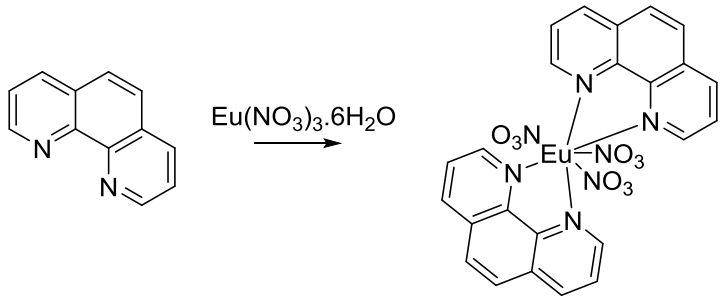

$C_{12}H_8N_2$	$H_{12}EuN_3O_{15}$	$C_{24}H_{16}EuN_7O_9$
180.21	446.07	698.40

Figure I.D.1: Synthesis of $Eu(phen)_2(NO_3)_3$

Synthesis according to [14] [15]:

1,10-Phenathroline (30 mg, 1.66 mmol, 2 eq) was transferred into 2 ml of absolute Ethanol and stirred until it was dissolved completely. $Eu(NO_3)*6H_2O$ (34.5 mg, 0.083 mmol, 1 eq) was solved in 2 ml of abs. EtOH as well and this solution was added drop wise to the previously prepared solution. The mixture was stirred for about ten minutes. Under UV-light a bright red luminescence could be observed due to the complexation. After five minutes a white solid was formed, which was filtered and washed with abs. EtOH. The in this manner obtained white powder was dried under vacuum. A yield of 44.6 mg could be achieved. (82.6 % of Th.)

Analyzed by Luminescence Spectroscopy (see figure I. C.3).

I.D.4.1.2. Eu(bdc)$(NO_3)_3$

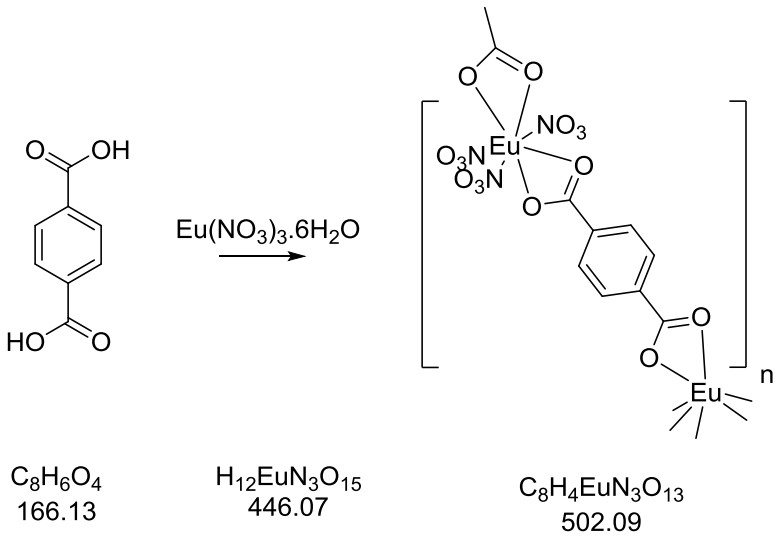

Figure I.D.2: Synthesis of Eu(bdc)$(NO_3)_3$

Synthesis according to [14] [15]:

Terephthalic acid (11.6 mg, 0.07 mmol, 1 eq) was transferred into 20 ml of absolute MeOH and stirred until it was dissolved completely. Meanwhile triethylamine (16.3 mg, 0.16 mmol, 2.8 eq, 101.19 g/mol) was dissolved in 5 ml abs. MeOH. Both prepared solutions were combined and stirred for one hour.

In a next step $Eu(NO_3)*6H_2O$ (49.2 mg, 0.11 mmol, 1.57 eq.) was dissolved in 2 ml of abs. MeOH and after one hour added drop wise to the previously prepared reaction mixture. A few minutes later a white precipitate was formed. Under UV-light a bright red luminescence due to the complexation process could be observed. After a reaction time of one hour the solid was filtered off and washed with abs. MeOH. The obtained white powder was dried under vacuum. A yield of 24.6 mg could be achieved. (70.2 % of Th.)

Analyzed by Luminescence Spectroscopy (see figure I.C.5).

I.D.4.1.3. Eu(ndc)$(NO_3)_3$

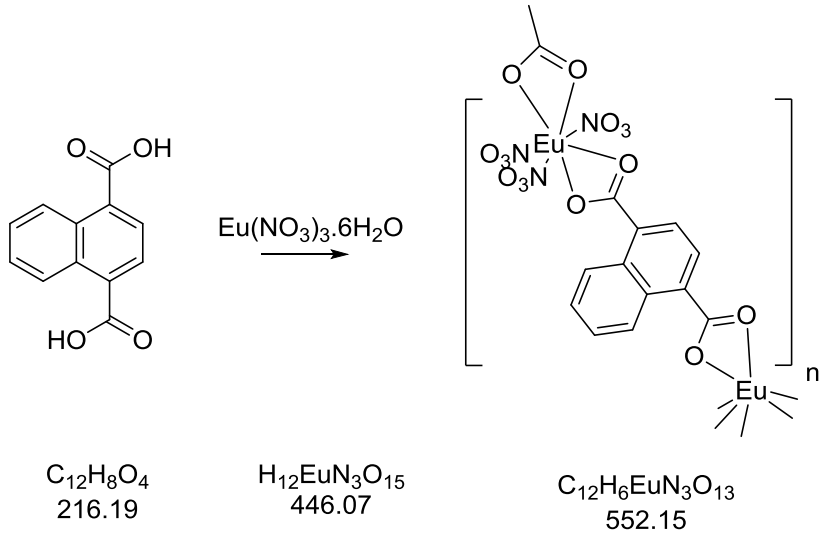

Figure I.D.3: Synthesis of Eu(ndc)$(NO_3)_3$

Synthesis according to [14] [15]:

In the same procedure as for *D.4.1.2. Eu-bdc,* 1,4-naphthalenedicarboxylic acid (14.8 mg, 0.07 mmol, 1 eq) was transferred into 20 ml of absolute MeOH and stirred until it was dissolved completely. Triethylamine (17.1 mg, 0.17 mmol, 2.4 eq, 101.19 g/mol) was dissolved in 5 ml abs. MeOH. Both solutions were combined and stirred for one hour.

Meanwhile Eu(NO_3)*$6H_2O$ (51.4 mg, 0.12 mmol, 1.71 eq.) was dissolved in 2 ml of abs. EtOH and after one hour added drop wise to the previously prepared reaction mixture. A few minutes later a white precipitate started to be formed. Under UV-light a weak red luminescence due to the complexation process could be observed. After one hour the solid was filtered and washed with abs. MeOH. The obtained white powder was dried under vacuum. A yield of 25.7 mg could be achieved. (70 % of Th.)

Analyzed by Luminescence Spectroscopy (see figure I C.6).

I.D.4.1.4. Eu(adc)$(NO_3)_3$

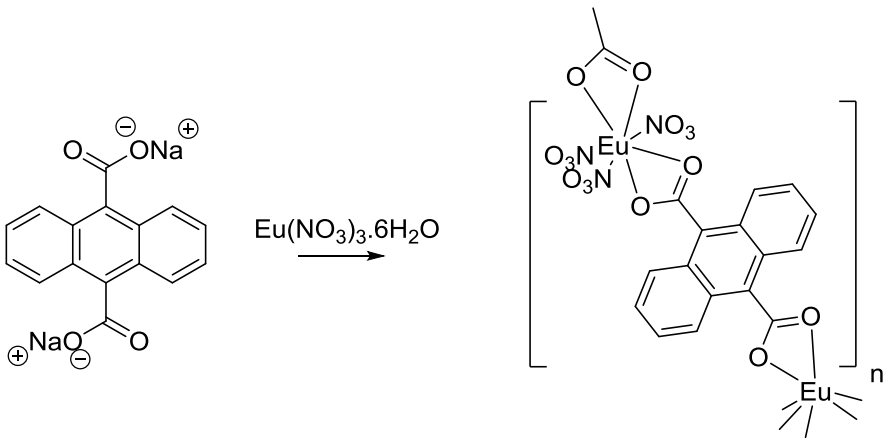

$C_{16}H_8Na_2O_4$ 310.22

$H_{12}EuN_3O_{15}$ 446.07

$C_{12}H_6EuN_3O_{13}$ 602.21

Figure I.D.4: Synthesis of Eu(adc)$(NO_3)_3$

Synthesis according to [14] [5]:

The salt of 9,10-anthracenedicarboxylic acid (34.77 mg, 0.11 mmol, 1 eq.) was transferred in 20 ml of absolute MeOH and stirred until completely solved. Meanwhile Eu(NO_3)*$6H_2O$ (50 mg, 0.11 mmol, 1 eq.) was dissolved in 2 ml of abs. MeOH and this solution was added drop wise to the previously dissolved ligand. Under UV-light no luminescence due could be observed. The mixture was stirred for about one hour, after five minutes a white solid was formed. This precipitation was filtered off and washed with abs. MeOH. The obtained white powder was dried under vacuum. A yield of 40.6 mg could be achieved. (60.5 % of Th.)

Analyzed by Luminescence Spectra (see figure I.C.7).

I.D.4.2. Development of Thin Films with Helical Eu-Complexes Using Self-Assembling Materials

I.D.4.2.1. Cleaning of the Surface

Procedure according to [16]:

Before developing an anchor group on the glass surface, it was necessary to clean its surface in an appropriate way. Therefore, thin pieces (thickness about 1 mm) of regular SiO_2 quartz glass were cut into small pieces with about 1 cm length and 4 mm with.

As a first step a solution of 5 ml MeOH and 5 ml HCl (12M) was prepared. The glass pieces were put into this solution for 30 minutes and additionally in an ultrasonic bath. Afterwards the samples were carefully rinsed with ultra pure deionized water and transferred into 10 ml H_2SO_4 (12 M), and then again for 30 minutes into the ultrasonic bath. As before the glass pieces were rinsed with ultra pure deionized water.

The final step before the functionalization was a last bath in ultra pure deionized water for 60 minutes in an ultrasonic bath. At the end of this time the samples were dried and ready for further treatments.

I.D.4.2.2. Functionalization of the Surface

Procedure according to [17] and adjusting by M. Hasegawa:

For the functionalization of the surface a solution of 0.1 ml aminopropyltriethoxysilane in 10 ml toluene was prepared. The glass pieces were added to this solution and were kept in there for one hour. Afterward the samples were cleaned with pure toluene and dried with pressured air.

For the next step the glass pieces were transferred into a solution of 330 mg of glutaric anhydride in 10 ml DMF. The temperature of the reaction solution was heated up to 60 °C and maintained for nine hours. After this time the glass samples were rinsed with pure DMF and again dried with pressured air.

In figure I.D.5 a step by step visualization of this procedure is shown:

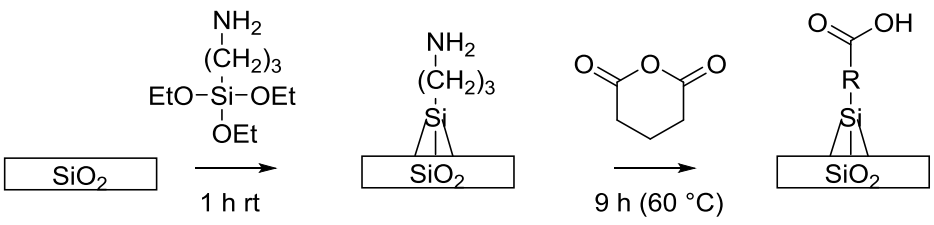

Figure I.D.5: Functionalization of the Surface

I.D.4.3. Synthesis of N,N^{I}-(Ethane-1,2-diyl)-bis(1,10-phenanthroline-2-yl)methanimin

I.D.4.3.1. 2-Methyl-1,10-phenanthroline

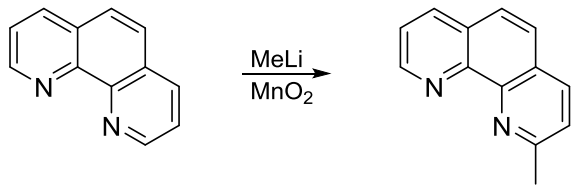

$C_{12}H_8N_2$
180.21

$C_{13}H_{10}N_2$
194.24

Figure I.D.6: Synthesis of 2-Methyl-1,10-phenanthroline

Synthesis according to [18]:

Before the reaction was started it was necessary to absolutize THF. Therefore the solvent was refluxed with elemental sodium for five hours (under an argon atmosphere).

Methyllithium (1,6 mol/dm^3 in Et_2O, 34.98 ml, 55.77 mmol, 1 eq.) was added to 150 ml of the absolutized THF, again under inert conditions. The MeLi flask was well shaken to avoid inhomogeneities before the usage. The so prepared solution was cooled down to -10 °C and kept under argon atmosphere.

1,10-Phenanthroline (10.05 g, 55.77 mmol, 1 eq.) was weighed in a glove box, to avoid a reaction with humidity in the air. The hygroscopic educt was transferred in about 100 ml absolute THF. This suspension was added quickly under strong stirring to the cooled solution of MeLi under argon. During the addition, the temperature was kept at -10 °C and immediately a change in color from clear to dark violet could be observed. The residues of 1,10-Phenanthroline were thoroughly washed into the reaction flask with small amounts of absolute THF. Afterwards the reaction mixture was allowed to warm up to rt and stirred overnight. During this period the reaction mixture was kept under an argon atmosphere.

At the next day, the reaction mixture was cooled down with an ice bath and 25 ml of brine were added carefully to the reaction mixture in order to quench it. Then it was transferred into a separation funnel and 50 ml of brine were added. Residues in the reaction flask were washed with Et_2O afterwards.

The organic layer and water layer were separated. The organic layer was then extracted with 100 ml of water. At this time the water phase was milky and cloudy. After this extraction process, the organic layer was isolated and evaporated untill about ¼ of the solution was left.

For the next step 400 ml Et_2O were added to the so prepared solvent. Under strong stirring, activated MnO_2 (62.4 g, 0.72 mol, 86.94 g/mol) was transferred in small portions to the reaction solution. After the addition, it was necessary to stir the mixture for two hours. After this time $MgSO_4$ was added to the reaction mixture for drying. Again the reaction was stirred for two hours. Subsequently the reaction mixture was filtrated through a glass filter filled with celite. The filter cake was washed several times with Et_2O. In this manner, a clear, yellow solution was achieved, which was evaporated till dryness. The so obtained yellowish oil was coated with 50 ml pentane and kept overnight in the refrigerator.

At the next day a beige solid was formed. This solid was obtained by filtration, several times washed with cold pentane and dried. In this way 5.85 g of a white-beige solid were obtained. (54.3 % of Th.)

Analyzed by ^1H NMR:

200 MHz, DMSO	δ = 9.08 (d, J = 2.77 Hz, 1H), 8.50 (d, J = 9.07 Hz, 1H), 8.32 (d, J = 8.2 Hz, 1H), 7.92 (s, 2H), 7.74 (dd, J = 4.22, 3.78 Hz, 1H), 7.64 (d, J = 8.22 Hz), 2.78 (s, 3H) ppm.

I.D.4.3.2. 1,10-Phenanthroline-2-carbaldehyde

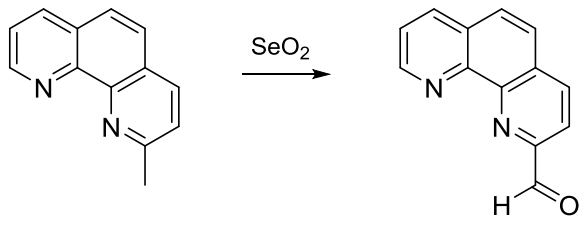

$C_{13}H_{10}N_2$
194.24

$C_{13}H_8N_2O$
208.22

Figure I.D.7: Synthesis of 1,10-Phenanthroline-2-carbaldehyde

Synthesis according to [19]:

As a first step it was necessary to dissolve the previously synthesized 2-Metyl-1,10-phenanthroline (500 mg, 2.57 mmol, 1 eq) in dry 1,4-dioxane. Afterwards SeO_2 (573 mg, 5.15 mmol, 2 eq, 110.96 g/mol) was added to the solution. The reaction mixture was heated under reflux conditions for about 80 minutes. It could be observed that the solution turned its color from clear to yellowish, to bright red up to a dark, brownish red. The progress of the reaction was checked every 10 minutes by TLC (solvent mixture: EE 9-8 parts : MeOH 1-2 parts : NH_3 (25%) 2 drops).

After about 80 minutes the reaction was finished according to TLC. A little bit of activated carbon was added and the mixture and was stirred for further five minutes. Afterwards the hot solution was filtrated over celite. In this manner a bright yellow filtrate was obtained. Since the product was not very good soluble in 1,4 dioxane, the filter bed was washed several times with Et_2O. By doing so, a white turbidity occurred in the filtrate. The so obtained filtrate was evaporated untill dryness and then dissolved in EE. A little bit of activated carbon was added and the solution was again filtrated through Celite. A pale yellow filtrate was obtained and again evaporated untill dryness.

In this manner 250 mg of a yellowish white solid were obtained. (46.6 % of Th.)

Analyzed by ^{1}H NMR:

250 MHz, DMSO δ = 10.31 (s, 1H), 9.20 (dd, J = 2.58, 1.70 Hz, 1H), 8.72 (d, J = 8.23 Hz, 1H), 8.58 (dd, J = 6.42, 1.68 Hz, 1H), 8.25 (d, J = 8.25 Hz, 1H), 8.15 (q, J = 8.84, 6.26 Hz, 2H), 7.85 (dd, J = 4.35, 3.76 Hz, 1H) ppm.

I.D.4.3.3. N,N^{I}-(Ethane-1,2-diyl)-bis(1,10-phenanthroline-2-yl)methanimin

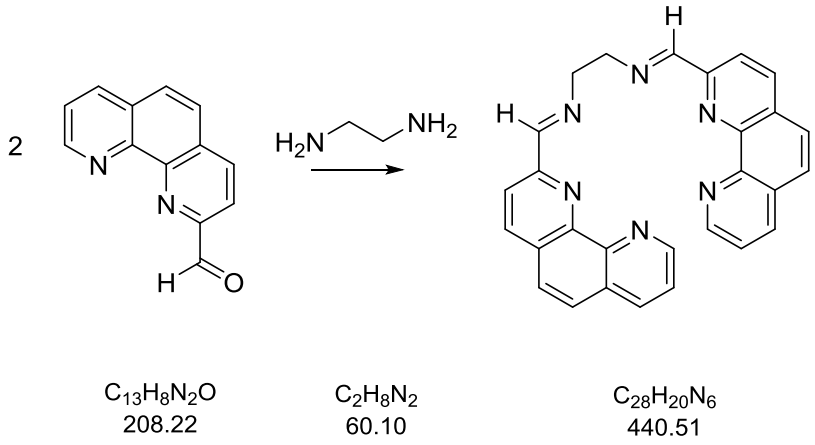

Figure I.D.8: Synthesis of N,NI-(Ethane-1,2-diyl)-bis(1,10-phenanthroline-2-yl)methanimin

Synthesis according to [21]:

At first it was necessary to distill ethylenediamine over $CaCl_2$ to dry it. Afterwards a solution of 1,10-Phenanthroline-2-carbaldehyde (537 mg, 2.6 mmol, 2.2 eq) in 5 ml iPrOH was prepared. Then the purified ethylenediamine (69.58 mg, 1.16 mmol, 1 eq) was quickly added to the solution with a syringe to avoid reactions of the educt with humidity from air.

After five minutes a yellow solid started to precipitate, which was filtrated off. The yellow precipitant was afterwards washed with a small amount of cold Et_2O and dried under vacuum.

In this manner 433 mg of a yellowish white solid was obtained. (38.1 % of Th.)

Analyzed by ^{1}H NMR:

250 MHz, $CDCl_3$ δ = 8.68 (dd, J = 2.71, 1.69 Hz, 2H), 8.45 (s, 2H), 7.81 (q, 31.77, 8.39 Hz, 4H), 7.71 (dd, J = 6.39, 1.68 Hz, 2H), 7.11 (dd, J = 4.39, 3.70 Hz, 2H), 3.68 (s, 4H) ppm.

Analyzed by ^{13}C-APT NMR:

250 MHz, $CDCl_3$ δ = 164.68 (d), 154.74 (s), 150.67 (d), 146.21 (d), 145.74 (d), 136.77 (d), 136.29 (d), 129.55 (s), 128.98 (s), 127.45 (d), 126.58 (d), 123.21 (d), 120.65 (d), 61.67 (t) ppm.

I.E. Conclusion and Outlook

In this chapter a summary of the results will be given.

I.E.1. Synthesis of Eu-Complexes

Three Eu-complexes with bdc, ndc and adc as ligands were successfully synthesized and analyzed by luminescence spectroscopy. The most promising results in relation to this method were obtained by using bdc. Therefore, it is planned to carry out future experiments with this compound as a linker. This could be due to the steric effects of the used ligands. To verify these considerations, further analyses like XRD, etc will be performed. In addition, linear polarized luminescence spectroscopy and measurement of the absolute luminescence quantum yields are also in progress as well, in order to obtain more information about the synthesized complexes.

I.E.2. Development of Thin Films with Helical Eu-Complexes Using Self-Assembling Materials

The cleaning and functionalization of the glass was performed successfully, further analyses such as FT-IR of the samples are in progress already. As a next step an appropriate procedure to connect the Eu-complex onto the prepared surface will be performed. The aim is to achieve layers of polymeric chain-structured complexes by an alternating use of complex and a linker. As mentioned above and in the previous work of M. Hasegawa [12] bdc will be most promising as a linker. In this manner, it is hopefully possible to achieve thick layers with promising photo luminescence properties. These properties can be again analyzed by luminescence spectroscopy, etc as mentioned above.
Also the usage of other lanthanides like Terbium, Neodymium, etc. or different ligands and the combination of several different elements would be of great interest. [12]

I.E.3. Synthesis of N,N^{I}-(Ethane-1,2-diyl)-bis(1,10-phenanthroline-2-yl)methanimin

The synthesis of the target molecule succeeded and resulted in a sufficient yield for analysis and possible further coordination experiments. It was analyzed by ^{1}H and ^{13}C NMR and in this manner its structure was confirmed. Further improvements of the individual reaction steps, as well as purification procedures, are planned.
Usage of the synthesized compound in coordination reactions especially in regards to [12] as ligand to achieve helical poylmeric chain-structured complexes would be of great interest.

I.F. Appendix

The NMR spectra of the synthesized compounds are given below (figure to figure):

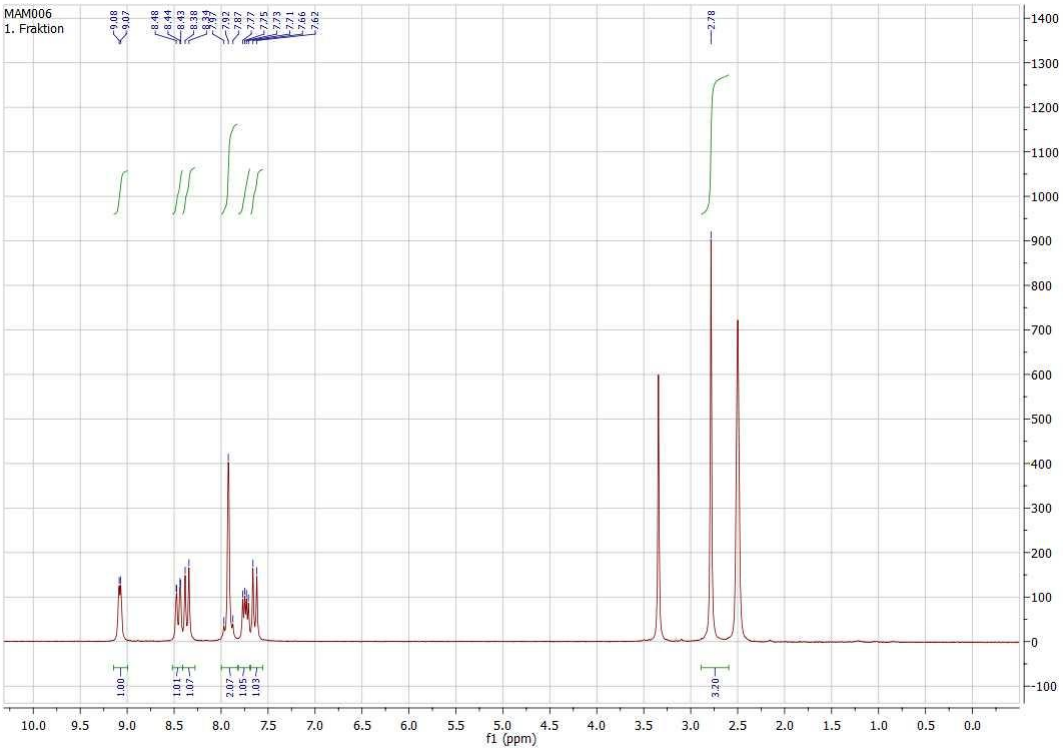

Figure I.F.1: ^{1}H NMR of 2-Methyl-1,10-phenanthroline in DMSO d_6

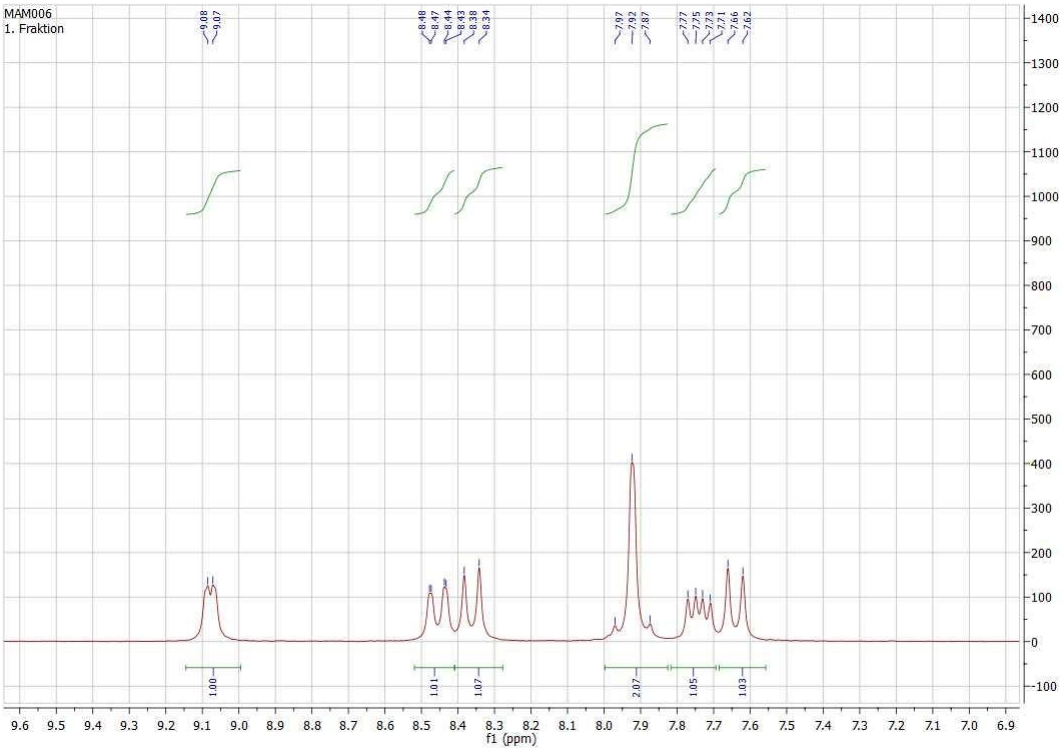

Figure I.F.2: ^{1}H NMR of 2-Methyl-1,10-phenanthroline in DMSO d_6 (aromatic area zoomed in)

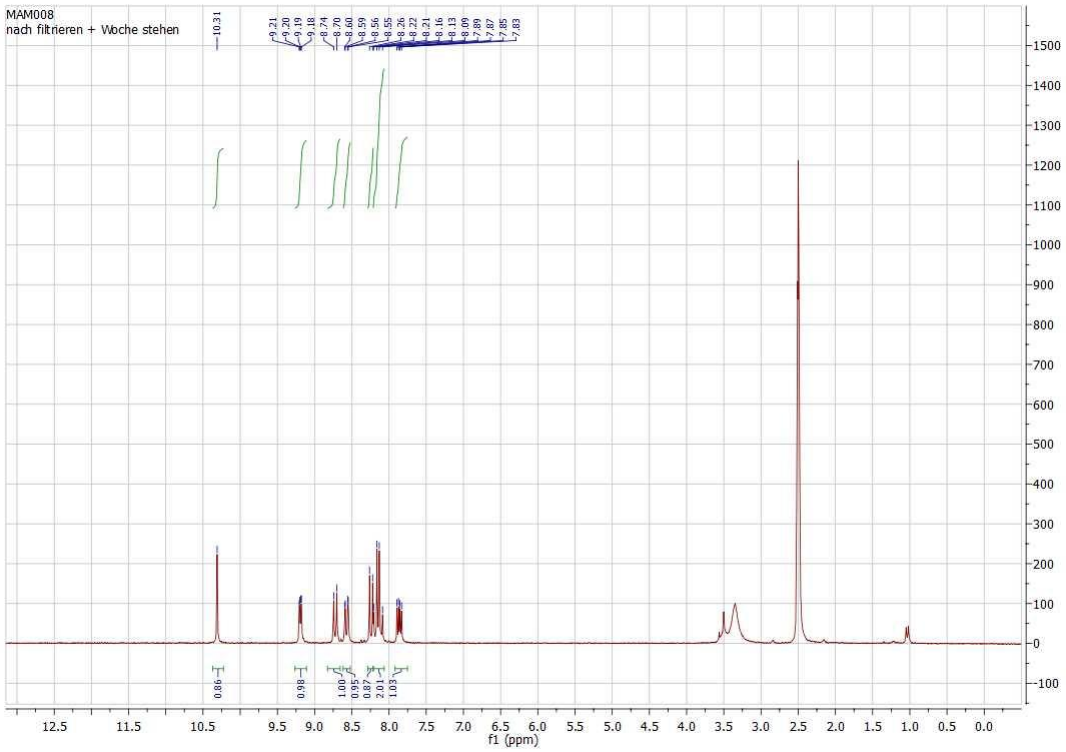

Figure I.F.3: ^{1}H NMR of 1,10-Phenanthroline-2-carbaldehyde in DMSO d_6

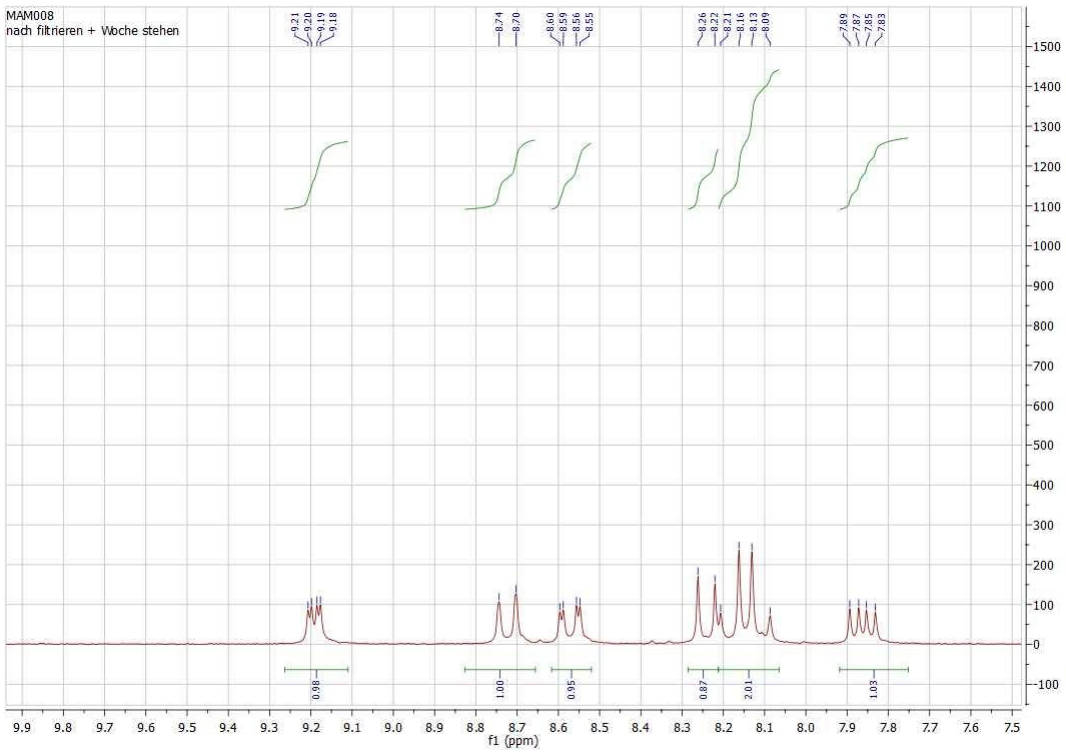

Figure I.F.4: ^{1}H NMR of 1,10-Phenanthroline-2-carbaldehyde in DMSO d_6 (aromatic area zoomed in)

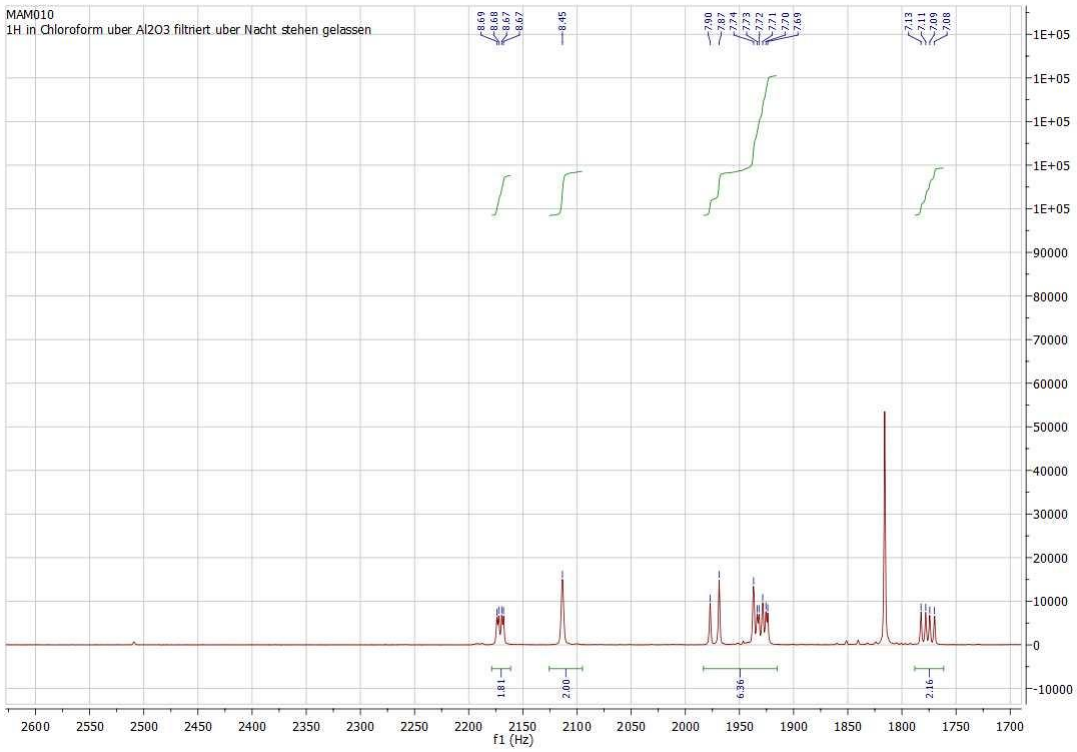

Figure I.F.5: ^{1}H NMR of N,N^{I}-(Ethane-1,2-diyl)-bis(1,10-phenanthroline-2-yl)methanimin in $CDCl_3$

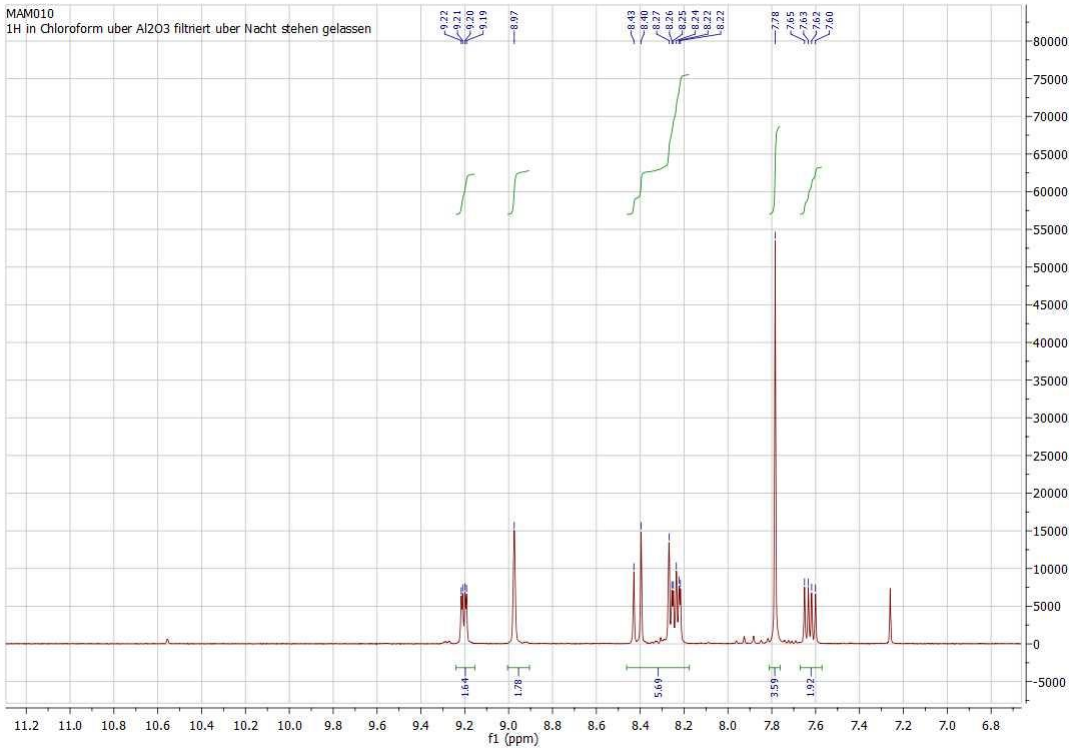

Figure I.F.6: ^{1}H NMR of N,N^{I}-(Ethane-1,2-diyl)-bis(1,10-phenanthroline-2-yl)methanimin in $CDCl_3$ (aromatic area zoomed in)

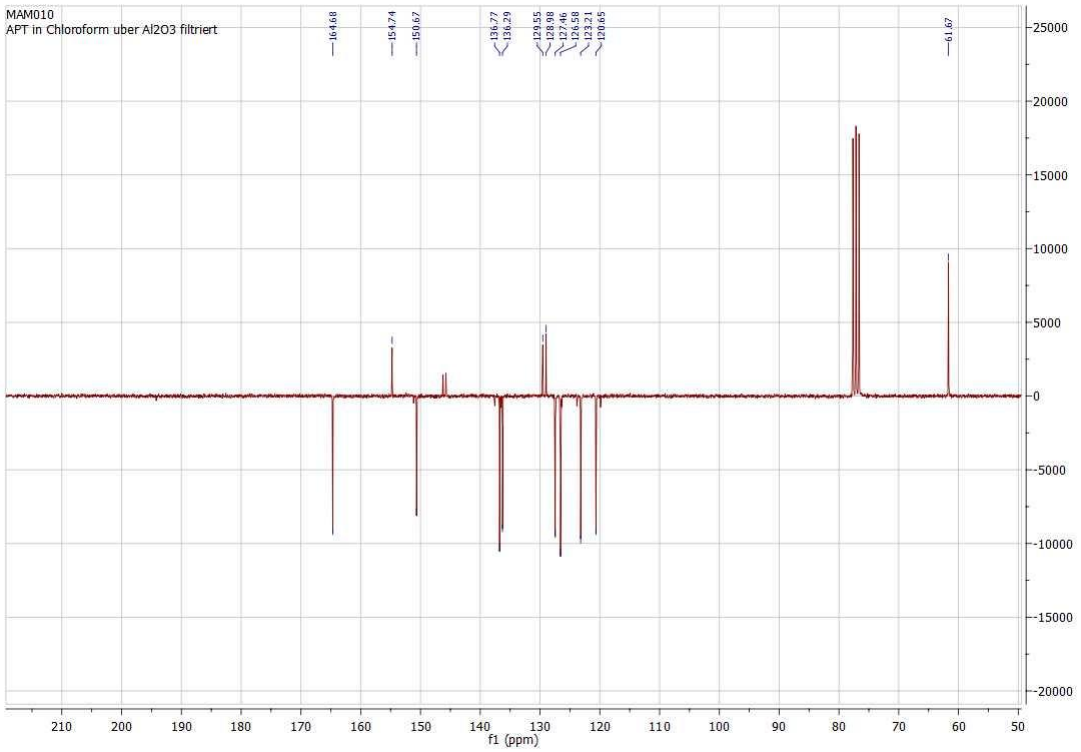

Figure I.F.7: ^{13}C NMR (APT) of N,N^{I}-(Ethane-1,2-diyl)-bis(1,10-phenanthroline-2-yl)methanimin in $CDCl_3$

II. Part:

Synthesis of Copper(I)sulfide

II.A. General Aspects

II.A.1. Introduction

The aim of this thesis was to produce $Cu_{2-x}S$ (with x in the range of -0.2 to 0.2) compounds in various molar ratio and to analyze them regarding to their applicability as thermoelectric materials. Suitable thermoelectric materials are characterized by their possibility to convert temperature differences between two conductors into electricity based on the principle of the Seebeck effect and vice versa to convert electric current in temperature difference due to the so called Peltier effect.[24] [25]

Both of these effects find widespread applications in research and industry. Thermoelectric materials are especially used in cooling systems, a field in the economy where it is important to achieve the best as possible result. In addition the usage of these effects is considerably more environment-friendly than conventional methods. Examples of such outdated methods are refrigeration systems. These machines use mainly toxic materials as refrigerants for the cooling process, which are dangerous for the environment in terms of production, disposal and greenhouse effect. Thermoelectric materials based on the Seebeck and Peltier effects do not require such toxic substances, thus are ideally suited as alternative. Not only is it possible to use this thermoelectric energy conversion for large industrial facilities, but also for a wide range of applications, since these effects are principally scale independent. It is therefore also possible to use thermoelectric materials for small objects like lamps with near the same efficiency. These materials can be built from large bulk modules to very thin films. [26] [27] [28]

Another example is a thermoelectric generator (TEG). Here the waste heat of a technical process is used for the conversion into electricity. This process could be of interest in the automobile industry as cars with combustion engines loose very much energy in terms of unused heat. The further support of TEG could lower the yearly increase of global warming for example through CO_2 savings. So in a nutshell, thermoelectric applications are a very attractive, clean alternative for traditional, declining energy resources like oil, gas, etc. [29]

Nowadays these depicted thermoelectric devices unfortunately achieve not yet adequate energy conversion efficiency for common industrial use. That is why this research area is of great interest and still offers many opportunities. The aim therefore is to find and explore new materials, which are able to fulfill the needed industrial standards to generate the appropriate energy efficiency. To describe this efficiency a figure of merit is used with a dimensionless ZT-value, see equation II.A.1. [30]

(II.A.1) $$ZT = \left(\frac{S^2 \sigma T}{\lambda}\right)$$

Whereby T is the measuring temperature, λ the thermal conductivity, σ the electric conductivity (with $\sigma = \frac{1}{\rho}$, ρ the electric resistivity) and S the Seebeck coefficient.

To achieve satisfying energy efficiencies, a large ZT-value is needed and therefore the focus rests on materials with a high Seebeck coefficient and a moderate electrical conductivity together with a low thermal conductivity. The problem is to optimize just one property without ruining the other, since they are interdependent, meaning it is impossible to change a value without changing the others. A compromise must be reached, keeping in mind that industry standards are favoring a ZT-value larger than 1. [26]

So a way to achieve this goal is to explore on new, unusual materials like Copper(I)sulfide. One advantage of these materials is that the used elements are relatively cheap, easily accessible and less toxic than other metal compounds. Furthermore, copper and especially sulfur form many crystal structures, depending on their molar ratio and sample preparation. Regarding to the crystal structure different outcomes regarding to the ZT-value can be expected. Thus, the potential of these compounds is very high, which has been effectively proved by Zhao and Snyder in their paper *High thermoelectric and mechanical performance in highly dense $Cu_{2-x}S$ bulks prepared by a melt-solidification technique*. [24] Therefore these encouraging achievements were taken up for this master thesis. Further aspects of this compound can be found in section *II.A.4. Copper(I)sulfide* (page 57).

II.A.2. Theoretical Background

In the following the most important theoretical aspects especially regarding to thermoelectric materials with a focus on the Seebeck effect are explained and discussed.

II.A.2.1. Carrier Concentration

As mentioned above the efficiency of a thermoelectric material is characterized by a figure of merit with a dimensionless ZT-value, whose parameters are connected by interdependence. This means every alteration of a value implies a simultaneous change of the others. Whilst increasing, for example, the charge carrier concentration the Seebeck coefficient simultaneously decreases; however the electric and thermal conductivity also increase due their direct proportionality. In conclusion, materials like metals with a very high carrier concentration show a very promising electric conductivity, but unfortunately as a consequence a kind of disappointing small Seebeck coefficient. The plain opposite of that are insulators with a nonexistent electric conductivity. These materials show a ZT-value around zero and are for obvious reasons unsuitable as thermoelectrica. As a result of these considerations, especially narrow gap semiconductors are left for further research. [30] [31]

So the interdependence for the ZT-values is determined by a range of parameters, mainly which carrier type is in place and concentration thereof. Generally, the Seebeck coefficient increases, if the thermoelectric material is composed of an n- or p-type semiconductor. N-type semiconductors have a negative, p-type a positive Seebeck coefficient. [25]

Referring to figure II.A.1, the relation between the ZT-value and the carrier concentration is shown.

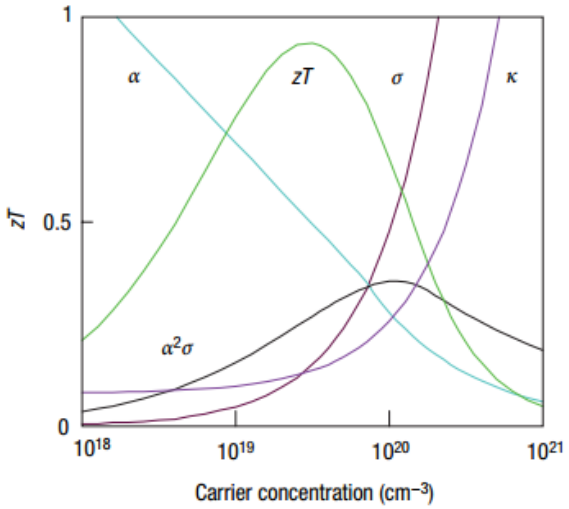

Figure II.A.1: ZT-value depending on the carrier concentration [cm^{-3}], with
α - Seebeck coefficient, σ - electrical conductivity, κ - thermal conductivity [30]

As one can see from figure A.1 the Seebeck coefficient α is falling continuously on a rise of the carrier concentration, whereas the electrical conductivity σ and thermal conductivity κ increase. On the left side of the diagram isolators can be found, going to the right side metals regarding σ and κ. It is particularly interesting to note that the highest peak for ZT is located in the middle of this illustration, between a carrier concentration of 10^{19} and 10^{20} per cm^{-3}. In this range are semiconductors with their narrow band gap located. Thus semiconductors seem to be the best choice for thermoelectric materials, since the ZT-value shows its maximum at this point. It should be mentioned however, that the ratios in the diagram are idealized and perfect semiconductors are assumed. Usually materials and compounds do not present such integrity or other carrier concentration variations may be found. But nevertheless this means if the achievement is a high ZT-value, materials which resemble semiconductors are preferred and should be taken in particular focus. [30] [31]

II.A.2.2. Electrical Conductivity and Resistivity

As mentioned above when looking at the ZT-value and the aim achieving a high one, the electrical conductivity σ is a very important element. When speaking of the electrical conductivity the electrical resistivity must be attributed, since it is its inverse. [25]

The strength of a constant electric current, which is the velocity and number of particles, is determined by the electrical conductivity, when subjecting an electric voltage U to an electrical conductive material. At the same time by contrast the electrical resistivity characterizes to what extent the electric current is disturbed during the current flow by material properties. Or in other words which electric voltage U is necessary for a certain electricity flow in a conductor, whilst overcoming a certain electric resistivity. Thus it describes the dependence of the electric current on the conductor material. This material constant is a characteristic, intrinsic property and is known as specific electrical resistivity ρ. [25]

II.A.2.2.1. Electric Resistivity relating to Temperature

Considering the electric resistivity in periodic infinite crystals (Bloch theory), it appears that it becomes zero. The reason is that there are no scattering processes or other disturbances in such perfect, hypothetical substances. However, in real crystals the specific electric resistivity is among other things depending on scattering processes within the material, a correlation described by the Matthiessen`s Rule. Generally spoken, this rule states that the specific electric resistivity for all independent scattering processes can be totaled up by adding together the specific electric resistivity for all single scattering processes. In relation to temperature there are two temperature-dependent scattering terms, scattering of electrons on lattice vibrations (phonons, ρ_{ph}) and scattering of electrons against each other (ρ_{ee}), and a temperature-independent term, resulting of electron scattering on lattice imperfections (ρ_0). Hence at zero temperature (T = 0 K) the resistivity is only dependent on impurities and defects. The terms of the Matthiessen`s Rule are displayed in equation II.A.2: [25] [32] [33]

(II.A.2) $$\rho = \rho_0 + \rho_{ph}(T) + \rho_{ee}(T) + \dots$$

At room temperature the specific electric resistivity is mainly caused by interactions of electrons with phonons in the lattice structure of the metal/material. However at temperatures next to absolute zero, scattering with foreign atoms (impurities or doping) and mechanical lattice effects must be considerate. It can be concluded that this empirical rule should be seen approximately and not general assumable. [25] [32] [33]

At room temperatures for metals the amount of scattering caused by phonons dominates. This phenomenon is generally defined by the Bloch-Grüneisen law and it is illustrated in the figure II.A.2:

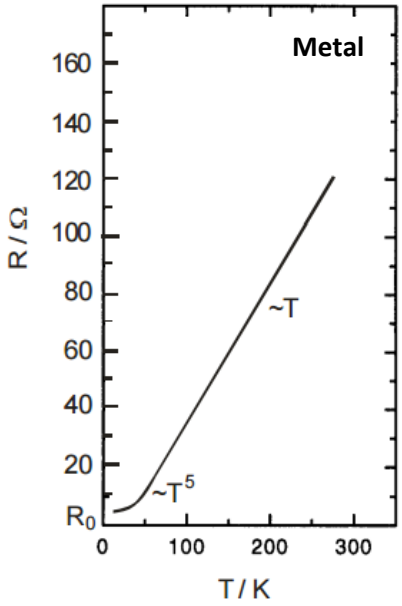

Figure II.A.2: Electrical Resistance R [Ω] plotted against temperature T [K] of copper [34]

As suggested by figure II.A.2 the electrical resistance in common metals increases with the temperature. It is proportional to T^5 [K] at very low temperatures, at higher temperatures it increases constantly with T. However the case is different for semiconductors, as seen in figure II.A.3:

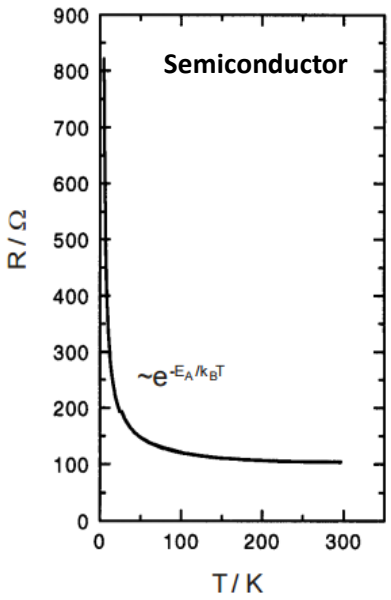

Figure II.A.3: Electric resistivity R [Ω] plotted against temperature T [K] of carbon [34]

Here the specific electric resistivity decreases with rising temperatures, at T = 0 K it is several orders of magnitude higher than those for metals. The cause lies in the special characteristics of the semiconductor itself, namely the band gap between conduction and valence band. Charge carriers are not able to overcome this band gap at such low temperatures. It should be noted that the shape of the curves in figure II.2.A and II.3.A can but does not necessarily look like this. Also way more complex models (two- and three- band model) are used to describe more advanced problems. [33]

II.A.2.2.2. Electric Resistivity relating to Concentration

The specific electrical resistivity ρ also depends on the carrier concentration. As described under point *II.A.2.1. Carrier concentration* (page 46) the electrical conductivity σ increases with a higher carrier concentration. By implication that means that the specific electrical resistivity drops in accordance, being the inverse to the electrical conductivity. Appropriate doping should therefore result in a decrease of the specific electrical resistivity. [33]

II.A.2.3. Thermal conductivity

The thermal conductivity λ describes in simple terms how well a material conducts heat. If a temperature difference is applied on a sample (metal, etc.), the thermal conductivity determines the ability to carry heat from the hot to the cold end of the sample. Therefore it is a very important property of every material and is generally described by the Fourier´s law for heat conduction with the temperature T and the local heat flux density $\vec{q}$ (equation II.A.3):

(II.A.3) $$\vec{q} = -\lambda\vec{\nabla}T$$

The thermal conductivity in solids depends on the following factors: Temperature, carrier concentration and disorder within the material. Heat (= energy) is mainly transported via (quasi-) particles like electrons (el) and phonons (ph), these contributions can be summed up to calculate the total thermal conductivity. For this purpose following equation is used (equation II.A.4):

(II.A.4) $$\lambda = \lambda_{el} + \lambda_{ph} + \ldots$$

When comparing different materials, it appears that the thermal conductivity of metals is mainly caused by charge carrier like electrons (λ_{el}), whereas in case of isolators phonons (λ_{ph}) outweigh. Reason for this is that in isolators hardly any charge carriers are present. As for semiconductors both terms should be considered together. [33] [35]

Additionally, the electronic thermal resistivity W_{el} should be mentioned at this point. W_{el} is the inverse to λ_{el}, which is as described above the partial amount caused by electrons to the thermal conductivity λ. It is defined by equation II.A.5:

(II.A.5) $$\frac{1}{\lambda_{el}} = W_{el} = W_{el,0} + W_{el,ph}$$

The two terms in equation A.5 describe the different scattering process of electrons within the material. $W_{el,0}$ deals with the scattering of electrons on lattice defects; this term exists at 0 K. $W_{el,ph}$ expresses the scattering of electrons on phonons; this term vanishes at 0 K and is consequently temperature dependent. [33] [35]

II.A.2.3.1. Thermal conductivity relating to Temperature

It is necessary to discuss the above mentioned terms individually with regard to temperature. For the relation between the charge carrier amount of the thermal conductivity (λ_{el}) and the electrical conductivity σ the empirical Wiedemann-Franz law (improved by the Drude-Sommerfeld theory) is applied (equation II.A.6):

(II.A.6) $$\left(\frac{\lambda_{el}}{\sigma T}\right) = \left(\frac{\pi^2}{3}\right)\left(\left(\frac{k_B}{e}\right)^2\right) = LT = 2{,}45 * 10^{-8}\left(\frac{W\Omega}{K^2}\right)$$

e… Elementary charge k_B… Boltzmann constant L… Lorenz number

The other term concerning the effect caused by phonons can be explained by the kinetic gas theory (equation II.A.7):

(II.A.7) $$\lambda_{ph}(T) = \frac{1}{3} C_v(T) v^2 \tau(T)$$

C_v… Specific heat capacity for a constant volume v… Velocity τ… Mean free time between collisions

To draw a solution from equation A.7, C_v and τ must be considered more closely:
The specific heat capacity C_v [JK^{-1}] is temperature-dependent. In order to calculate it, the Debye model is used. This model has been introduced to represent the contribution of phonons to the specific heat capacity and as further consequence to the thermal conductivity. The specific heat capacity in the Debye model at high temperatures is equal to the so called Dulong Petit ratio with T_D as Debye-temperature and N_A as Avogadro constant (equation II.A.8). However at low temperatures $C_v(T < T_D)$ increases with T^3. [25] [36]

(II.A.8) $$C_v(T > T_D) = 3\, k_B N_A$$

The other term τ is the mean free time between collisions of electrons in a material (= relaxation time). It describes the average time between collisions and is also temperature-dependent. τ (T) remains constant at very low temperatures. Speaking of the mean free time, the mean free path should also be mentioned. It describes the average path length each particle (atoms, molecules, ions, electrons, etc.) covers without a collision with another. If the temperature is lowered the mean free path increases up to a certain point until it becomes constant. At this point only defects and the samples dimension play a role. [25] [36]

These considerations summarized, it is possible to draw a conclusion for the temperature dependence of the thermal conductivity λ(T). At very low temperatures λ(T) depends on $C_v(T < T_D) \approx T^3$ and the other terms keep constant, at very high temperatures it depends on $\tau(T) \approx \frac{1}{T}$. This holds in general for isolators, the behavior is shown in following figure II.A.4: [25] [37]

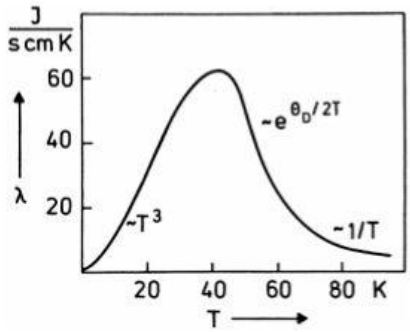

Figure II.A.4: Thermal conductivity [$Js^{-1}cm^{-1}K^{-1}$] plotted against temperature against temperature [K] [37]

With regard to the area around 40 K in figure A.4, where the thermal conductivity is increasing till the decay. To explain this observation one should keep in mind, that at lower temperature (here below 40 K) the total momentum remains unchanged (only Normal processes). At higher temperatures particles (phonons) exist with a large enough momentum to perform so called Umklapp scattering, which leads to the exponential decay of the thermal conductivity. [25] [37]

II.A.2.3.2. Thermal conductivity relating to Concentration

In a similar manner to the electrical conductivity the thermal conductivity increase with the carrier concentration, see figure x1 (λ = κ abbreviation for thermal conductivity). As mentioned above under paragraph *II.A.2.2.2. Electric Resistivity relating to Concentration* (page 50) doping should lower the specific electrical resistance. [25] [37]

II.A.2.4. Seebeck Effect

The Seebeck effect occurs when a temperature difference is applied on two connected, diiferent materials and a heat transport between the contact points of these takes place. As a result of this, charge carriers move automatically from the hot side to the cold one and that way an electric voltage is produced. This is due to the so called thermodiffusion. To describe this phenomenon, the Seebeck coefficient S is used. If electrons (or holes) are thermally promoted across gaps, the number of charge carriers increases, thus S increases. It represents the proportionality factor between the applied temperature gradient $\vec{\Delta}T$ and the subsequent electric field $\vec{E}$ (equation II.9): [25]

(II.A.9) $$\vec{\mathrm{E}} = \mathrm{S}\vec{\nabla}\mathrm{T}$$

Equation II.10 shows the relationship between the Seebeck coefficient S, the voltage U and the temperature difference ΔT:

(II.A.10) $$\mathrm{S} = (-\frac{\mathrm{U}}{\Delta\mathrm{T}}) \Rightarrow \mathrm{U} = (\mathrm{S_A} - \mathrm{S_B})\Delta\mathrm{T}$$

By using this equation, the voltage U in an electric circuit caused by the Seebeck effect can be measured. As mentioned above, for this purpose a temperature gradient ΔT is applied on the contact points of two metals with different Seebeck coefficients (S_A and S_B). [25]

A simplified presentation of this circuit can be seen in figure II.A.5:

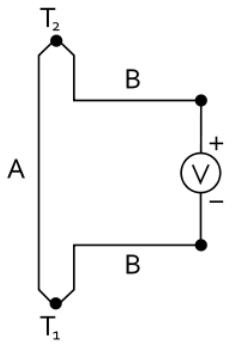

Figure II.A.5: Simplified electric circuit for measuring the voltage V caused by the Seebeck effect [38]

The comparison between metals and semiconductors regarding to the Seebeck effect shows that metals have a smaller one. Reason therefore is that both electrons and hole are transported in metals and these effects cancel each other out. Doped materials like semiconductors show a higher Seebeck coefficient, a negative for n-type doped semiconductors, a positive for p-type. The aim is to achieve a high as possible resulting voltage U, therefore materials with completely different (= positive and negative sign) Seebeck coefficients are used, in this case for example a combination of metals with opposite signs of the Seebeck coefficient. [25]

II.A.3. X-Ray Diffraction

The X-ray diffraction is a simple, straight-forward method, to analyze the crystal structure of the thermal treated samples. In this way it is possible to draw a conclusion about the chemical structure of the prepared materials. Bragg's law is the basis for this measurement, described in equation II.A.11, with the distance between two parallel lattice planes (=d), the scattering angle between the X-ray beam and lattice plane (= sinθ), a positive integer (= n) and the wavelength of the X-ray beam (= λ): [35]

(II.A.11) $$2d\sin\theta = n\lambda$$

Briefly explained when an X-ray beam hits a crystal structure, most of the rays move unhindered through. But a very small percentage is distracted by the atoms of the crystal, an effect called X-ray diffraction. This phenomenon occurs when an X-ray beam with an appropriate wavelength λ hits the lattice plane with the correct angle θ. The lattice planes have to be parallel and must stand in the right distance d.

Only after the fulfillment of these conditions, described in Bragg's law, constructive interferences of spherical waves can come up, which superimpose and enhance themselves. These spherical waves are caused by the diffraction of the X-ray beams on the electron shells. If one looks at the system macroscopically, it gives the impression that the X-ray beam is reflected at the crystal structure. [35]

A visual representation of Bragg's law can be found in figure II.A.7:

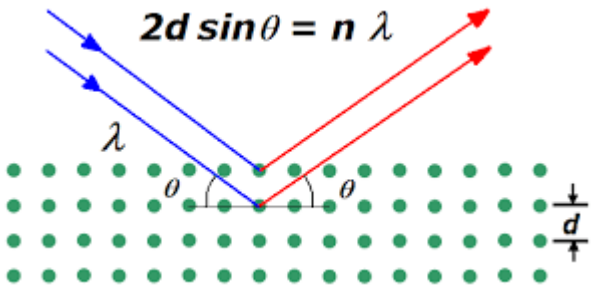

Figure II.A.7: Visual Representation of Bragg's law [39]

II.A.4. Coppersulfide

In this chapter the target substance copper(I)sulfide and its source elements copper and sulfur are further discussed.

II.A.4.1. Copper

Copper (Cu) belongs to group 11 of the periodic table, together with silver as well as gold. It is a typical metal and name giver of this group. Elements that belong to this group have the electron configuration (n-1) d^{10} ns^1, therefore they can exist in various oxidation states beginning from +1 to +4/+5. The precious metal behavior, which is characteristic for this group, is caused amongst other things by relativistic effects. Metals of group 11 exhibit high melting points (Cu: 1085 °C) and they crystallize cubic face centered. Generally, Cu is a bright red metal with tough and flexible properties, making it interesting for processing. One of the most important advantages is its excellent electric and thermal conductivity. Only silver conducts better. This characteristic is an important aspect regarding to thermoelectrica as one can see in this thesis. [1]

The most important oxidation states for copper are +1 and +2. It can form chemical bonds with oxides, hydroxides, sulfides, sulfates, cyanides and halogenides. The stability of oxidation states is defined by their redox potential: $Cu \xrightarrow{+0.52\ V} Cu^{+} \xrightarrow{+0.15\ V} Cu^{2+}$

Cu^+-ions disproportionate in aqueous solutions to Cu and Cu^{2+}-ions (ΔE = + 0.37 V), but this equilibrium depends on the solubility and complexing mechanism of the copper compound. Generally, the +2 oxidation state is the one favored. Copper is common metal, which does not exist as pure element but in sulfide minerals and in oxidized forms like Chalkosin (Cu_2S), Chalopyrit ($CuFeS_2$), etc. In most of the cases the raw material is roasted, slagged and electrolytically purified. Figure II.A.8 shows such a raw material, native copper: [1]

Figure II.A.8: Native copper mineral with impurities from other elements and oxidation processes [40]

Native copper occurs naturally in small quantities. It is used for producing pure elemental copper among other materials. Usually it is contaminated with other elements such as iron and dark stained due to oxidation processes in contrast to the typical copper-like color. [41]

II.A.4.2. Sulfur

Sulfur (S) occupies the position under oxygen amongst with Selen, Strontium and Tellur in group 16 of the periodic table, the so called chalcogens. It has a characteristic yellow color and an unpleasant, irritating smell. As a nonmetal it shows a poor thermal and electric conductivity. However, Sulfur is very reactive and forms chemical bonds with most elements (exceptions are noble gases, gold, platin, iod, etc.) The most common oxidation states for S are +6, +4, +2 and -2. Most of the global sulfur resource is produced from H_2S-based gases with the so called Claus-process. A small amount of elemental S comes from natural reserves. [1]

Sulfur has many various, allotropic modifications at different temperatures and aggregate states. Figure II.A.9 shows the heating up process of Sulfur from room temperature up to 444 °C:

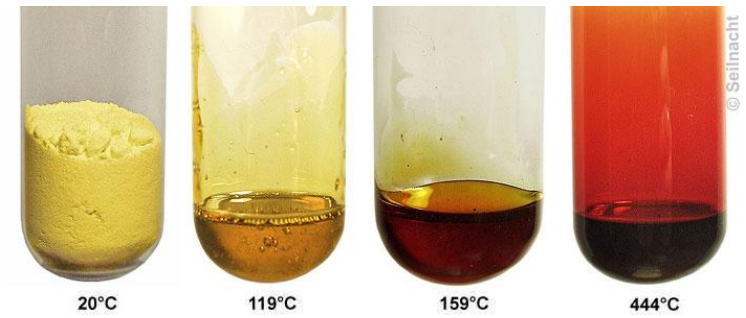

Figure II.A.9: Heating up process of Sulfur and the resulting changing modifications [42]

At standard conditions (in figure II.A.9 outer left, at 20 °C) bright yellow, orthorhombic Sulfur exists. Its crystal form is called α-Sulfur. This is the only thermodynamic stable form under normal conditions. The S atoms form eight-membered, crown-shaped rings (S_8). Heating above 95.6 °C results in a transformation to monoclinic Sulfur, also called β-Sulfur. At this temperature the S_8 atoms try to rearrange in their crystal lattice, but the speed of conversion is still relatively low. When heating up to 119 °C the melting point of Sulfur is reached and the monoclinic β-Sulfur melts to λ-Sulfur (in figure A.9 second from left), a dark yellow liquid with more moveable S_8 rings. Continuing the heating up, the initial S_8 rings change their structure to other rings with various sizes (S_n, with n = 6, 7, 9, 12 up to 26). When S_{26} forms, it is called π-Sulfur. Observing the reaction, it appears that the melt is getting darker whilst staying relatively thin. At 159 °C (in figure A.9 second from right) the viscosity dramatically increases. Polymeric μ-Sulfur forms at this temperature. The viscosity reaches its maximum at 185 °C, after this point it decreases due to thermal cracking processes and the forming of biradical, aliphatic chains starts. At 444.6 °C (in figure A.9 outer right) the boiling point is reached. The melt changes its color to dark red-brown and in the gas phase a temperature-dependent equilibrium between S_n (with n = 1-8) sets in. Above 1800 °C single Sulfur atoms are transferred to the gas phase, at 2200 °C S-atoms predominate. [1] [43]

II.A.4.3. Copper(I)sulfide

Copper(I)sulfide is a black solid with a bluish shimmer with the molecular formula Cu_2S. It occurs in nature as a mineral called chalcocite (Cu_2S, shown in figure II.A.10) and can be produced synthetically with pure copper and sulfur under vacuum and high temperatures. [1]

Figure II.A.10: Mineral Chalcocite ("Kupferglanz") [44]

The crystal structure of this chalcogenide compound is quite complicated:
According to the temperature a cubic (anti-)fluorite structure (over 743 K) or a hexagonal structure (between 743 and 376 K), which is called high chalcocite can be found. At room temperature it forms a crystal structure called low chalcocite. Slightly changing the stoichiometric ratio (from Cu_2S to $Cu_{1.96}S$) results in a new crystal structure, which can be found in the mineral djurleite. So there are various crystal structures, present in this compound. The reaction conditions and molar ratios of the starting elements affect whether copper(I)sulfide or copper(II)sulfide forms, hence these factors should be kept in mind for the experiments. [45]
Recently, copper(I)sulfide distinguish itself by being an interesting compound for high temperature thermoelectrica. Experiments were conducted where hot-pressed $Cu_{2-x}S$ polycrystalline bulks were analyzed regarding to their performance as thermoelectric material. Very promising results were obtained with ZT-values around 1.7 at 1000K. Additionally, the raw materials for the production of copper(I)sulfide, which are pure copper and sulfur, are easily accessible, non toxic and affordable. Enough reasons to further investigate this compound. One method to produce it is by using spark plasma sintering systems. This, however, has the big disadvantage of high costs and harsh reaction conditions (very high pressure and temperature). Therefore, another method is to be sought and found in the work of Zhao and Snyder: *High thermoelectric and mechanical performance in highly dense $Cu_{2-x}S$ bulks prepared by a melt-solidification technique*. [24]

This paper shows a two-step method to receive the target compound, firstly the production of highly dense bulks and afterwards their subsequently thermal treatment (melt-solidification technique). Samples produced in this manner (with a molar ratio of Cu_2S and $Cu_{1.97}S$) show very promising results with ZT-values around 1.9 at 937 K.

In figure II.A.11 the results for the electric conductivity (a), Seebeck coefficient (b), thermal conductivity (c) and ZT-value of the two samples described above are presented: [24]

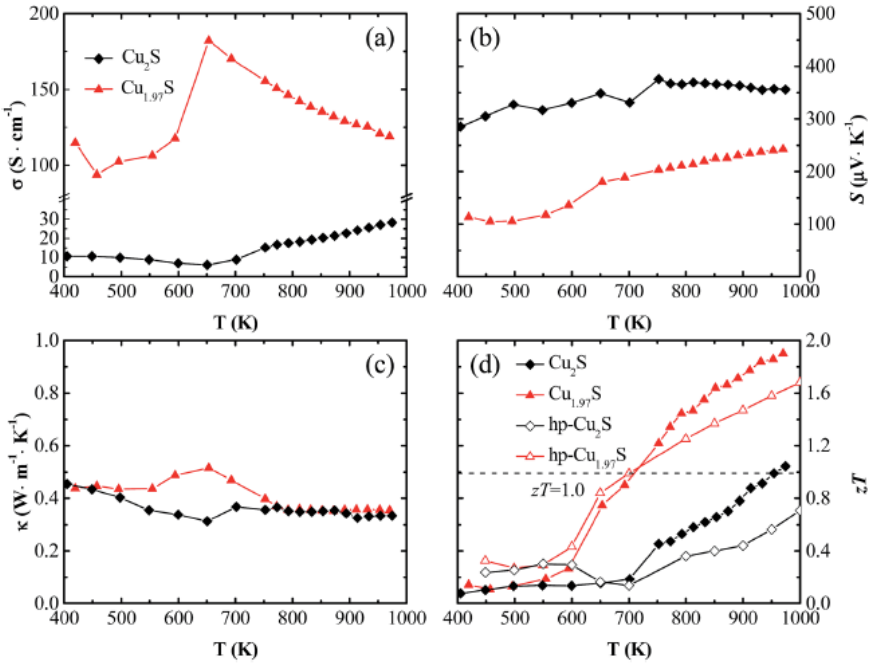

Figure II.A.11: Electric Conductivity (a), Seebeck Coefficient (b), Thermal Conductivity (c) and ZT-value (d) plotted against Temperature (K) for Cu_2S (black) and $Cu_{1.97}S$ (red), hp abbreviation for hot pressed [24]

As one can see there are encouraging results for the individual values. Also differences between Cu_2S and $Cu_{1.97}S$ and some indicated phase transitions for the electric conductivity can be found. The ZT-value seems to depend strongly on the molar ratio and the preparation method (lower right corner). Generally, the method (melt-solidification technique) described in the paper of Zhao and Snyder seems to be ideally suited for producing highly dense copper(I)sulfide bulks in various molar ratios. Considering the high ZT-value and the easy practicability of the sample preparation it was the basis and motivation for this diploma thesis.

In addition it can be said that copper(I)sulfide is a typical representative for Soft/Soft Lewis Acid-Base interaction, since this compound is the result of a reaction between Sulfur and Copper.

II.B. Experimental

II.B.1. Sample Preparation

II.B.1.1. Preliminary Tests

As a first step it was necessary to prepare the samples, by mixing fine copper (MG: 63.546) and sulfur (MG: 32.06) powder (both with a degree of purity of 99.8 % by Merck) together in their selected stoichiometric ratios. Choosing the molar ratio was as mentioned before inspired by previous works of Zhao and Snyder.[24] In their work the experiments were performed with $Cu_{2-x}S$ (x = 0 and 0.03) achieving promising results. Therefore these ratios were adapted, resulting in the following three samples, which were prepared for the further experiments:

Table II.1: Molar Ratios Preliminary Test Samples

Sample Name	Molar Ratio
MK1	Cu_2S
MK2	$Cu_{1.8}S$
MK3	$Cu_{2.2}S$

Table II.1 shows that the molar ratio for MK2 and MK3 were significantly above the suggested ratio by Zhao and Snyder, whereas for MK1 it was maintained.[24] These samples were the first experiments within this chemistry in the working group, so they were used to get general information and to gain a deeper insight.

Every sample was prepared by weighing in the required amount of copper and sulfur. The fine powders of these starting materials were carefully mixed together with a mortar and pestle. The total weight of each sample was 3 g. This was the necessary amount to carry out the following experiments. In table 2 the initial and the actual sample weight can be found:

Table II.2: Sample weights of Cu and S, Preliminary Test Samples

Sample Name	Cu calculated [g]	Cu weighed [g]	S calculated [g]	S weighed [g]
MK1	2.396	2.395-?	0.604	0.601
MK2	2.343	2.336	0.657	0.656
MK3	2.440	2.433	0.560	0.560

As in table II.2 can be seen there were some differences between the calculated and the actual weighed mass of the starting materials. This can be put down to difficulties during the weighing process, each element was put separately in a small shovel before being transferred into a mortar. Both elements were used as a fine powder and especially the copper powder was difficult to transfer due to electrostatic charge, resulting in the above seen distinctions.

Unfortunately the weight of sample taken for MK1 was not written down, therefore it was not possible to calculate the actual molar ratio. For the other two samples MK2 and MK3 the actual molar ratios are found in table II.3:

Table II.3: Calculated and Actual Molar Ratios, Preliminary Test Samples

Sample Name	Calculated Molar Ratio	Actual Molar Ratio
MK1	Cu_2S	?
MK2	$Cu_{1.8}S$	$Cu_{1.8}S$
MK3	$Cu_{2.2}S$	$Cu_{2.2}S$

As seen in table II.3 there were no significant differences between the calculated and the actual molar ratios for sample MK2 and MK3, only the actual molar ratio for MK1 could not be figured out due to absent reference values. It did not matter too much at this point, because these experiments were an initial attempt to broadly understand this kind of chemistry. Therefore it was decided to continue the experiments with sample MK1.

After blending the yellow sulfur and reddish copper powder to a yellowish light brown mixture, it could be observed that after a while the color of the samples turned to a darker brown. This behavior could be lead back to oxidation processes during the preparation. Both elements were used as fine powders, resulting in a very large surface area. So during the mixing process a reaction with the atmospheric oxygen could have taken place. Another explanation could be that by using mortar and pestle to blend the starting materials, friction caused resulting heat, which could lead to a starting reaction between copper und sulfur. In this way probably not the desired Cu_2(I)S but instead Cu(II)S had formed. This should not be a problem because the samples were later heated up over 507 °C in vacuum. During this process following decomposing should take place: 2 CuS -> Cu_2S + S
It must be kept in mind that the so formed copper(I)sulfide is not completely stoichiometric and rather described by the molecular formula $Cu_{2-x}S$. [46]
Considering the above mentioned aspects, it was reasoned to free the fine copper from possible oxygen contaminations (materials with a large surface area like powders are prone to react with the atmospheric oxygen). Therefore the copper powder was washed with an aqueous ammonia solution, but the results were not promising as a consequence of this treatment, the copper complex $[Cu(NH_3)_4]^{2+}$ formed. This method was abstained.

After preparing the samples in the manner as stated above, the starting materials were pressed into cylindrical pellets with a hydraulic press (OMCN, ART.-156, Tonn. 20) at a pressure of 50 bar for about one minute. The highly dense pressed bulks have a silver metallic color and thus vary in terms of color from the unpressed yellow-brownish powdery samples.

Overlapping edges were straightened with a scalpel. The resulting probe diameter and height of the samples were around 8.5 to 8.54 mm and 11 to 12.10 mm. The differences in height can be explained by a varied pressing time.

II.B.1.2. Charge I and Charge II

After the promising preliminary tests the experiments were continued, this time with a slightly substoichiometric molar ratio in comparison with Cu_2S. The intended molar ratios are presented in table II.4:

Table II.4: Molar Ratios, Charge I

Sample Name	Molar Ratio
MK4	$Cu_{1.98}S$
MK5	$Cu_{1.96}S$
MK6	$Cu_{1.94}S$
MK7	$Cu_{1.92}S$

The samples of charge I (MK4, MK5, MK6 and MK7) were prepared in the same manner as the ones of the preliminary tests. But in contrast the fine copper und sulfur powders were weighed directly in a mortar to avoid losses due to the transfer. The starting materials were carefully mixed together with a pestle. Each sample weighed 4 g in total, containing the appropriate amount of copper and sulfur. In table II.5 the calculated and the actual sample weights of the starting materials can be found:

Table II.5: Sample weights of Cu and S, Charge I

Sample Name	Cu calculated [g]	Cu weighed [g]	S calculated [g]	S weighed [g]
MK4	3.188	3.188	0.812	0.812
MK5	3.181	3.181	0.819	0.819
MK6	3.174	3.174	0.826	0.826
MK7	3.168	3.168	0.832	0.832

With the weights of sample taken the actual molar ratios could be figured out and compared to the calculated ones. In table II.6 the results can be found:

Table II.6: Calculated and Actual Molar Ratios, Charge I

Sample Name	Calculated Molar Ratio	Actual Molar Ratio
MK4	$Cu_{1.98}S$	$Cu_{1.98}S$
MK5	$Cu_{1.96}S$	$Cu_{1.96}S$
MK6	$Cu_{1.94}S$	$Cu_{1.94}S$
MK7	$Cu_{1.92}S$	$Cu_{1.92}S$

Table II.6 shows that there are no significant differences between the calculated and the actual molar ratios, meaning that the new used weighing method is better suitable. As with the samples of the preliminary tests, the ones of charge I also changed their color from a yellowish light brown (due to the color of the starting materials) to a much darker brown over a short period of time. The samples were stored for a few days, as a result the color transferred to a very dark, nearly black shade.

Since this behavior appeared while preparing the samples of the preliminary test as well as the samples of charge I, it was considered that the starting materials either had reacted during mixture process already with each other, or with atmospheric oxygen or both reactions occurred simultaneously. To avoid unwanted reactions with oxygen, it was therefore decided to work under inert conditions. A glove box was used for this purpose. To prepare sample MK8 (with a molar ratio of $Cu_{1.96}S$, same as MK5), copper and sulfur were separately weighed in air and transferred to the glove box. Under these inert conditions both starting materials were finally mixed in a mortar and blended with a pestle. However the usage of low friction already caused a strong exothermic reaction between copper and sulfur. This was reflected by the emergence of dark fume and heat release. Black powder with a bluish shimmer formed, which indicates the formation of copper(I)sulfide. The reaction was immediately stopped by getting the reaction vessel out of the glove box and pouring water over it. The remaining powder residues were dried and analyzed by X-ray diffraction, the results of the measurement were not very revealing.

One likely explanation for this unexpected strong reaction could be the actually intended exclusion of oxygen. Under normal conditions atmospheric oxygen forms a very thin, protecting layer during the reaction, something that cannot happen in the glove box. In combination with the friction heat caused by the pestle, there was more than enough energy to abruptly start the reaction between sulfur und copper.
Nevertheless the idea to prepare the samples under inert conditions was continued. Consideration was given to the friction problem caused by the pestle, therefore a solution was sought to avoid this problem. It was decided to try to homogenize the starting materials with a bird feather. In order to try this attempt sample MK9 (1 g, molar ratio $Cu_{1.98}S$) was prepared. For this purpose copper and sulfur powder were again weighed individually and transferred to the glove box. This time the elements were mixed with the feather, to avoid friction. This method worked very well and unwanted early reactions did not happen. Afterwards the test tube containing the mixture was sealed with a balloon and taken out of the glove box. In this way the inert conditions were kept inside the vessel and the starting materials were reacted directly with a Bunsen burner. So possible rising pressure could be absorbed by the balloon.

The sample reacted immediately under these circumstances and a black solid with a bluish shimmer formed. Some sulfur evaporated at the head of the test tube. By using this method it was possible to produce samples and let them react under inert conditions. The possible difference of samples prepared under normal or inert conditions was of great interest. Therefore it was decided to prepare charge II again with four samples (MK10, MK11, MK12 and MK13), which resembles the molar ratios of charge I (see table II.7):

Table II.7: Molar Ratios, Charge II

Sample Name	Molar Ratio
MK10	$Cu_{1.98}S$
MK11	$Cu_{1.96}S$
MK12	$Cu_{1.94}S$
MK13	$Cu_{1.92}S$

The samples of charge II were prepared in the same manner as MK9 (weighing in the air, homogenization and reaction under inert conditions). This time the total weight of each sample was 5 g. In the following table II.8 the calculated and actual weights of the samples can be found:

Table II.8: Sample weights of Cu and S, Charge II

Sample Name	Cu calculated [g]	Cu weighed [g]	S calculated [g]	S weighed [g]
MK10	3.985	3.963	1.015	1.001
MK11	3.976	3.923	1.024	1.014
MK12	3.968	3.865	1.032	1.027
MK13	3.959	3.832	1.040	1.033

Table II.8 shows that there are some differences between the calculated and weighed amount of the starting materials. This is explained by the more complicate work conditions in the glove box. In addition the copper and sulfur powder were weighed separately and mixed transferred in the test tube. Thus residues remained in the original vessel, which could not be avoided despite all affords. In table II.9 the calculated and actual molar ratios are represented:

Table II.9: Calculated and Actual Molar Ratios, Charge II

Sample Name	Calculated Molar Ratio	Actual Molar Ratio
MK10	$Cu_{1.98}S$	$Cu_{1.99}S$
MK11	$Cu_{1.96}S$	$Cu_{1.98}S$
MK12	$Cu_{1.94}S$	$Cu_{1.95}S$
MK13	$Cu_{1.92}S$	$Cu_{1.93}S$

After the samples of charge II were finished the pellets for the thermal treatment were produced. The samples of charge I were already in powder form, the ones of charge II were prior to pressing carefully grinded, since they had formed a porous solid during the pre-reaction.

For charge I and II the same parameters were used to produce cylindrical pellets (see point *II.B.1.1.Preliminary Tests*, (page 59). However, under these conditions the samples did not solidify. This behavior differed significantly from the preliminary tests. Therefore the pressure was increased to 200 bar, but the sample still remained mainly a fine powder and only formed a very thin solid layer. Only when the pressing time was increased to five minutes, it was possible to produce solid cylindrical pellets. After pressing the overlapping edges of the samples were straightened with a scalpel. In this way eight silver metallic samples were prepared for the melt-solidification process. No differences between charge I and II could be determined due to color or pressure behavior. The resulting probe diameter and height of the samples were around 7.07 to 9.89 mm and 10.19 to 10.27 mm.

II.B.2. Thermal Treatment

II.B.2.1. Preliminary Tests

The pellets were each sealed in quartz tubes and evacuated at $6.4*10^{-5}$ mbar (with a Pfeiffer Balzers DUO 016 B) for three hours at room temperature. It was necessary to carry out the thermal treatment free from air, to avoid unwanted reactions with atmospheric oxygen while heating up the samples. At first the pellets were heated up in a furnace (Nabertherm P 330) to 400 °C with a heating rate of 300 °C per hour (correspond to 5 °C per minute), this temperature plateau was held for 5 hours. Then it was heated up to 1150 °C again with a heating rate of 300 °C per hour. After two hours at this temperature, the furnace was allowed to cool down to room temperature. Overall the thermal treatment took over 18 hours. [24] Afterwards the samples were removed from the oven and examined. It could be seen that the previous cylindrical pellets lost their original form during the heating process and melted a bit away. The pellets kept their metallic color, sample MK2 appeared to have a darker shade and gave a crystal-like impression. It seemed that sample MK3 had reacted with the quartz tube wall. MK1 showed no abnormalities. In general, all of the tubes appeared to be clear, no sulfur was sublimated. After opening the tubes with a hammer a slight sulfurous odor came up.

II.B.2.2. Charge I and Charge II

The samples of charge I and II were also each sealed in quartz tubes as well as evacuated and treated with the same thermal treatment, as described in section *II.B.2.1.Preliminary Tests* (page 64).

However, after the heating process it turned out that two of the quartz tubes were destroyed during this treatment, as they were lying shattered in the corner of the oven. Due to the previous arrangements of the samples it was possible to draw the conclusion that the two destroyed tubes pertained to MK4 and MK5 from charge I. As a result of this incident it was not possible to differ between them, since they completely changed their previous position. Despite their shattering, the samples were still left in the destroyed tubes. Since it was more than enough left to perform further measurements, it was nonetheless decided to analyze them as their results would still be interesting in comparison with the others. For the further experiments these samples were marked with a question mark to keep in mind that they are both exchangeable. Fortunately the other samples were mostly undamaged, only sample MK5 was shifted probably by reason of the bursting quartz tubes.

As before the samples were examined after the thermal treatment to draw conclusion about the chemical reaction during this heating process. The results are shortly described below:

- MK10: The sample lost its cylindrical form, as already observed within the preliminary tests. It had a silver color and did not show any pores at the first glance. Further on it did not connect durably to the glass surface during the thermally processing.
- MK11: Again the sample lost its cylindrical form and lay loose in the quartz tube. Its upper side appeared matt black and homogenous, whereas the underside was silver-gray with pores. Around the sample´s reclining surface the glass was steamed up a little bit with sulfur, whereas on the other side the glass wall was a little blackened. One part of the quartz tube was splashed outside with a dark brown liquid. The glass wall was slightly molten at this point. This was caused by the destroyed samples.
- MK12: As before the sample lost its cylindrical form and lay loose in the quartz tube. It appeared again silver-gray with pores. The glass was steamed up with sulfur, but no black deposits could be found. Remarkable with this sample was the fact that the quartz tube showed a little puncture at its wall. The hole appeared to be clean. Therefore it could be considered that no raw material escaped through this opening. Probably the quartz tube had a hairline fracture, which could not stand the building temperature and pressure.
- MK13: The sample lost its cylindrical form, lay loose in the quartz tube and was of a silver color. It had an even matt surface on top, the metallic bottom showed many pores, again yellowish sulfur deposits were found on the inside glass wall.
- MK7: The sample lost its cylindrical form and this time its bottom side had reacted with the glass wall. Like the others it had a silver color and showed porosity. No sulfur or other deposits could be detected. The outside of the quartz tube was again splashed by the exploded sample due to the sample position.

- MK6: The sample shows a great similarity to MK7, it lost its cylindrical form and reacted with the glass wall. The sample was so firmly fixed with the quartz tube, that it had to be detached with a hammer. Thereby the sample lengthwise broke. It had a silver color and appeared very porous. There were yellowish sulfur and a bit copper deposits on the inside of the glass wall. The outside of the quartz tube was again splashed by the exploded sample.
- MK4/5: The two samples are discussed under one point, due to their indistinguishability. During the heating process they were laying in the left rear corner, but as a result of an inexplicable explosion, they were hurled to the right rear corner and changed position. As they were lying next to each other a differentiation was not possible. Generally, one quartz tube was lengthwise cracked, the other was destroyed more. In both cases the samples were still laying in the tubes, but they were not directly fused with the glass. This indicates that one or both quartz tubes must have exploded while cooling after passing the melting point. Otherwise the samples must have flowed or degased outside for the most of the part and no specimens had been left in the glass wall. An explanation for this could be that the quartz tube maybe had some previous cracks, which could not stand the building up temperature or pressure during the reaction. At some point during the cooling the glass wall bursted, causing such a force to destroy the adjacent glass tube or this incident occurred for both samples.

II.B.3. Mechanical Processing

II.B.3.1. Preliminary Tests

Subsequently the samples were ready to be analyzed by X-ray diffraction (XRD) and for measurements of the Seebeck coefficient and electrical conductivity. For the purpose of these measurements the samples were cut into rectangular pieces with a saw equipped with a diamond-tipped cutting disc (ISOMET, 11-1180 Low Speed Saw, BUEHLER LTD.). The leftovers accumulated during this process were used for the XRD. The first differences between the samples already showed at this point. Sample MK2 and MK3 were easy to cut, they only needed a few hours, sample MK1 however took one and half day. MK2 appeared like a kind of dark grey single crystal, the molten pellet was very fragile and broke away during the cutting. Sample MK1 was a metallic, very solid material with dispersed small pores.

The hardness of sample MK3 was between them. It appeared that the pellet somehow reacted at the bottom with the quartz tube. The cut surface showed more and larger pores, particular interesting were some areas of what seemed like pure cooper in the otherwise silver metallic sample.

II.B.3.2. Charge I and II

The samples of charge I and II were cut in the same manner as described above (section *II.B.3.1. Preliminary Tests*, page 66) to prepare them for the further measurements. MK4*, MK5*, MK6 and MK7 (charge I) showed a similar degree of hardness, it would take between 3 and 4 hours to perform a long cut. In comparison with MK10, MK11, MK12 and MK13 (charge II), it appears that these samples showed also a similar hardness, except for MK12 which needed much more time for a single cut. The inner side of all samples showed more or less pores, partly also fine cracks. A behavior related to the preliminary tests. These pores could be due to the degassing of compounds like Sulfur during the thermal treatment.

II.B.4. X-Ray Diffraction

Before starting the XRD the pellet residues had to be carefully grinded with a mortar and pestle in an alcoholic ethanol solution to avoid unwanted friction. Afterwards the fine powder was transferred to a glass plate and fixed with vaseline. In a powder sample crystallites are randomly orientated. Therefore a carful homogenisation of the sample is important to get valuable results. The X-ray diffraction measurements were carried out with the Siemens XRD Diffraktometer D5000 with the following parameters (Table II.10):

Table II.10: XRD

Measuring Period	20 h
Step Time	16.0 s
Step Size	0.02 °
Angle	10 – 100 °
Scan-Type	Continous
X-Ray Source	Copper Anode

The results of the X-Ray diffraction patterns for each sample are discussed in chapter *II.C.1. X-Ray diffraction* (page 69). After finishing these measurements, emphasis was also placed on the Seebeck coefficient and electrical resistance at high temperatures.

II.B.5. Seebeck Coefficient and Electrical Resistance

To measure the Seebeck Coefficient and Electrical Resistance of the sample (preliminary tests, charge I and II) at high temperatures the ULVAC ZEM-3 was used. This device allows a measuring range from room temperature to 1000 °C by using a 4-point-method.

This method consists of overall four contacts, two inner contacts for the voltage and temperature gradient and two outer ones for the current. To obtain better results the contacts are mechanical pressed at the sample surface. For this kind of measurement it is necessary to work under noble gas atmosphere, in this case Helium, to avoid unintentional chemical reactions with the atmospheric oxygen.

The samples were analyzed at a temperature range from rt to 550 °C and vice versa in 25/50 °C steps. To obtain correct results, the Seebeck coefficient and electric resistivity were measured three times on each temperature step, each time with a slightly different gradient. In this manner a mean value could be calculated. [33]

Unfortunately it was not possible to obtain values for sample MK3 despite of repeated tries, since the resistance was way too high, forcing the device to shut down. Sample MK1 and MK2 showed promising results. However for MK2 it appeared that during the measurement some kind of reaction took place as the material afterwards had turned darker in color and seemed more porous. The samples of charge I and II were measured partly, to be precise MK6 and MK7 (charge I) as well as MK11 and MK13 (charge II). Of course the measurements of the other samples will be performed in the future in the bachelor thesis of A. Müller. [47]

The results of these analyses will be discussed in *chapter II.C.2.Seebeck Coefficient and C.3.Electric Resistivity* (page 81 and 86).

II.C. Results and Discussion

This following chapter covers the results of the X-Ray diffraction, the Seebeck coefficient and the electric resistivity at high temperatures (550 K) for the samples of the preliminary test, charge I as well as charge II.

II.C.1. X-Ray diffraction

The crystal structures of the samples were analyzed with the theoretical background of Bragg's law (see chapter *II.A.3.X-Ray Diffraction,* page 54). The experimental data for the measurement can be found in chapter *II.B.Experimental* under point *II.B.4 X-Ray Diffraction* (page 67).

For the evaluation of the obtained diffractograms the program PowderCell (version 2.4.) was used. The experimental values were compared to a number of validated examples, which had similar or identical molar ratios to the target compounds. A comparative library was created with the program FindIt and it did contain the following copper(I)sulfide compounds with their corresponding crystal structures: Cu_7S_4 (ICSD: 16011), $Cu_{1.6}S$ (ICSD: 628786), $Cu_{1.78}S$ (ICSD: 106569), $Cu_{1.8}S$ (ICSD: 69756), $Cu_{1.8}S$ (ICSD: 95395), $Cu_{1.94}S$ (ICSD: 10100), $Cu_{1.95}S$ (ICSD: 42709), Cu_2S (ICSD: 16550), Cu_2S (ICSD: 23596), Cu_2S (ICSD: 100333), Cu_2S (ICSD: 53329), Cu_2S (ICSD: 200989), and Cu_2S (ICSD: 202785). [48]

These well-known crystal structures were compared with the diffractograms obtained at the preliminary test, charge I as well as charge II. In this manner it was possible to analyze each sample in relation to their crystal structure and chemical composition. Refinements were applied because the idealized crystal structures of the library did not find the measured values exactly enough. Some diffractograms could not be matched completely. In this case, the most appropriate crystal structure was chosen. In the following chapters *II.C.1.1.Preliminary Test* to *II.C.1.3.Charge II* each sample is presented in comparison to an idealized crystal structure and their differences are discussed. In the following figures the measurement angle is plotted on the abscissa axis and the intensity on the ordinate axis. The interesting area with the peaks is between 25 and 60 °. In the left corner of each diffractograms the percentage of the idealized phase, which can be found in the raw data, can be seen. In general, the samples show very similar diffraction patterns. The crystal structures of Cu_2S Chalcosite (ICSD: 23596, monoclinic crystal system) in combination with Chalcocite-Q (ICSD: 16550, tetragonal crystal system) appeared to be the most suitable ones, with only MK2 as an exception. The samples were also checked with a pure copper diffractogram to see if there were any copper traces left. The results were negative for all samples. But it should be kept in mind that the limit of detection is around 5 % with regard to the sample. The quite high base line can be explained by amorphous parts in the sample material.

II.C.1.1. Preliminary Test

The following figures show the diffractograms obtained of sample MK1, MK and MK3. In figure II.C.1.1, the raw data of MK1 and the fitting crystal structure of the Cu_2S Chalcosite Monoclinic crystal system (ICSD: 23596) can be found:

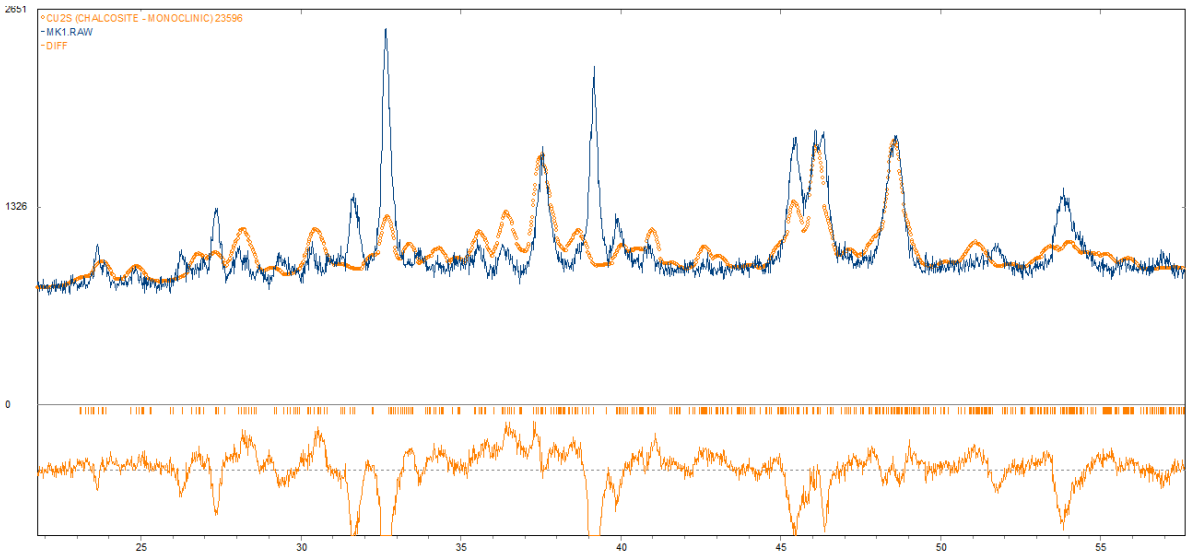

Figure II.C.1.1: Diffractogram MK1, blue line = measured values, orange circle = Cu_2S Chalcosite Monoclinic crystal system (ICSD: 23596), orange line beneath = difference

One can see that there are many similarities between the peaks of the raw data (blue) and the idealized crystal system (orange). However, there are still some peaks which cannot be found in the diffractogram of Cu_2S Chalcosite (ICSD: 23596). Therefore a second idealized diffractogram, Chalcocite-Q (ICSD: 16550), was used (figure II.C.1.2) and the differences become less pronounced:

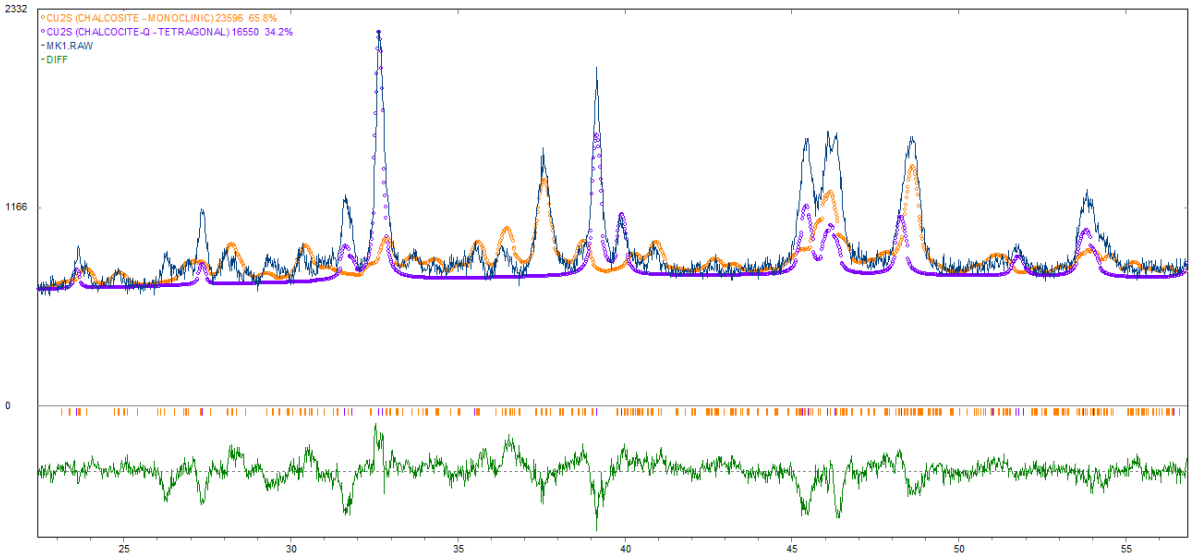

Figure II.C.1.2: Diffractogram MK1, blue line = measured values, orange circle = Cu_2S Chalcosite, monoclinic crystal system (ICSD: 23596), purple circle = Cu_2S Chalcocite-Q, tetragonal crystal system (ICSD: 16550), green line beneath = difference

Figure II.C.1.3 presents the results of sample MK2 (molar ratio $Cu_{1.8}S$), which diffractogram exhibits the largest differences. This is due to the different molar ratio. This also affects the appearance and behavior of the sample. The diffractogram shows nearly completely different peaks. It was not possible to find a completely fitting comparable crystal structure, but the best match was $Cu_{1.85}S$ Digenite (ICSD: 95359):

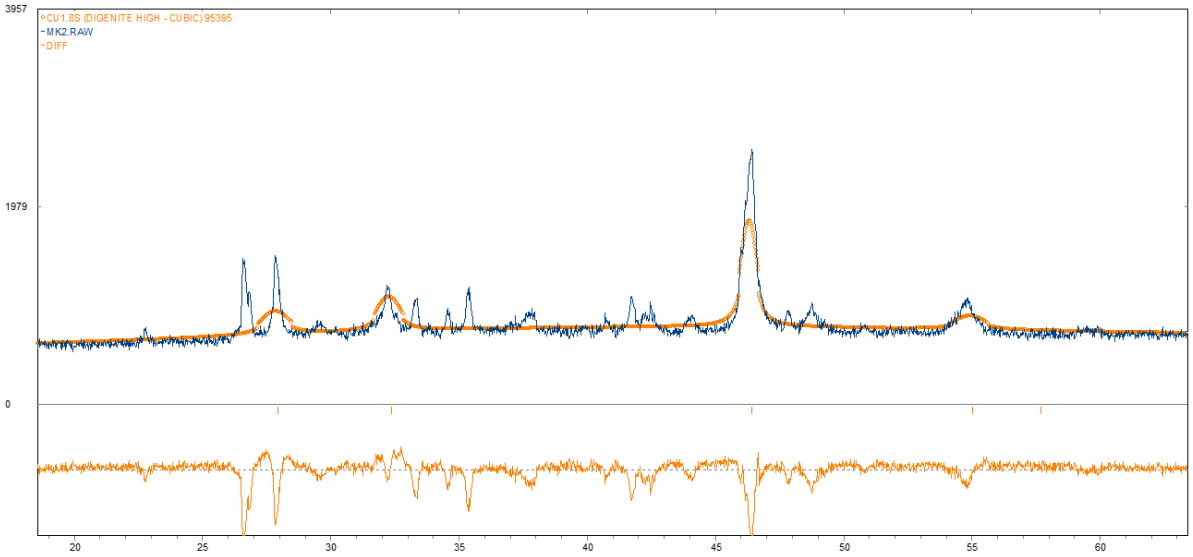

Figure II.C.1.3: Diffractogram MK2, blue line = measured values, orange circle = $Cu_{1.85}S$ Digenite, high cubic crystal system (ICSD: 95359), orange line beneath = difference

The diffractogram of sample MK3 ($Cu_{2.2}S$) fits the crystal structure of Cu_2S Chalcosite (ICSD: 23596) precisely, as one can see in figure II.C.1.4. Not a single peak is too much and the difference (orange line beneath) shows hardly any deviations:

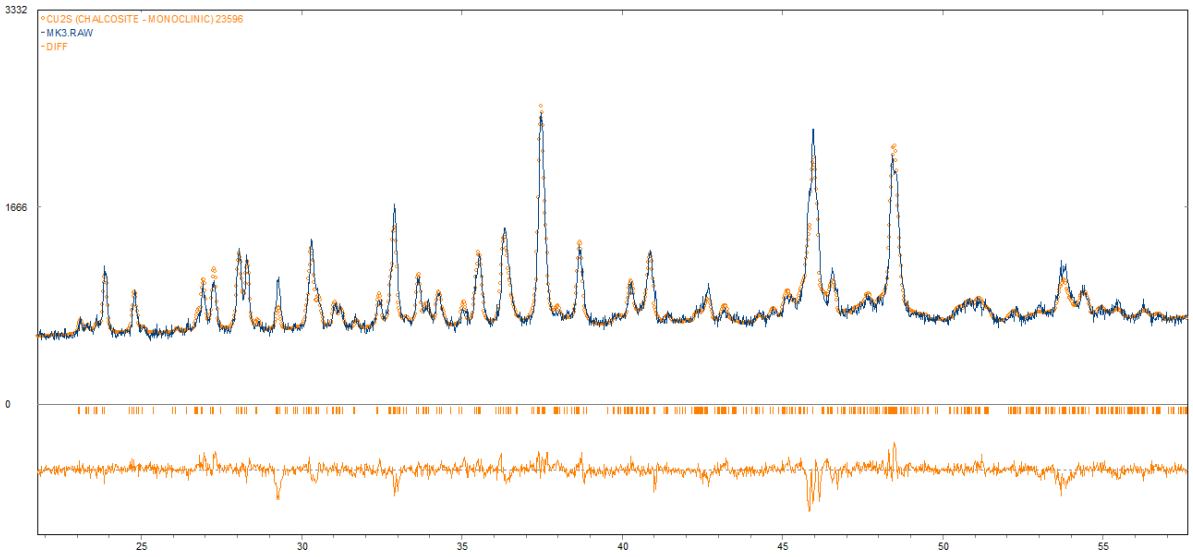

Figure II.C.1.4: Diffractogram MK3, blue line = measured values, orange circle = Cu_2S Chalcosite Monoclinic crystal system (ICSD: 23596), orange line beneath = difference

II.C.1.2. Charge I

The diffractograms of charge I follow the trend of sample MK1. There are many similarities between the raw data and the crystal structure of Cu_2S Chalcosite (ICSD: 23596) with one certain not matching peak around 40 ° (figure II.C.1.5 and II.C.1.7). Again the second comparable diffractogram, Chalcocite-Q (ICSD: 16550), was added (figure II.C.1.6 and II.C.1.8) to minimalize the differences. By the circumstances which are stated above it was not possible to differ between MK4 and MK5. Therefore a star was put over these samples:

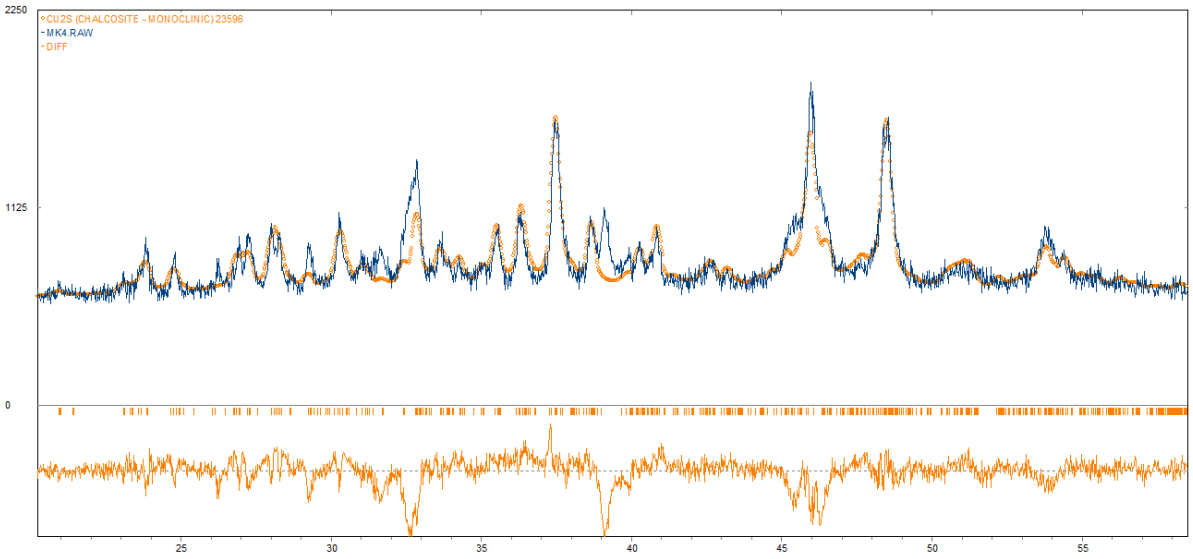

Figure II.C.1.5: Diffractogram MK4*, blue line = measured values, orange circle = Cu_2S Chalcosite Monoclinic crystal system (ICSD: 23596), orange line beneath = difference

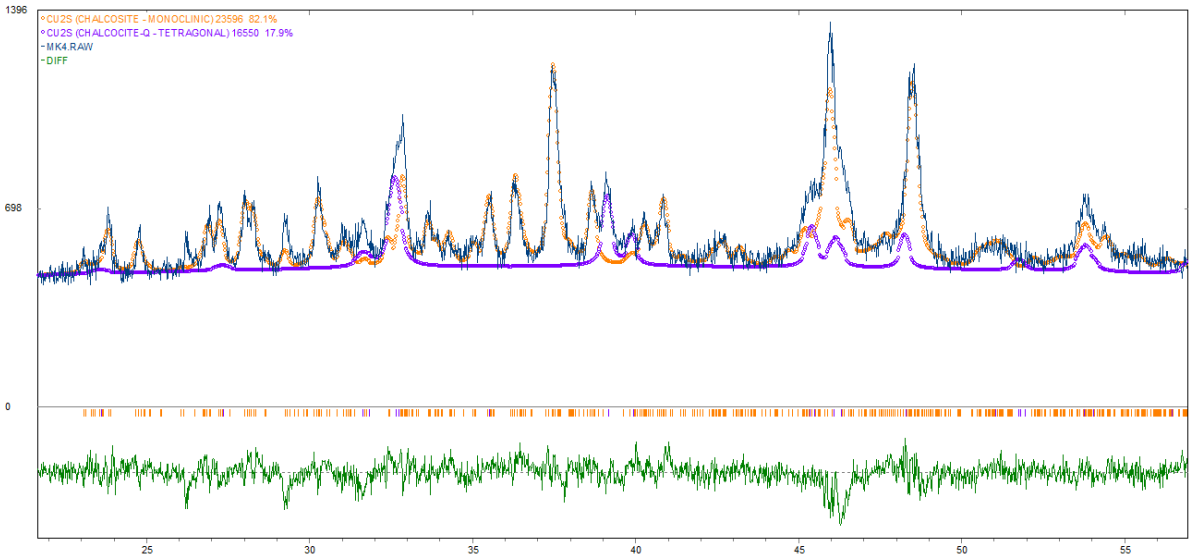

Figure II.C.1.6: Diffractogram MK4*, blue line = measured values, orange circle = Cu_2S Chalcosite, monoclinic crystal system (ICSD: 23596), purple circle = Cu_2S Chalcocite-Q, tetragonal crystal system (ICSD: 16550), green line beneath = difference

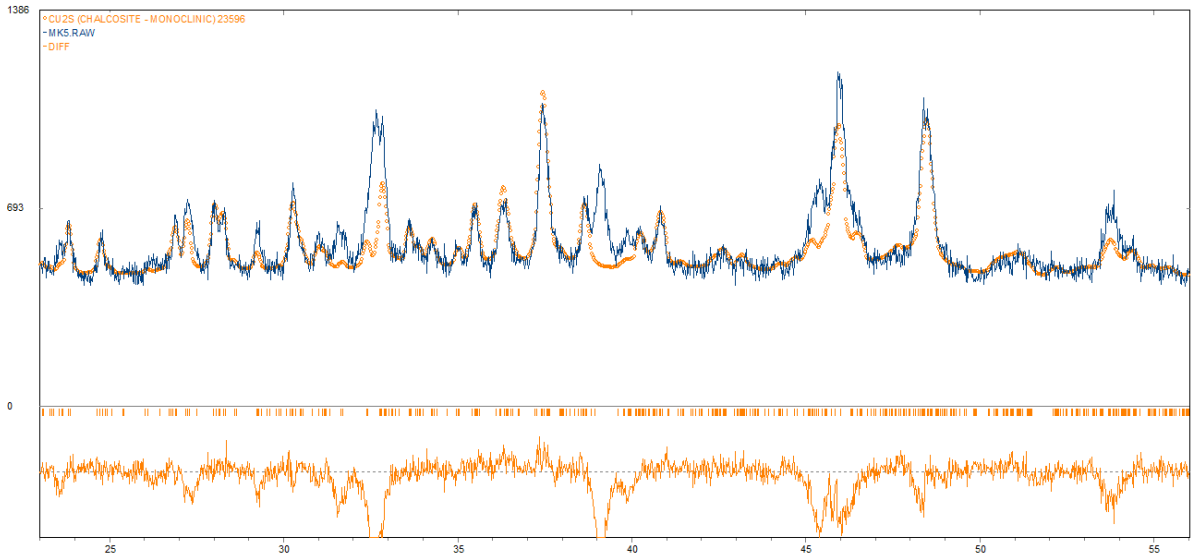

Figure II.C.1.7: Diffractogram MK5*, blue line = measured values, orange circle = Cu_2S Chalcosite Monoclinic crystal system (ICSD: 23596), orange line beneath = difference

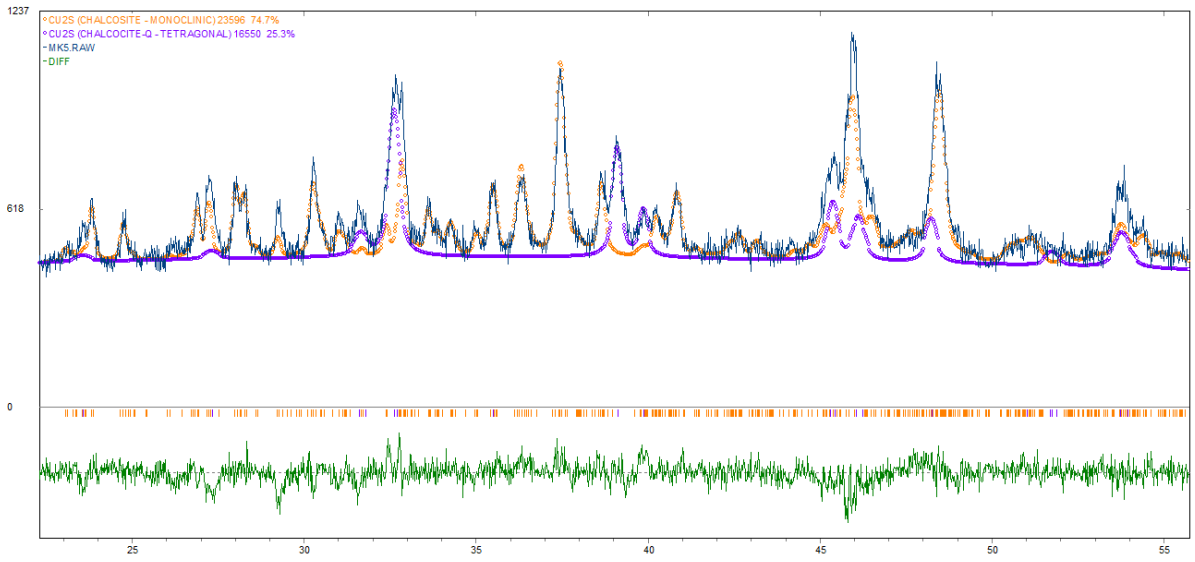

Figure II.C.1.8: Diffractogram MK5*, blue line = measured values, orange circle = Cu_2S Chalcosite, monoclinic crystal system (ICSD: 23596), purple circle = Cu_2S Chalcocite-Q, tetragonal crystal system (ICSD: 16550), green line beneath = difference

Sample MK4* and MK5* show very similar results regarding to their diffractograms, and the difference is quite pleasing. The molar ratio for MK4 was $Cu_{1.98}S$ and for MK5 $Cu_{1.96}S$.

The following figures II.C.1.9 and II.C.1.10 show the results of the X-ray diffraction for sample MK6 (molar ratio $Cu_{1.94}S$). The same crystal structures were used as before for MK1, MK4* as well as MK5*. Again comparable results are obtained:

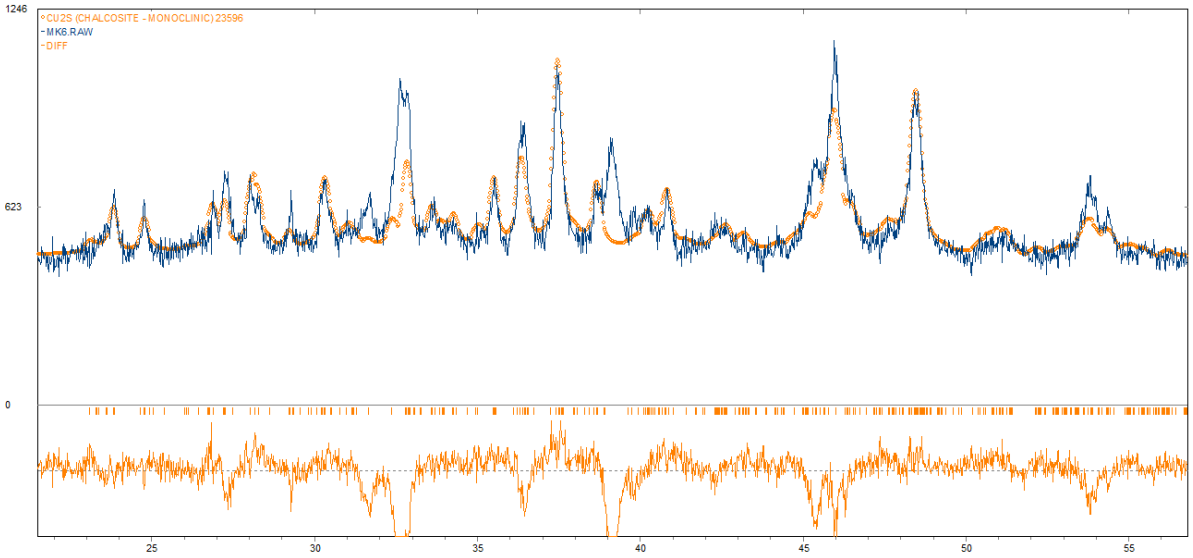

Figure II.C.1.9: Diffractogram MK6, blue line = measured values, orange circle = Cu_2S Chalcosite Monoclinic crystal system (ICSD: 23596), orange line beneath = difference

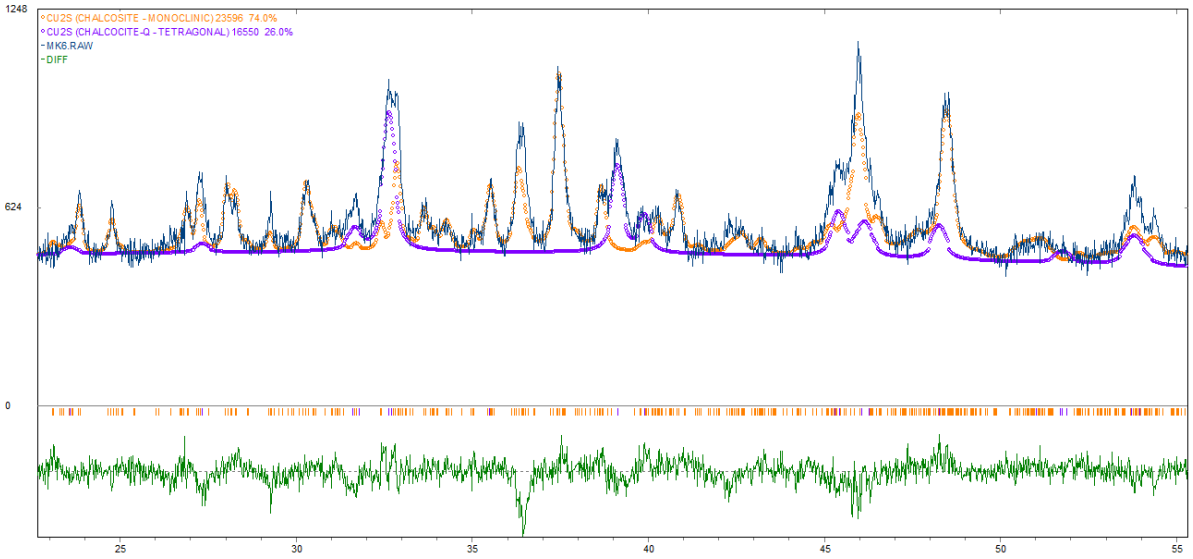

Figure II.C.1.10: Diffractogram MK6, blue line = measured values, orange circle = Cu_2S Chalcosite, monoclinic crystal system (ICSD: 23596), purple circle = Cu_2S Chalcocite-Q, tetragonal crystal system (ICSD: 16550), green line beneath = difference

Sample MK7 (molar ratio $Cu_{1.92}S$) is the first example of charge I to show differences compared to the others. This could be due to the molar ratio, which is lower than for the other samples of charge I. As one can see in the diffractogram (figure II.C.1.11) underneath approximately three peaks are missing (between 20 and 40 °), which can be found in the other diffractograms of charge I. The same crystal structures Cu_2S Chalcosite (ICSD: 23596) and in addition Chalcocite-Q (ICSD: 16550) were used in the absence of a more appropriate alternative. This explains the relatively poor difference (see figure II.C.1.11 and II.C.1.12).

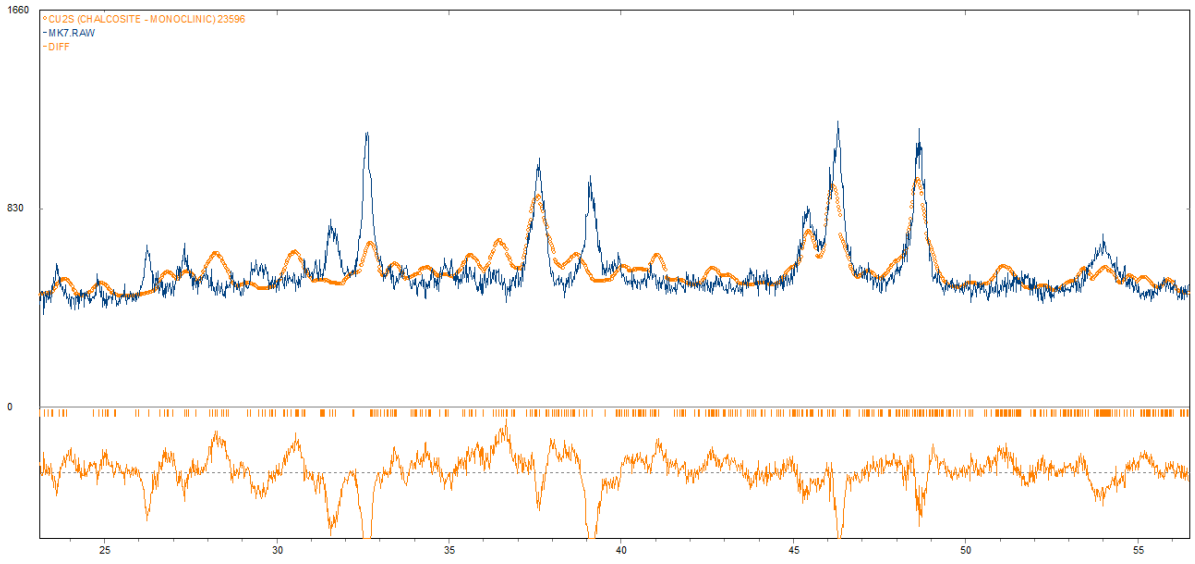

Figure II.C.1.11: Diffractogram MK7, blue line = measured values, orange circle = Cu_2S Chalcosite Monoclinic crystal system (ICSD: 23596), orange line beneath = difference

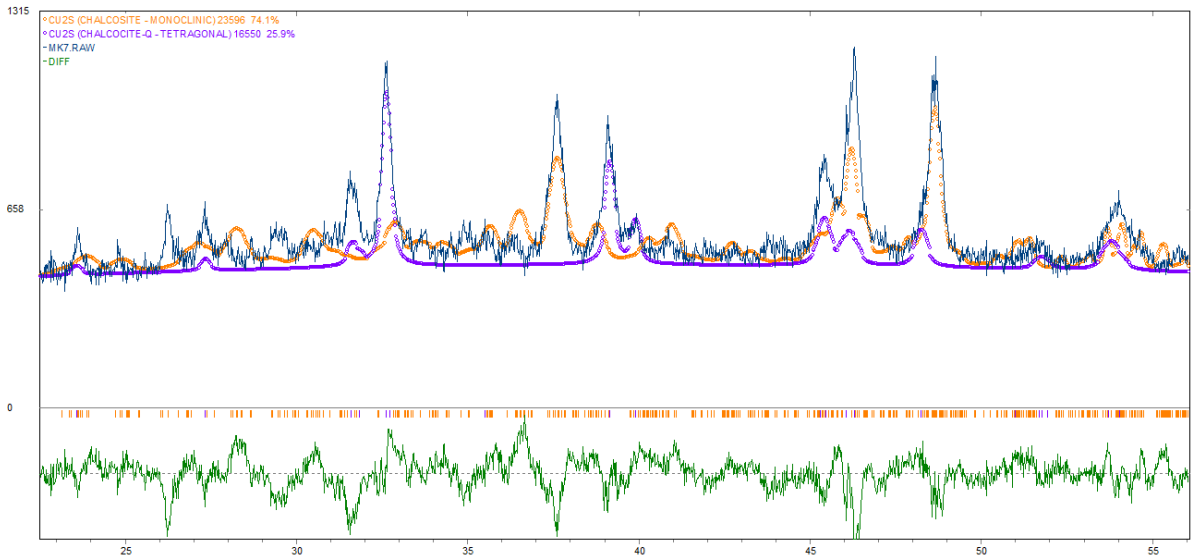

Figure II.C.1.12: Diffractogram MK7, blue line = measured values, orange circle = Cu_2S Chalcosite, monoclinic crystal system (ICSD: 23596), purple circle = Cu_2S Chalcocite-Q, tetragonal crystal system (ICSD: 16550), green line beneath = difference

II.C.1.3. Charge II

The samples of charge II (MK10, MK11, MK12 and MK13) were also analyzed by X-ray diffraction. At first the diffractogram of sample MK10 (molar ratio $Cu_{1.99}S$) is presented (figure II.C.1.13 and II.C.1.14). Once more the crystal structures Cu_2S Chalcosite (ICSD: 23596) and then in addition Chalcocite-Q (ICSD: 16550) showed the best results:

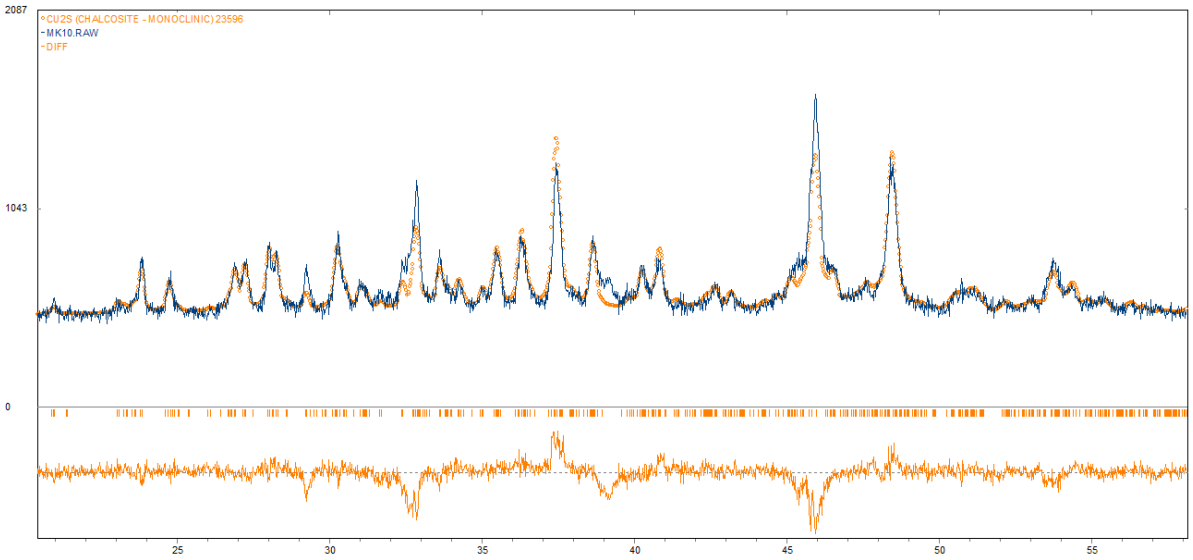

Figure II.C.1.13: Diffractogram MK10, blue line = measured values, orange circle = Cu_2S Chalcosite Monoclinic crystal system (ICSD: 23596), orange line beneath = difference

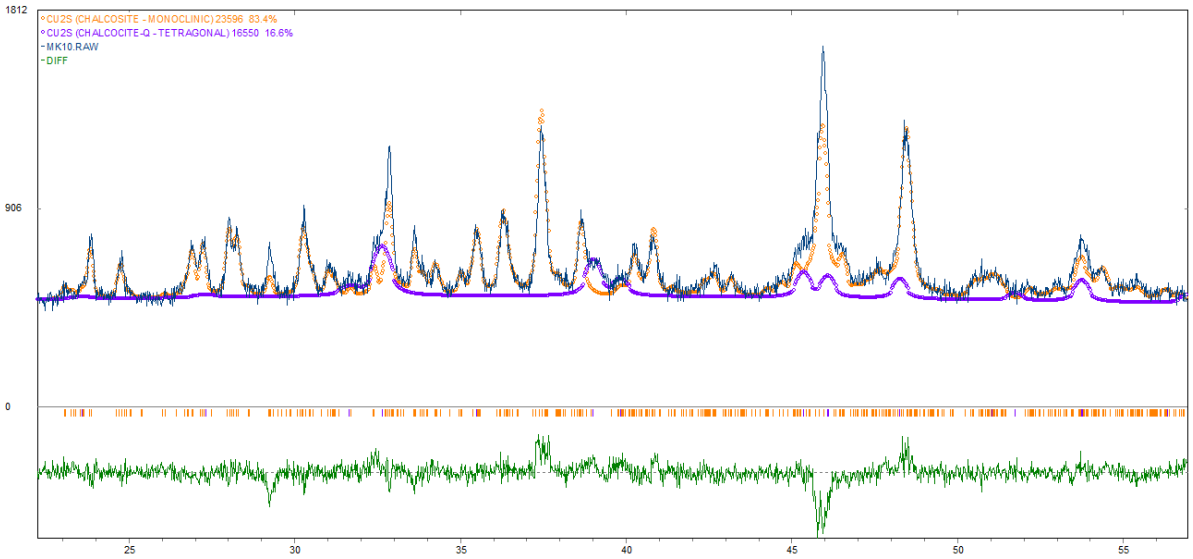

Figure II.C.1.14: Diffractogram MK10, blue line = measured values, orange circle = Cu_2S Chalcosite, monoclinic crystal system (ICSD: 23596), purple circle = Cu_2S Chalcocite-Q, tetragonal crystal system (ICSD: 16550), green line beneath = difference

A similar picture emerges when looking at the diffractogram of sample MK11 (molar ratio $Cu_{1.98}S$). Sample MK10 and MK11 have very similar molar ratios. So the comparison was made with the same crystal structures as before. The results can be found in figure II.C.1.15 and II.C.1.16:

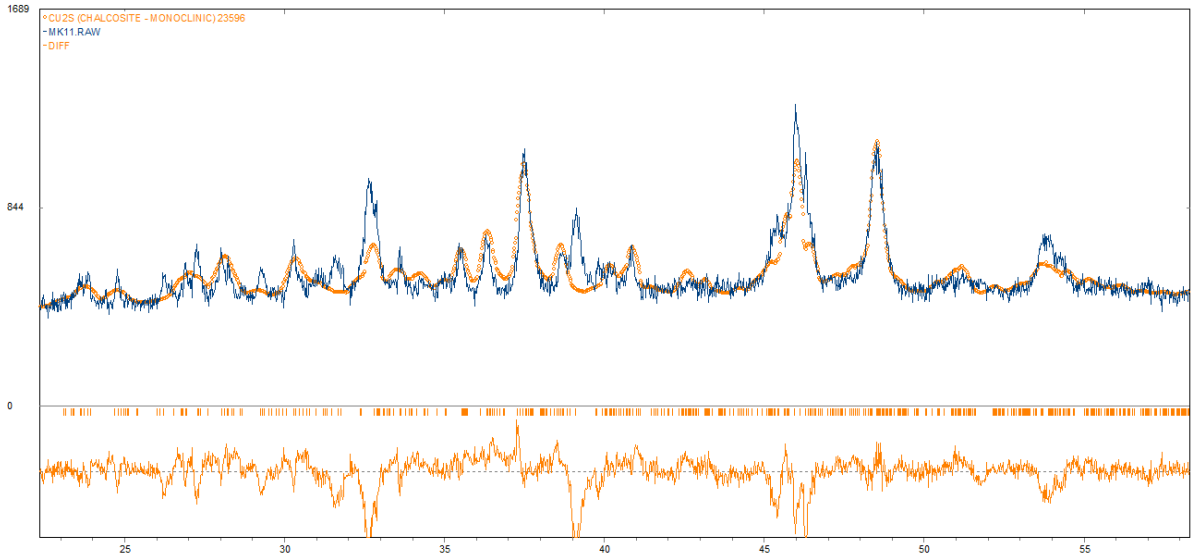

Figure II.C.1.15: Diffractogram MK11, blue line = measured values, orange circle = Cu_2S Chalcosite Monoclinic crystal system (ICSD: 23596), orange line beneath = difference

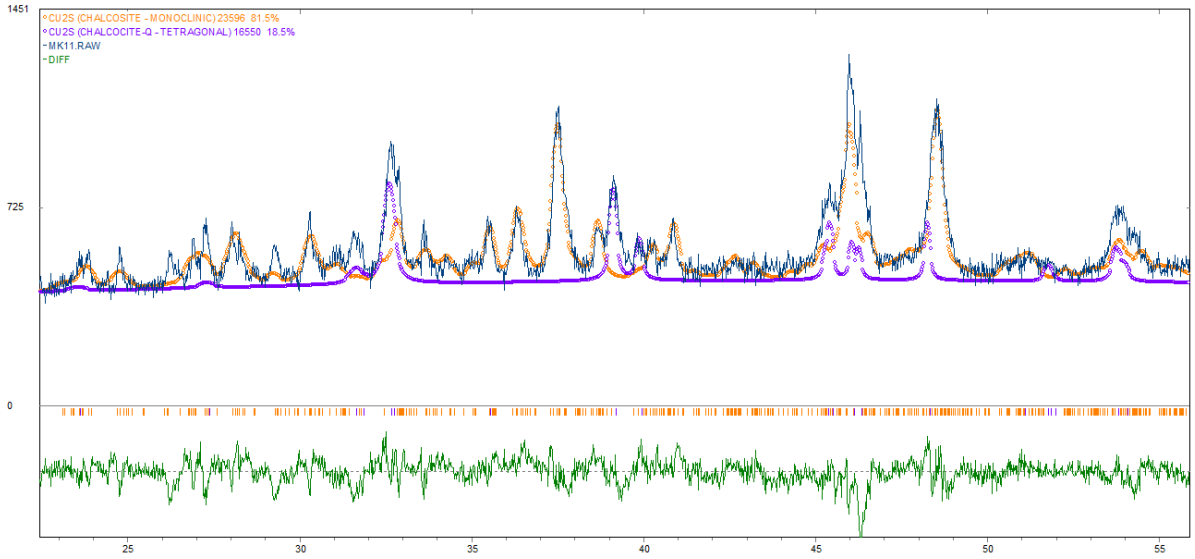

Figure II.C.1.16: Diffractogram MK11, blue line = measured values, orange circle = Cu_2S Chalcosite, monoclinic crystal system (ICSD: 23596), purple circle = Cu_2S Chalcocite-Q, tetragonal crystal system (ICSD: 16550), green line beneath = difference

Sample MK12 (molar ratio $Cu_{1.95}S$) shows compared with the other samples of charge II (MK10 and MK11) some differences (see figure II.C.1.17 and II.C.1.18). A certain number of peaks are missing (between 20 and 40 °). This trend is similar to charge I, where MK7 differs for this reason from the others. Nonetheless the same crystal structures Cu_2S Chalcosite (ICSD: 23596) and then in addition Chalcocite-Q (ICSD: 16550) were compared, since no other one fitted better. Only a quite poor difference can be observed (see figure II.C.1.17 and II.C.1.18):

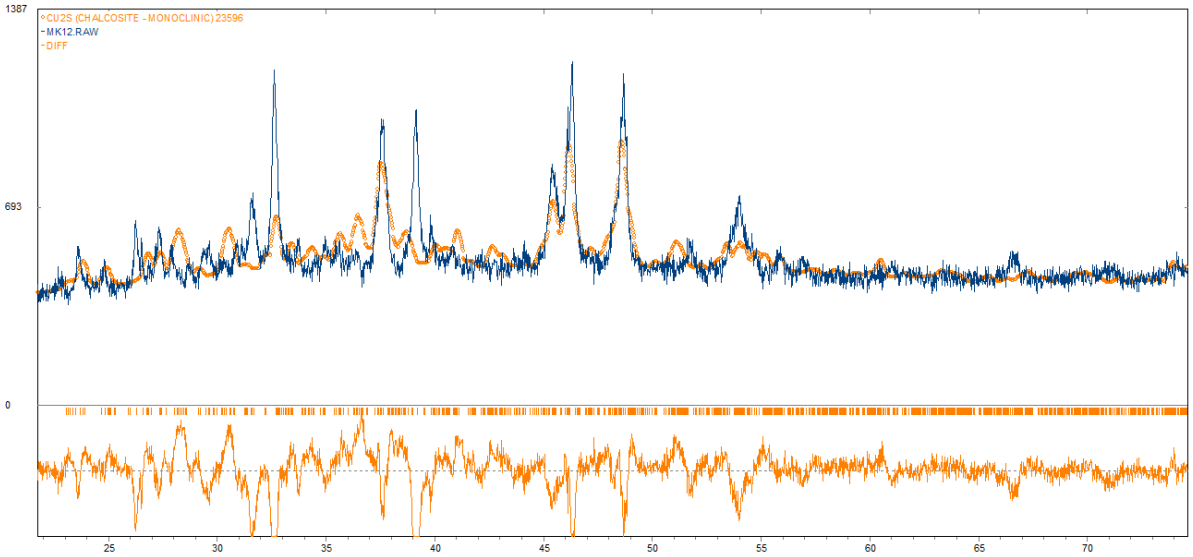

Figure II.C.1.17: Diffractogram MK12, blue line = measured values, orange circle = Cu_2S Chalcosite Monoclinic crystal system (ICSD: 23596), orange line beneath = difference

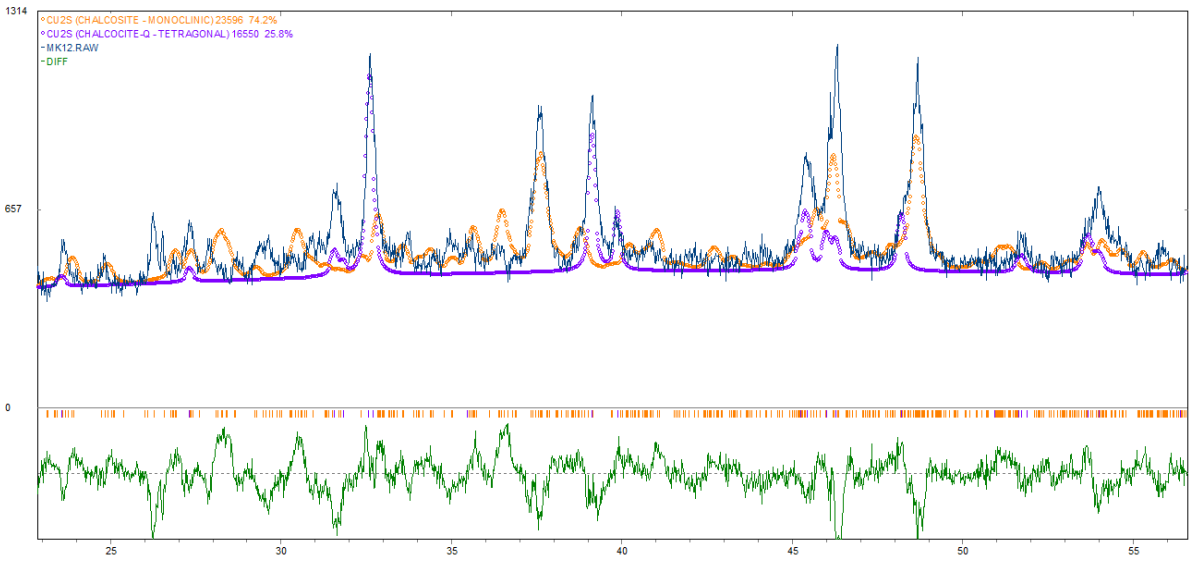

Figure II.C.1.18: Diffractogram MK12, blue line = measured values, orange circle = Cu_2S Chalcosite, monoclinic crystal system (ICSD: 23596), purple circle = Cu_2S Chalcocite-Q, tetragonal crystal system (ICSD: 16550), green line beneath = difference

Sample MK13 (molar ratio $Cu_{1.93}S$) shows a similar behavior, see figure II.C.1.19 and II.C.1.20. Its diffractogram is very similar to sample MK12 and again the same crystal structures were used for comparison and again a poor difference was received:

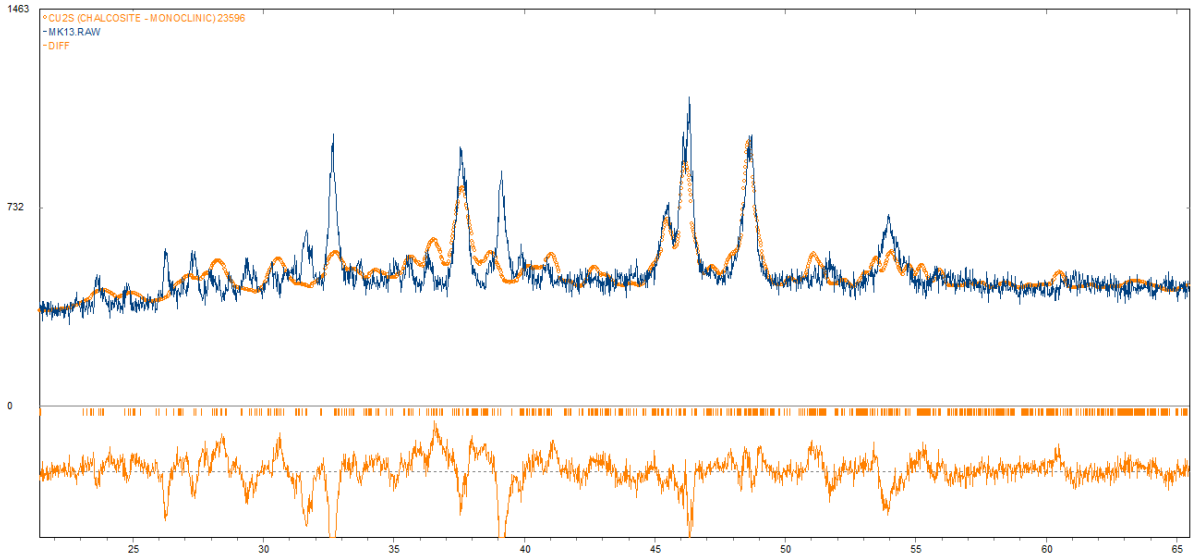

Figure II.C.1.19: Diffractogram MK13, blue line = measured values, orange circle = Cu_2S Chalcosite Monoclinic crystal system (ICSD: 23596), orange line beneath = difference

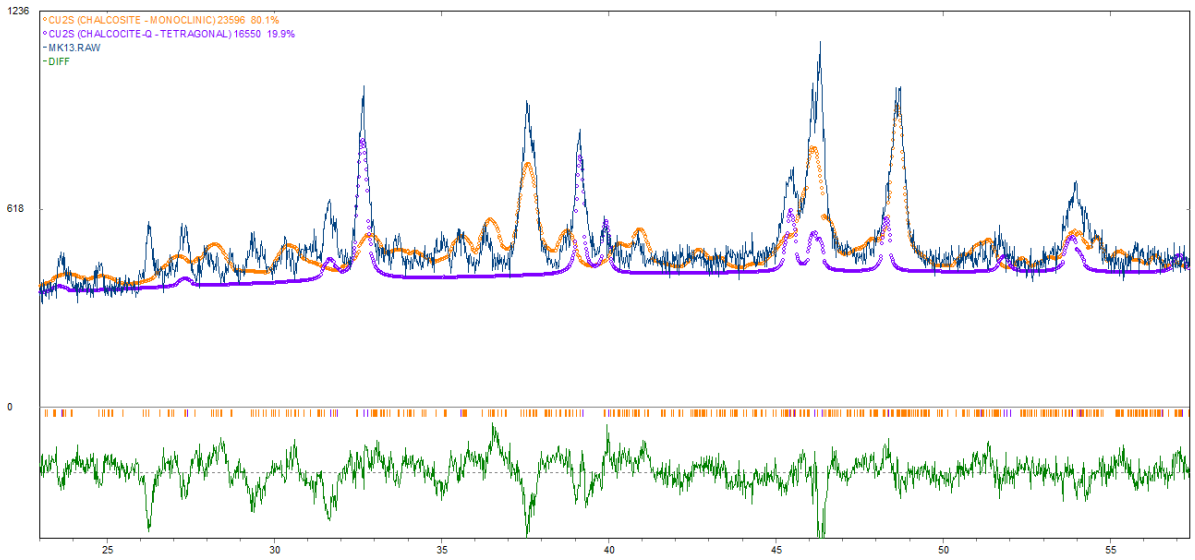

Figure II.C.1.20: Diffractogram MK13, blue line = measured values, orange circle = Cu_2S Chalcosite, monoclinic crystal system (ICSD: 23596), purple circle = Cu_2S Chalcocite-Q, tetragonal crystal system (ICSD: 16550), green line beneath = difference

Generally, the crystal structures Cu_2S Chalcosite (ICSD: 23596) and Chalcocite-Q (ICSD: 16550) showed the best results. It would be fair to assume that these crystal structures can be found in these samples. The exceptions to these results are sample MK2 with a rather different diffractogram and the samples MK7 (charge I), MK12 as well as MK13 (charge II), where the used comparison structures did not fit perfectly. These samples have the lowest molar ratio of all samples with $Cu_{1.92}S$ (MK7), $Cu_{1.95}S$ (MK12) and $Cu_{1.93}S$ (MK13). Apparently, this has an impact on the diffractograms, resulting in the poor differences. Unfortunately, no suitable diffractograms for such a low molar ratio showed better results.

It may be possible to draw a conclusion on the results of the diffractograms regarding to a chemical reaction. For samples with a molar ratio close to Cu_2S, as mentioned above, an appropriate comparison could be found. However, the sample with a lower molar ratio (around $Cu_{2-x}S$ with x =, 0.05, 0.07 and 0.08) could not be compared to diffractograms of similar compounds, but rather to the diffractograms of compounds with higher molar ratios (Cu_2S). This may indicate that these samples, despite of the chosen low molar ratio, tend to form Cu_2S during the thermal treatment. To verify this consideration further measurements are necessary.

II.C.2. Seebeck Coefficient

The Seebeck coefficient was measured with the ULVAC ZEM-3 at high temperatures (up to 550 C°). This device uses a so called 4-point-method. More details of the experimental setup can be found in chapter *II.B.Experimental* under point *II.B.3. Seebeck Coefficient and Electric Resistivity* (page 68). The results of the preliminary tests, charge I (MK6 and MK7), as well as charge II (MK11 and MK13), are in the following sections. At this time the other measurements have not been carried out yet (to be precise MK4* and MK5*) from charge I and MK10 and MK12 from charge II. These experiments will of course be performed, they will be found in the bachelor thesis of A. Müller. [47]

II.C.2.1. Preliminary Tests

Following, the results of the Seebeck coefficient measurements of sample MK1 (figure II.C.2.1) and sample MK2 (figure II.C.2.2) are illustrated. Unfortunately, it was not possible to analyze sample MK3 with this method, as its electric resistivity was too high causing the ULVAC ZEM-3 to shut down. But the other results were quite promising:

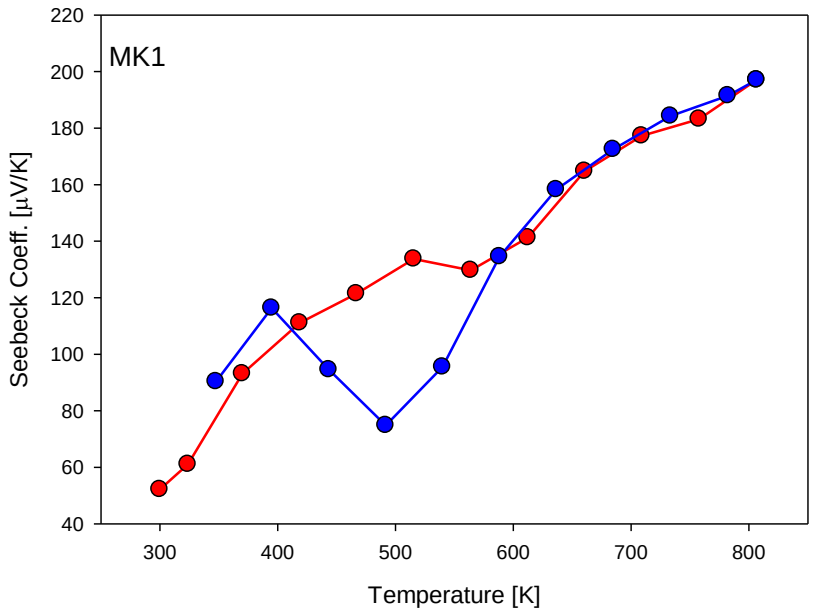

Figure II.C.2.1: Seebeck Coefficient [μvK^{-1}] as function of temperature [K], Sample MK1

In figure II.C.2.1 sample MK1 is shown (molar ratio $Cu_{2-x}S$, x =?). The red curve represents the heating process, whereas the blue curve represents the cooling. The same color scheme is used for all the other samples. The Seebeck coefficient reaches quite satisfying results, close to 200 [µV/K]. Although the exact molar ratio of this sample is unknown, due to an initial weight mistake, the outcome is still interesting. Both curves show a similar behavior at high temperatures between 600 and 800 K. Therefore the following deviating points of the cooling curve may be outliers.

The Seebeck coefficient of sample MK2 (molar ratio CuS) is displayed in figure II.C.2.2:

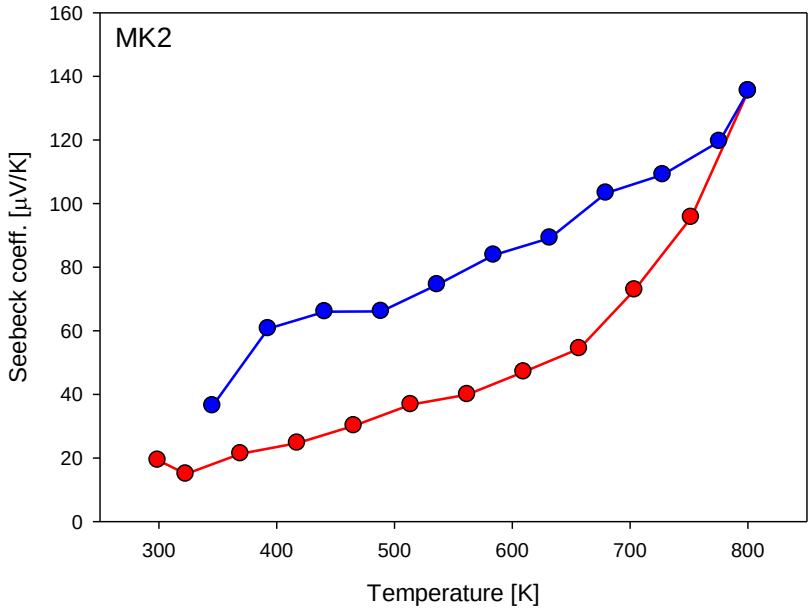

Figure II.C.2.2: Seebeck Coefficient [µvK^{-1}] as function of temperature [K], Sample MK2

As can be seen in figure II.C.2.2 the Seebeck coefficient differs noticeably between the heating and cooling phase. This could be due to errors during the measurement, which may not be caused by the porosity or shape of the sample, since the Seebeck coefficient should not be depending on them. The sample appeared like it had reacted during the measurement. This maybe implies that there was some kind of chemical reaction during the process of heating up, which resulted in a changed Seebeck coefficient. The Seebeck coefficient itself is smaller compared to sample MK1.Running a measurement several times would help to confirm such assumptions.

II.C.2.2. Charge I

The samples MK6 (molar ratio $Cu_{1.94}S$) and MK7 (molar ratio $Cu_{1.92}S$) were measured from charge I, the others will also be analyzed and the results will be, as mentioned above, found in the bachelor thesis of A. Müller. [47]

The results of the analyzed samples relating to the Seebeck coefficient are portrayed in the following figure II.C.2.3 and II.C.2.4. Sample MK6 shows very deviating results, the Seebeck coefficient reached unexpected values during the cooling phase. This sharp increase happened around 750 K. At a first view the heating and cooling curves are very different from another. A structural phase transition and hysteresis with corresponding changes in the electronic structure could be a possible cause. It is necessary to repeat the measurement of sample MK6, to verify and compare the results. In this manner it is hopefully possible to find the source of error.

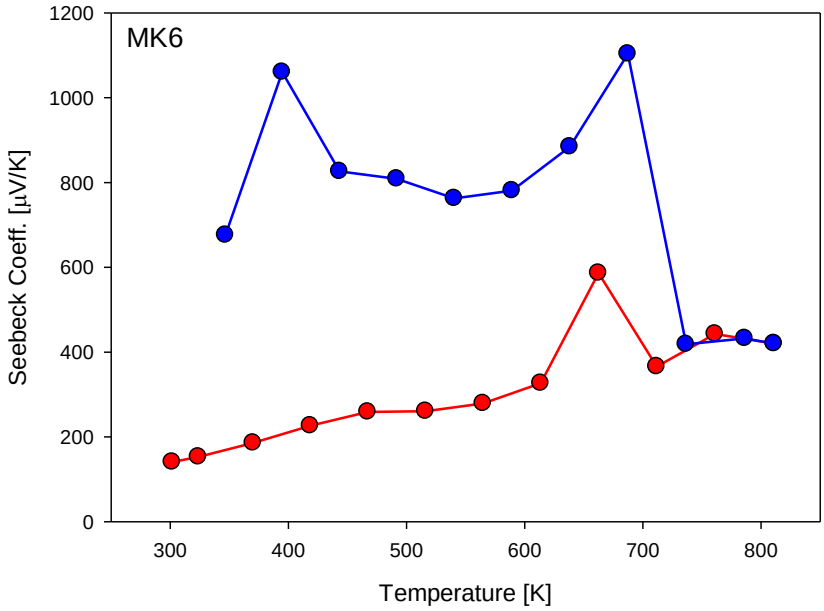

Figure II.C.2.3: Seebeck Coefficient [µvK^{-1}] as function of temperature [K], Sample MK6

MK7 (figure II.C.2.4) shows very promising approaches, in respect of both the Seebeck coefficient, which is slightly over 200 [µV/K] and the behavior of the curve. The heating and the cooling phase show a very similar trend. Although it must be added that the latter has less measuring points, which means that it does not represent this results very well.

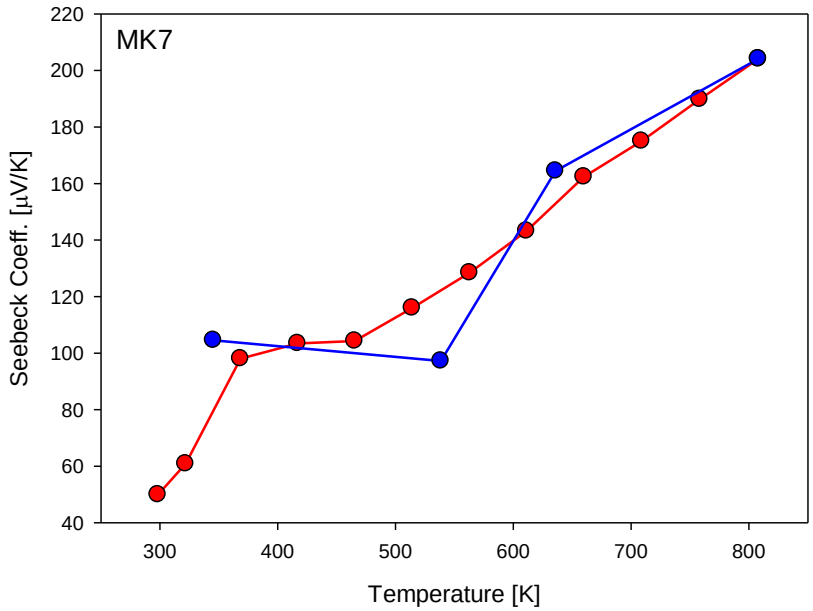

Figure II.C.2.4: Seebeck Coefficient [µvK^{-1}] as function of temperature [K], Sample MK7

II.C.2.3. Charge II

Until now sample MK11 (molar ratio $Cu_{1.98}S$) and MK13 (molar ratio $Cu_{1.93}S$) were analyzed regarding to their Seebeck coefficient. MK13 was measured two times, since it appeared that the positioning of the sample in the ULVAC ZEM-3 device changed during the measurement. In this manner, it could also be checked if the sample itself changes as a consequence of the heating up process.

In figure II.C.2.5 the results of MK11 are presented. This sample shows the highest Seebeck coefficient of all so far measured samples, around 210 [µV/K]. The heating curve has a regular course, as well as the cooling curve between 650 and 850 K. At lower temperatures, some measuring points start to vary. These could be again explained by outliers. Thus, measurements with more measuring points would be interesting.

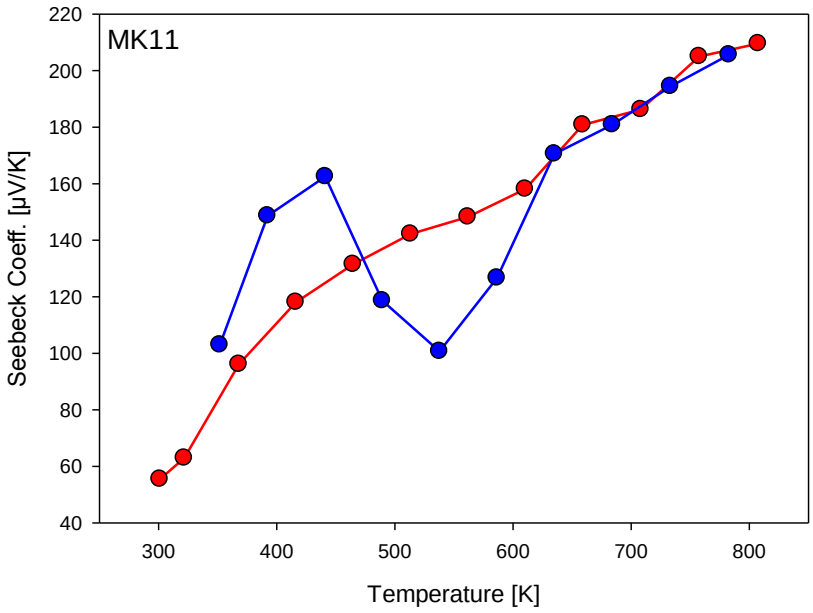

Figure II.C.2.5: Seebeck Coefficient [µvK^{-1}] as function of temperature [K], Sample MK11

Sample MK13 is portrayed two times, since as described above it appeared to be shifted after the measurement. In figure II.C.2.6 the first measurement and in figure II.C.2.7 the second measurement are shown. Both measurements have a quite similar value for the Seebeck coefficient, between 160 and 180 [µV/K], whereby the latter has a slightly higher one. These results are therefore also quite promising. The behavior of the curves in regard to the heating phase show more differences, but this could be due to outliers. The cooling phases cannot be compared that easily, since the first measurement has less measurement points:

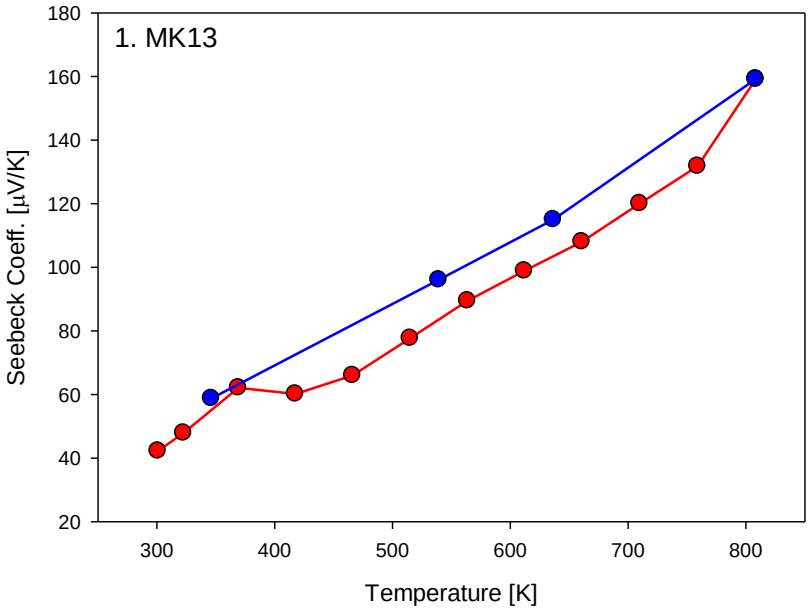

Figure II.C.2.6: Seebeck Coefficient [µvK^{-1}] as function of temperature [K], Sample MK13, 1st measurement

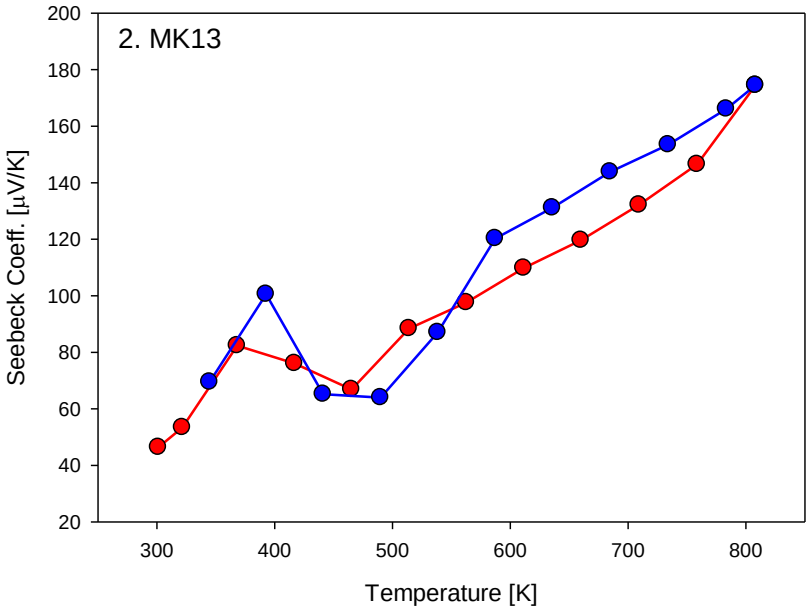

Figure II.C.2.7: Seebeck Coefficient [µvK^{-1}] as function of temperature [K], Sample MK13, 2nd measurement

Summarized, all the samples show quit promising Seebeck coefficients except for sample MK6, which will be measured again due to its extraordinary results. Compared with the results of Zhao and Snyder`s work, similar but a little bit lower results were obtained for the Seebeck coefficient, whereby in this thesis lower temperatures were used. [1]

To obtain more precise results further measurements with a larger number of measuring points at low temperatures should be carried out.

II.C.3. Electric Resistivity

The Electric Resistivity was also measured with the ULVAC ZEM-3 at high temperatures (up to 550 C°), parallel to the Seebeck coefficient. Again more details to experimental setups can be found in chapter *II.B.Experimental* under point *II.B.3. Seebeck Coefficient and Electric Resistivity* (page 68). The results of the preliminary tests, charge I (MK6 and MK7), as well as charge II (MK11 and MK13) are discussed under the following points. At this time the other measurements are still pending to be precise MK4* and MK5* from charge I and MK10 and MK12 from charge II. These samples will of course be measured and they will be found in the bachelor thesis of A. Müller. [47]
Oppositely to the Seebeck effect, the electric resistivity depends also on factors like the geometry of the sample and its quality (pores, fine cracks, etc.) All these external and internal influences must be considered, when looking at the following figures.

II.C.3.1. Preliminary Tests

As mentioned before under point *II.C.2. Seebeck Coefficient* it was not possible to analyze sample MK3, since its resistivity was way too high to measure with the ULVAC ZEM-3. The other samples of the preliminary tests are portrayed underneath (figure II.C.3.1 and II.C.3.2):

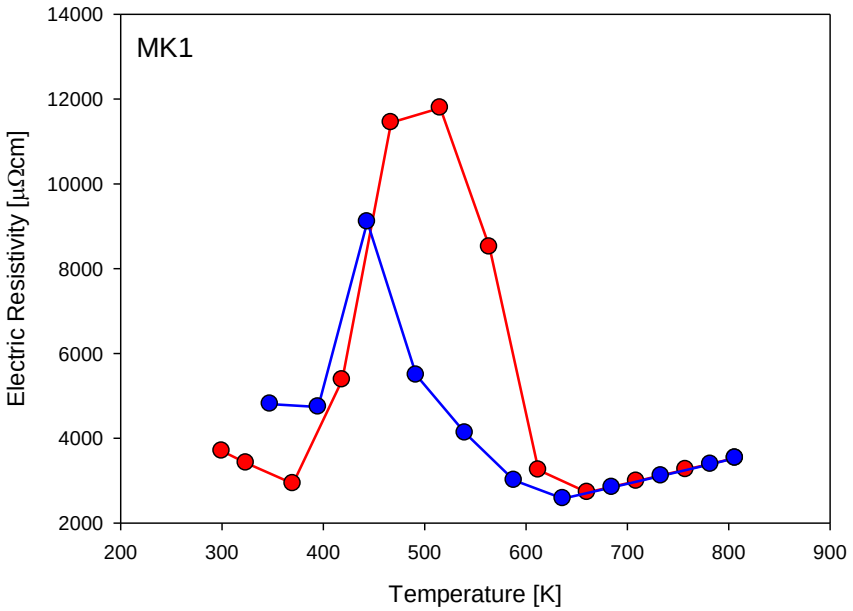

Figure II.C.3.1: Electric Resistivity [μΩcm] as function of temperature [K], Sample MK1

The electric resistivity of sample MK1 shows an interesting hysteresis between 400 and 600 K, where quite high values are reached. This could be due to a phase transition in the compound. Apart from that, the heating (red) and the cooling (blue) curve show a similar trend.

In figure II.C.3.2 the results for sample MK2 (molar ratio) are portrayed:

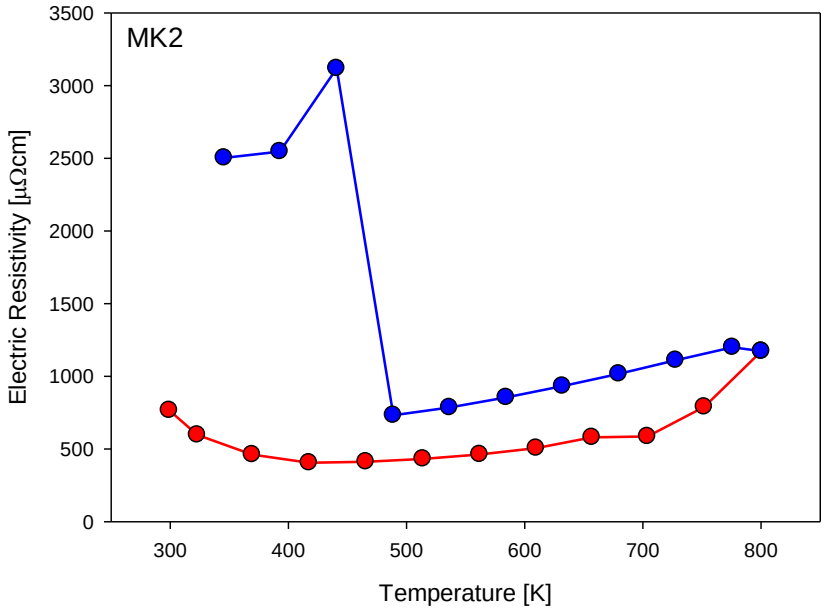

Figure II.C.3.2: Electric Resistivity [µΩcm] as function of temperature [K], Sample MK2

Here, the electric resistivity behaves quite differently and the measured values are relatively low. The curves are very similar, aside from the last measuring points of the cooling phase. This could be due to measurement failures or outliers.

II.C.3.2. Charge I

Regarding to charge I the samples MK6 (molar ratio $Cu_{1.94}S$) and MK7 (molar ratio $Cu_{1.92}S$) were analyzed. Unfortunately the results for sample MK6 were not analyzable. Therefore only the results of MK7 are shown (figure II.C.3.3):

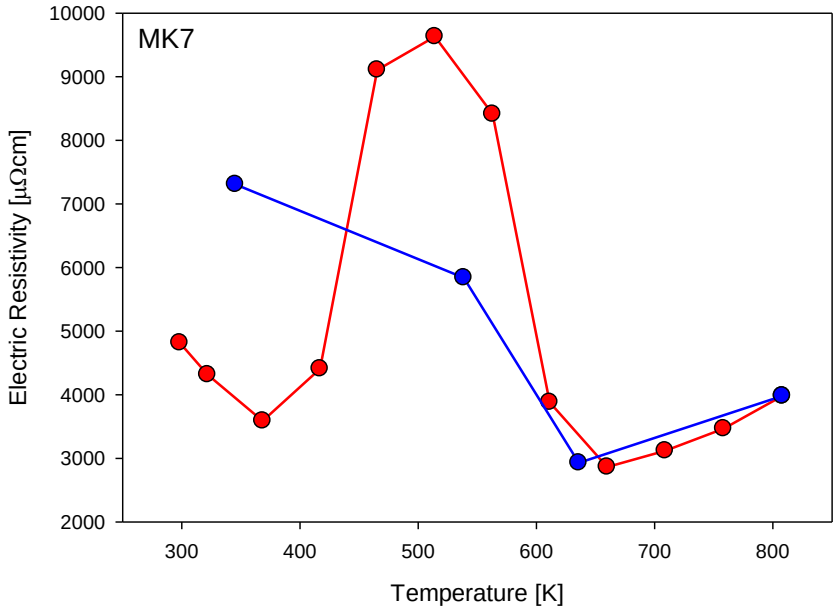

Figure II.C.3.3: Electric Resistivity [µΩcm] as function of temperature [K], Sample MK7

Quite high values for the electric resistivity were obtained for sample MK7 comparable to MK1. The heating curve also shows a similar behavior (kind of a hat shape). If one looks at the cooling phase it seems a bit off, but this could be due to the low number of measuring points. The hysteresis could again be caused by a potential phase transition.

II.C.3.3. Charge II

From charge II sample MK11 (molar ratio $Cu_{1.98}S$) and MK13 (molar ratio $Cu_{1.93}S$) were analyzed regarding to their electric resistivity. Again MK13 was measured two times, due to a slightly changing sample position after the measurement. So it could also be observed if the sample changes as a consequence of the heating up process.

In figure II.C.3.5 the results of sample MK11 are shown. Again a hysteresis with a similar shape as in MK1 and MK7 occurred, which indicates a possible phase transition. Notable are also the obtained very high values of the electric resistivity, which are more than twice as high as for the other samples:

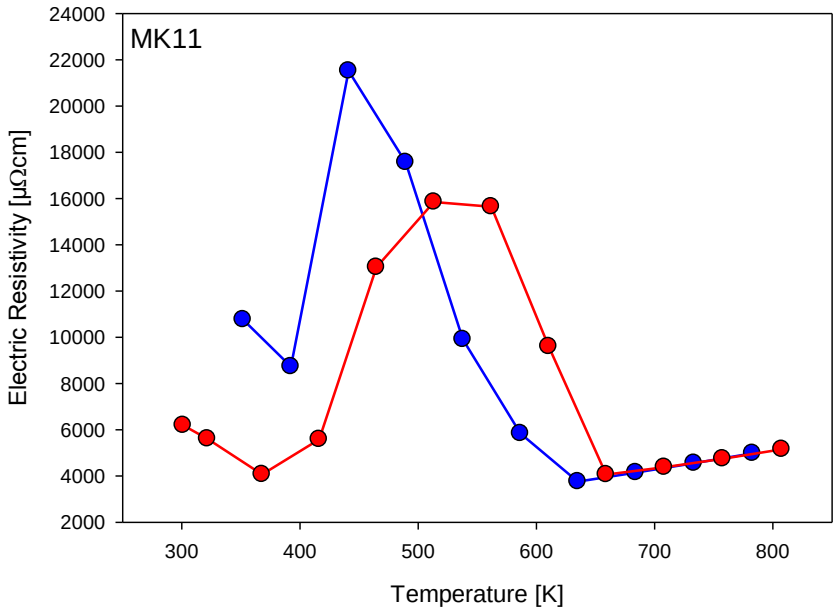

Figure II.C.3.4: Electric Resistivity [µΩcm] as function of temperature [K], Sample MK11

The first measurement of sample MK13 is portrayed in figure II.C.3.6. The lowest values for the electric resistivity were obtained here. Also the heating and cooling curve show a different trend, yet again some kind of hysteresis can be found:

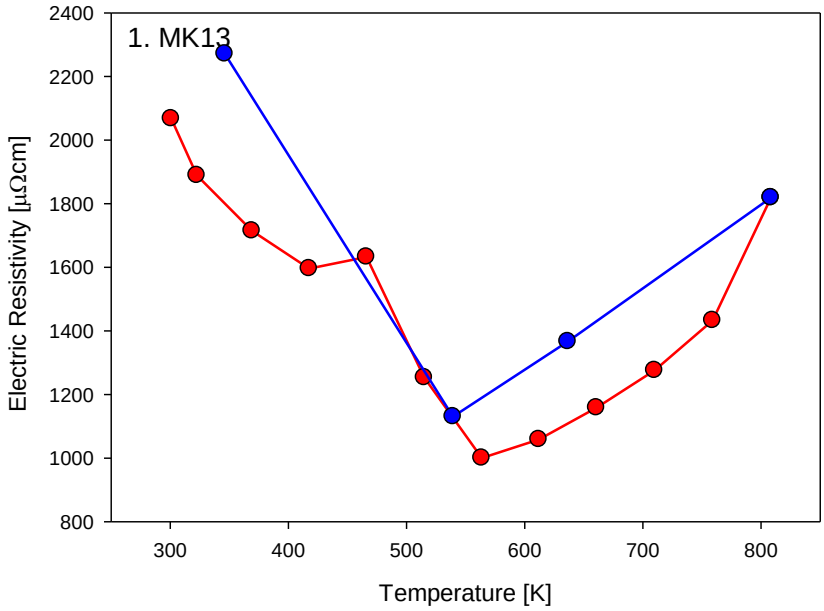

Figure II.C.3.5: Electric Resistivity [µΩcm] as function of temperature [K], Sample MK13, 1st Measurement

Comparing the first measurement of sample MK13 to the second one, it appears that the latter has the higher electric resistivity (figure II.C.3.7). The heating curve (red) takes a form similar to MK1, MK7 and MK11, which could again due a phase transition during the temperature change.

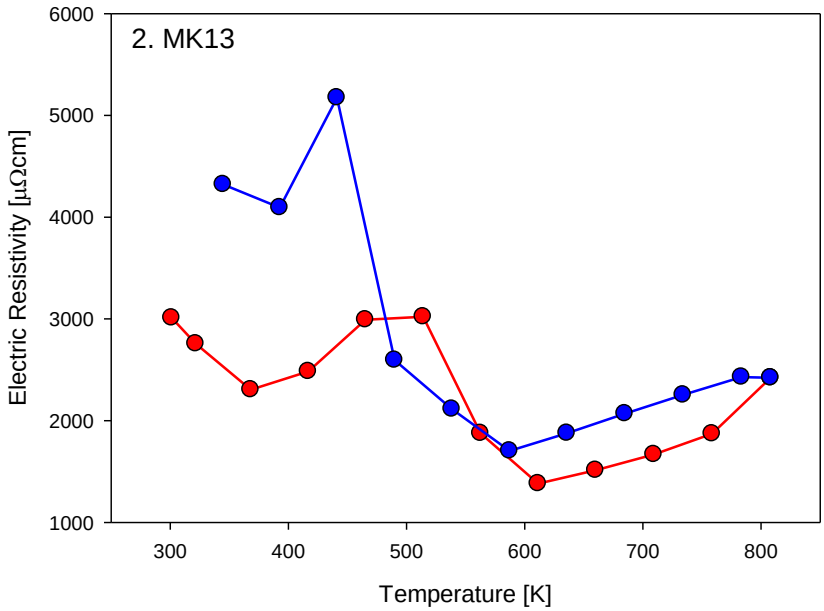

Figure II.C.3.6: Electric Resistivity [µΩcm] as function of temperature [K], Sample MK13, 2nd Measurement

Generally speaking, the accurate electric resistivity measurement is much more difficult to measure, since effective geometrical factors influences the results. Again a repetition of the measurements with more measuring points would make sense. Also experiments at low temperature would be very interesting.

II.C.4. Potential ZT-Value

A quick comparison of the obtained results of the electric resistivity ρ and the Seebeck coefficient S, which can form the power factor PF ($= \frac{S^2}{\rho}$), shows that especially for the samples MK7, MK11 and MK13 (2nd measurement) large values were be obtained.

The thermal conductivity λ, which of course will be analyzed in the future, appears to be very low (< 1 W/mK) according to another paper of Snyder *High Thermoelectric Performance in Non-Toxic Earth-Abundant Copper Sulfide* [49]. Additionally this value seems to be quite independent from the used temperature gradient and stochiometric composition of the synthesized samples. In this manner it is possible to calculate a potential ZT-value ($= \frac{S^2}{\rho\lambda} * T$), with the so far measured values of the electric resistivity as well as the Seebeck coefficient, the used measurement temperature and the published value for the thermal conductivity by Snyder. [49]

In table II.11 the measured values at 800 K, the assumed thermal conductivity λ from the above mentioned paper and the in this manner calculated potential ZT-value are shown:

Table II.11: XRD

Sample	MK7	MK11	MK13 (2nd)
Seebeck Coefficient S [μvK^{-1}]	200	210	180
Electric Resistivity ρ [μΩcm]	4000	5000	2000
Thermal Conductivity λ [mWcm^{-1}K^{-1}]	5	5	5
Temperature [K]	800	800	800
ZT-Value	1.6	1.411	2.592

As one can see in table II.11 very promising results for the potential ZT-values of sample MK7, MK11 and MK13 were obtained by using a value for the thermal conductivity, which is already known from corresponding literature. Especially MK13 shows very good results, which is a huge motivation for further experiments. Of course the thermal conductivity of each sample will be actually measured.

II.D. Conclusion

II.D.1. Sample Preparation

It was possible to prepare the copper(I)sulfide bulks in various molar ratios under normal or inert conditions. The following pressing and melt-solidification technique also worked without any problems. Except for the samples MK4 and MK5, which quartz tubes were shattered during the thermal treatment, which could be due to a fault of the vessel material. The melted,received bulks a little bit during this process and lost their original cylindrical form changing to a kind of drop-shaped one. All of the samples had a silver metallic color and showed visible voids as well as pores. To avoid these disturbing pores and to obtain denser bulks, probably more pressure or another press method should be considered. Exceptions were sample MK3 (overstoichiometric ratio, $Cu_{2.2}S$) and MK2 (undertoichiometric ratio, $Cu_{1.8}S$). The first one showed residual copper, whereas the latter resembled a dark crystalline material. The hardness of the samples can be compared to each other. MK1 (much harder) and MK2 (very porous) are the exceptions.

II.D.2. X-ray Diffraction

The crystal structures of Cu_2S Chalcosite (ICSD: 23596) and Cu_2S Chalcocite-Q (ICSD: 16550) showed the best fitting for most of the samples. It can therefore be assumed that these crystal structures can be found in the compounds. The exceptions are sample MK2 with the most different diffractogram compared to the others (due to the lowest molar ratio of $Cu_{1.8}S$) and samples MK7 (charge I), MK12 as well as MK13 (charge II). For these samples, however, the same crystal structures were used as before in default of a better alternative. The mentioned samples feature the lowest molar ratios with $Cu_{1.92}S$ (MK7), $Cu_{1.95}S$ (MK12) and $Cu_{1.93}S$ (MK13) within this thesis. It is interesting that these samples could not be compared to diffractograms with more appropriate molar ratios. This may be due to an unwanted, incomplete reaction to Cu_2S during the thermal treatment.

It was also of interest how the partly different sample preparations, one time under normal (charge I) the other one under inert conditions (charge II), affected the results. Comparing the relevant diffractograms with each other, no outstanding differences can be observed. This indicates that the previous chemical history of the samples is not so important, since the melt-solidification technique under high temperatures in vacuum is performed afterwards. Therefore, working under inert conditions appears not to be necessary. To verify this consideration further XRD measurement before the thermal treatment and analyses by electron microscopy would be necessary.

II.D.3. Seebeck Coefficient

In general, the samples showed quite promising results for the Seebeck coefficient, whereby MK11 had the highest values (and unfortunately at the same time the highest electric resistivity) around 210 [µV/K]. Compared with the results in Zhao and Snyder`s paper, similar but a little bit lower results were obtained, whereby in this thesis lower temperatures were used. [24]

The conducted analyses were performed to give a general overview of the Seebeck coefficient. To obtain more precise results, more elaborate measurements at different temperature, have to be carried out. In this manner it is possible to check if the samples show phase transitions by any chances as proposed by Zhao and Snyder.[24] This could be verified by measuring way more values especially at very low temperatures (down to 4 K) and a subsequently fitting with various band models.

II.D.4. Electric Resistivity

The results for the electric resistivity show wide differences. This can be explained by the fact that this value is way more difficult to measure than for example the Seebeck coefficient. Factors like the contact pressure of the samples and their geometry play a very important part. Also characteristics of the samples like porosity and cracks can change the measuring results drastically. As most of the produced samples in this thesis showed such properties, the partly strange results could be explained. However, it is interesting that some samples, namely MK1, MK7, MK11 and MK13 (2nd measurement), show a similar curve progression and hysteresis. This could be due to a phase transition. But again as for the Seebeck coefficient only further measurements at low temperatures with more values allow a reasonable fitting with band models.

II.D.5. Potential ZT-Value

As mentioned above it was possible to determine a potential ZT-value for the synthesized samples, although the thermal conductivity was not measured yet. Therefore a value for thermal conductivity from a well known appropriate literature was used. [49]

In this manner the potential ZT-value for the three most promising samples in regard to Seebeck coefficient and electric resistivity, namely MK7, MK11 and MK13 was calculated. An especially outstanding value with 2.592 was received for sample MK13. These are encouraging results, which definitely promotes further researches and experiments on this topic. Of course the actual thermal conductivity of each sample will be measured in the future to obtain the real ZT-value.

II.D.6. Outlook

For the future further and more elaborate measurements of the Seebeck coefficient and the electric resistivity are planned. In addition, also the thermal conductivity would be of great interest. In this manner an accurate ZT-value could be calculated with these values. It would be also important to produce samples with less or no pores and cracks, to obtain better results regarding the mechanical stability and thermoelectric characteristics like the electric resistivity.

References

[1] E. Riedel, C. Janiak, *Anorganische Chemie, 8.Auflage,* **2011**, De Gruyter.

[2] R.G. Pearson , *Recent Advances in the Concept of Hard and Soft Acids and Bases*, J. Chem. Educ., 64 (7), **1987**, 561-567.

[3] http://sciencenotes.org/printable-periodic-table/(access on 15th November 2016)

[4] C. Huang, *Rare Earth Coordination Chemistry, Fundamentals and Applications,* **2010**, Wiley.

[5] M.H.V. Werts, *Making Sense of Lanthanide Luminescence*, Science Progress, **2005**, 88 (2), 101–131.

[6] http://www.geology.neab.net/minerals/lanthani.htm (access on 15th November 2016)

[7] https://www.fas.org/sgp/crs/natsec/R41347.pdf (access on 15th November 2016)

[8] http://www.reuters.com/article/us-mining-toyota-idUSTRE57U02B20090831 (access on 15th November 2016)

[9] A. F. Hollemann, E. Wiberg, *Anorganische Chemie*, 33 Auflage, **1952**, De Gruyter.

[10] P. Pyykko, *Relativistic effects in structural chemistry,* Chem. Rev., **1988**, *88* (3), 563–594.

[11] J.C.G. Bünzli, S. V. Eliseeva, *Basics on lanthanide photophysics*, in P. Hänninen and H. Härmä (eds.), *Lanthanide Luminescence: Photophysical, Analytical and Biological Aspects*, **2010**, Springer.

[12] S. Sato, A. Ishii, C.i Yamada, J. Kim, C. Song, A. Fujiwara, M. Takata, M. Hasegawa, *Luminescence of fusion materials of polymeric chain-structured lanthanide complexes,* Polymer Journal 47, **2015**, 195–200.

[13] D. Bradshaw, A. Garai, J. Huo, *Metal–organic framework growth at functional interfaces: thin films and composites for diverse applications,* Chem. Soc. Rev., **2012**, 41, 2344–2381.

[14] A. N. Gusev, M. Hasegawa, G. A. Nishchymenko, V. F. Shul'gin, S. B. Meshkova, P. Dogac, W. Linert, *Ln(III) complexes of a bis(5-(pyridine-2-yl)-1,2,4-triazol-3-yl)methane ligand: synthesis, structure and fluorescent properties,* Dalton Trans., **2013**, 42, 6936.

[15] M. Hasegawa, H. Ohtsu, D. Kodama, T. Kasai, S. Sakurai, A. Ishii, K. Suzukic*, Luminescence behaviour in acetonitrile and in the solid state of a series of lanthanide complexes with a single helical ligand,* New J. Chem., **2014**,38 , 1225.

[16] J. Cras, C. Rowe-Taitt, D. Nivens, F. Ligler, *Comparison of chemical cleaing methods of glass in preparation for silanization,* Biosensors & Bioelectronics 14, **1999,** 683-688.

[17] K. Kao, C. Lee, T. Lin, C. Mou, *Cytochrome c covalently immobilized on mesoporous silicas as a peroxidase: Orientation effect,* J. Mater. Chem., **2010**, 20, 4653–4662.

[18] R. A. Poole, G. Bobba, M. J. Cann, J. Frias, D. Parker, R. D. Peacockc, *Synthesis and characterisation of highly emissive and kinetically stable lanthanide complexes suitable for usage 'in cellulo',* Org. Biomol. Chem., **2005**, 3, 1013-1024.

[19] M. Zhang, R. Gao, X. Hao, W. Sun, *2-Oxazoline/benzoxazole-1,10-phenanthrolinylmetal (iron, cobalt or nickel) dichloride: Synthesis, characterization and their catalytic reactivity for the ethylene oligomerization,* Journal of Organometallic Chemistry 693, **2008**, 3867–3877.

[20] E. Horkel, M. Schnürch, K. Schröder, *Lecture Notes from Organische Molekularchemie*, University of Vienna, **2015**.

[21] P. Bruice, *Organic Chemistry 7th Edition*, **2014**, Pearson.

[22] G.R. Fulmer, A. J. M. Miller, N. H. Sherden, H. E. Gottlieb, A. Nudelman, B. M. Stoltz, J. E. Bercaw, K. I. Goldberg, *Organometallics*, **2010**, 29, 2176-2179.

[23] Y. Kawamura, H. Sasabe, C. Adachi, *Simple accurate system for measuring absolute photoluminescence quantum efficiency in organic solid-state thin films*, Jpn. J. Appl. Phys. 43, **2004**, 7729–7730.

[24] L. Zhao, J. Snyder, et all, *High thermoelectric and mechanical performance in highly dense $Cu_{2-x}S$ bulks prepared by a melt-solidification technique, J. Mater. Chem. A.,* **2015**, 3, 9432.

[25] S. Bühler-Paschen, H. Michor, M. Reissner, *Lecture Notes for Festkörperphysik I*, TU Wien, **2016**.

[26] D. M. Rowe, *Thermoelectrics handbook: macro to nano*, CRC press, **2005**.

[27] http://www.roessel-messtechnik.de/webro-wAssets/docs/know-how/thermocouples-for-industrial-applications_de.pdf (access on 15th November 2016)

[28] H. Kleinke, *New bulk Materials for Thermoelectric Power Generation: Clathrates and Complex Antimonides*, Chem. Mater. **2010**, 22, 604-611.

[29] https://www.fraunhofer.de/de/presse/presseinformationen/2013/dezember/thermoelektrik (access on 15th November 2016)

[30] G. J. Snyder and E. S. Toberer, *Complex thermoelectric materials*, Nature Materials, **2008**, Vol.7(2), p.105.

[31] http://thermoelectrics.matsci.northwestern.edu/thermoelectrics/index (access on 15th November 2016)

[32] P.-R. Heinrich, *Determination of the density of charge carrier in thermoelectric materials,* diploma thesis, TU Wien, **2012**.

[33] I. Knapp, *Elektronischer und thermischer Transport in plastisch deformierten Skutteruditen*, master thesis, TU Wien, **2013.**

[34] https://www.tu-chemnitz.de/physik/FPRAK/F-Praktikum/Versuche_alt/v10a.pdf (access on 15th November 2016)

[35] E. Bauer, Ch. Eisenmenger-Sittner, J. Fidler, *Lecture Notes for Materialwissenschaften*, TU Wien, **2013**.

[36] http://www.physik.uni-wuerzburg.de/video/thermodynamik/g/sg15 (access on 15th November 2016)

[37] B. Budinska, *Thermoelektrische Eigenschaften der Heusler-Legierung $Fe_{(1-x)}Ni_xVa$*, bachelor thesis, Technische Universität, Wien, **2015**.

[38] https://upload.wikimedia.org/wikipedia/commons/e/e5/Seebeck_effect_circuit_2.svg (access on 15th November 2016)

[39] https://commons.wikimedia.org/wiki/File:Bragg%27s_Law.PNG (access on 15th November 2016)

[40] https://commons.wikimedia.org/wiki/File:Native_Copper_(mineral).jpg (access on 15th November 2016)

[41] http://www.seilnacht.com/Minerale/2kupfer.html (access on 15th November 2016)

[42] http://www.seilnacht.com/Lexikon/16Schwef.html (access on 15th November 2016)

[43] http://www.chemgapedia.de/vsengine/vlu/vsc/de/ch/16/ac/elemente/vlu/16.vlu/Page/vsc/de/ch/16/ac/elemente/chalkogene/schwefel/chal27.vscml/Supplement/1.html (access on 15th November 2016)

[44] https://de.wikipedia.org/wiki/Chalkosin#/media/File:Chalcocite-139815.jpg (access on 15th November 2016)

[45] S. Kashidaa, W. Shimosaka, *Valence band photoemission study of the copper chalcogenide compounds, Cu_2S, Cu_2Se and Cu_2Te,* Journal of Physics and Chemistry of Solids 64, **2003,** 2357–2363.

[46] R. Blachnik, A. Müller, *The formation of Cu_2S from the elements. I. Copper used in form of powders*. In: *Thermochimica Acta*. Band 361, Nr. 1–2, **2000**, 31–52.

[47] A. Müller, *Work-in-progress*, bachelor thesis, Technische Universität, Wien, **2016**.

[48] FindIt.Ink

[49] Y. He, T. Day T. Zhang, H. Liu, X. Shi, L. Chen, J. Snyder, *High Thermoelectric Performance in Non-Toxic Earth-Abundant Copper Sulfide,* Adv. Mater. **2014**, 26, 3974-3978.